Effects of Riblets on the Performance of the Supersonic Through-flow Fan Cascade Blades

by

Todd Arik Ninnemann

Dissertation submitted to the Faculty of the
Virginia Polytechnic Institute and State University
in partial fulfillment of the requirements for the degree of

DOCTOR OF PHILOSOPHY

in

Mechanical Engineering

APPROVED:

Wing Ng
Dr. W. F. Ng, Chairman

Clint L. Dancey
Dr. C. L. Dancey

Dr. J. A. Schetz

Douglas J. Nelson
Dr. D. J. Nelson

T. E. Diller
Dr. T. E. Diller

September 1994

Blacksburg, Virginia

Effects of Riblets on the Performance of the Supersonic Through-flow Fan Cascade Blades

by

Todd A. Ninnemann

Dr. W.F. Ng, Chairman

Mechanical Engineering

(ABSTRACT)

An experimental study to determine the effects of riblets on the performance of the supersonic through-flow fan (STF) cascade blades was performed. The two-dimensional cascade was tested in the Virginia Polytechnic Institute and State University intermittent wind tunnel facility, where the Mach and Reynolds (based on chord) numbers were 2.36 and 4.8×10^6, respectively. Three different V-grooved riblet heights were tested on the blades: 0.023, 0.033, and 0.051 mm. Riblet testing were conducted at design incidence as well as at off-design conditions (incidence angles: +5, -10 deg).

The riblet effect on the performance of the STF blades was determined by measuring the total pressure profile downstream of the cascade and integrating this total pressure to obtain an overall mass-averaged loss

coefficient. The riblet loss coefficient was compared with the loss coefficient of a control test case where an equivalent thickness of smooth material is applied to the blades. Results show that, at the design incidence, the 0.033 mm height riblets provided the optimal benefit, with a reduction of 8.5% in the loss coefficient compared to the control case. Smaller effects were measured at the off-design conditions.

Shadowgraph pictures were taken to study the effect of riblets on the turbulent transition location on the blades surfaces. At design incidence, the shadowgraphs revealed that the optimum height riblets delayed the transition location on the suction surface of the blades. Therefore, it was concluded that for the 0.033 mm height riblets the decrease in the cascade's loss coefficient was the result of delayed transition in addition to a decrease in turbulent viscous losses.

A numerical simulation was conducted to investigate both riblet effects on the STF blades. The numerical study showed that only the combination of the two riblet effects was able to produce a decrease in loss coefficient that was observed experimentally. Results from the numerical study indicate, that at design incidence, 2/3 of the riblet benefit is attributed to the delayed transition effect on the blades with the other 1/3 resulting from a decrease in turbulent viscous losses.

Acknowledgements

I would like to thank the members of my committee--Dr. Schetz, Dr. Dancey, Dr. Diller, and Dr. Nelson--for their time and help. I am especially indebted to my major professor, Dr. Ng, for his guidance and patience through these last three years.

I would also like to thank my office mates: Kevin Detwiler, Rob Wagner, Jeff Kozak, Abhijit Pande, David White, Zhenguo Yuan, and Terry Reid. They made graduate school a much more enjoyable experience.

I need to express my deepest thanks to Dr. Philip Andrew and D.J. Osborne. Phil showed the unique character of unselfishness. At every step in my research, Phil was there offering assistance or valuable advice. D.J. and I spent numerous hours discussing my research; but even more important, we discussed a larger and more meaningful research topic--life.

Finally, I would like to thank Kathy Ferguson for providing me with support and comfort in my times of need. Kathy with her beautiful smile and encouraging words was my sole inspiration.

Table of Contents

List of Illustrations

List of Tables

List of Symbols

A^+	Van Driest damping coefficient
C	chord
C_f	coefficient of friction
D	drag
h	riblet height
h^+	nondimensional riblet height
i	cascade incidence angle
M	Mach number
p	local static pressure
p_p	pitot pressure
P_t	local total pressure
s	spacing between riblet peaks
S	blade spacing or pitch
u	velocity component in pitch-wise direction
u_τ	friction velocity
x	stream-wise direction
y	transverse or pitch-wise direction

Greek Letters

α	yaw angle
γ	ratio of specific heats
Δ	difference between riblets and equivalent smooth layer
ν	turbulent viscosity
ρ	local density
ϖ	mass-averaged loss coefficient

Superscripts

—	averaged

Subscripts

1	conditions upstream of cascade
2	conditions downstream of cascade
s	smooth surface
w	wall conditions

1.0 Introduction

The increasing demand for international air travel has created renewed interest in a second-generation, supersonic transport aircraft known as the high speed civil transport (HSCT). Unlike the current generation of commercial supersonic aircraft, the HSCT is designed to economically compete with the subsonic wide-body aircraft. In order to produce a more viable supersonic aircraft, significant technological advancements in propulsion systems must be developed.

For the HSCT, one approach to improve the propulsion system efficiency involves an innovative turbofan concept known as the supersonic through-flow fan (STF). The unique design of the STF allows the flow entering and exiting the fan to be supersonic in the absolute reference frame. This significantly differs from a conventional turbofan, which first diffuses the flow to a subsonic axial velocity before entering the fan.

In 1956, Ferri[1] uncovered, through the use of cycle studies, the potential advantages of the flow entering the fan at supersonic axial velocities. Years later, design refinements of Ferri's concept by Advance Technology Laboratory, Incorporated[2] developed the idea for axially supersonic velocities throughout the fan stage. Physical distinctions between a STF and a conventional turbofan engine are presented in Figure 1.1. The smaller STF engine provides

Supersonic Through-flow Fan Engine

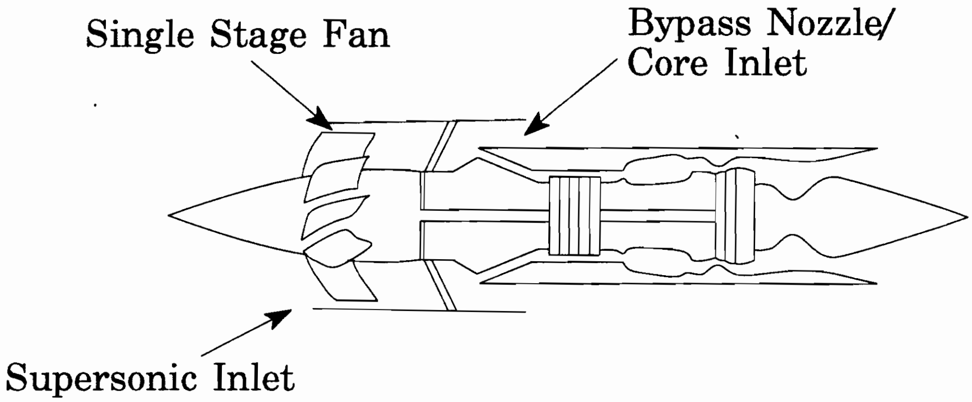

Conventional Mixed Flow Turbofan Engine

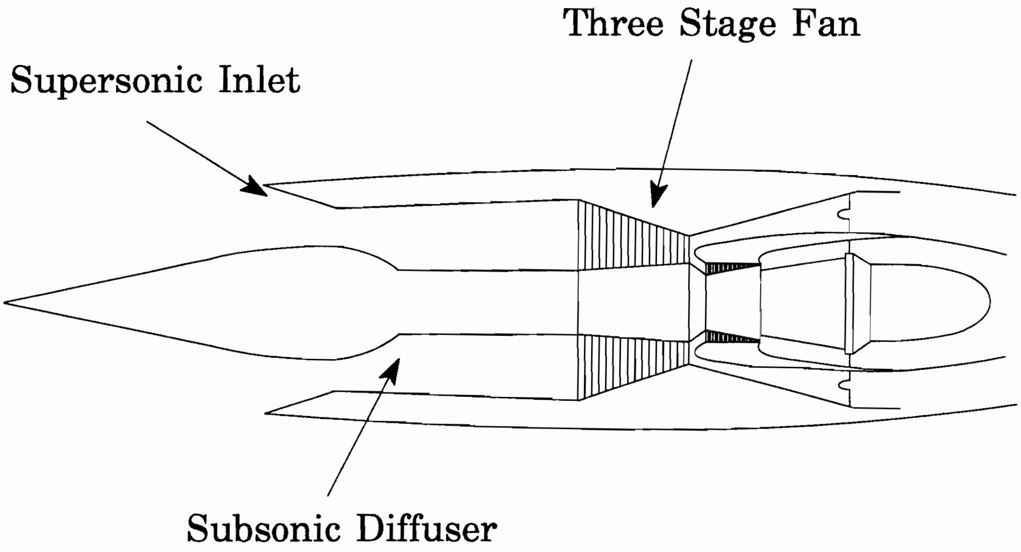

Figure 1.1 Comparison of STF Engine and Conventional Turbofan

a significant amount of weight savings. Compared to a conventional fan engine, the STF features a shorter inlet because the flow is not slowed to subsonic velocities. A shorter inlet produces lower inlet drag and lower diffusion losses with less energy requirement for boundary layer bleed. Further weight reduction results from the supersonic through-flow fan engine needing only a single fan stage to produce the required pressure rise.

Several cycle studies, incorporating the STF engine concept into a high speed civil transport aircraft, have shown potential benefits. Franciscus[3] in 1978 and Tavares[4] in 1985 studied the supersonic through-flow engine concept at flight conditions of Mach 2.32 and Mach 2.7 respectively. Conclusions from their studies indicate a 25% reduction in the propulsion system weight and a 12% reduction in fuel consumption. The combination of these results provides a 25% increase in flight range. Further information on the possible advantages of the STF engine are provided by Kepler and Champagne,[5] Franciscus,[6] and Saunders and Glassman.[7]

Until recently, experimental studies to determine the feasibility of a fan accepting supersonic axial flow were limited, with Boxer,[8] Savage et al.,[9] and Breugelmans[10] providing only preliminary data. As a result, the N.A.S.A. Lewis Research Center initiated the STF program to design, build, and test a fan rotor that operates with supersonic axial velocity from inlet to exit. Due to a limited experimental database, the design phase of the STF fan heavily depended on computation fluid dynamics (CFD). This was particularly true for the shape of the STF blades as documented by Wood, et al.[11] and Schmidt, et al.[12]

In conjunction with the STF development work at N.A.S.A Lewis Research Center, Virginia Polytechnic Institute and State University (VPI&SU) constructed a linear, two-dimensional supersonic through-flow cascade in order to study the flow physics of the STF rotor in more detail. Previous research at VPI&SU with the STF cascade extensively tested the original prototype blading design. Chesnakas[13] made mean flow measurements and developed a method to account for the different loss mechanisms in the cascade. Turbulence measurements in the wake at design conditions with use of a single hot-wire probe were recorded by Bowersox.[14] Andrew,[15] using a two component Laser Doppler Anemometer (LDA) system, studied the character of the turbulence in the wake in an attempt to improve CFD calculations at off-design conditions.

The emphasis of the present research is distinct from all previous research in the STF cascade. Rather than further study the flow physics of the original blade design, this research focuses on improving the performance of the STF cascade by modifying the blade surface with riblets.

Riblets, a passive technique, reduce turbulent skin friction drag by modifying the smooth surface geometry with micro-grooves. The riblets' effect on the performance of the supersonic through-flow cascade blades was determined by measuring differences in the wake profile downstream of the cascade. Results from the riblet effects for varied riblet heights and different cascade inflow incidence angles are presented in this document. In addition, shadowgraph photography of the flow between the blades and a two-dimensional, computational simulation were executed in order to better understand the riblet effect on the performance of the cascade blades.

This dissertation will first review the past riblet research. Next, a description of the cascade facility and experimental procedure will be given. Then the unique flow field characteristics of the cascade--for design and off-design conditions--will be presented, followed by the experimental results. The next two sections describe a method to numerically model the riblet effects on the cascade blades and the results from this numerical simulation. Lastly, conclusions from the riblet study are presented.

2.0 Riblets

For more than a decade, evidence has shown that modifying the geometry of a smooth surface can reduce viscous losses in turbulent boundary layer. This achievement results from altering the smooth surface with microgrooves, known as riblets, and aligning these grooves longitudinally with the mean flow direction. A sketch of a riblet geometry, defining the riblet height and spacing, and its orientation to the mean flow direction is given in Figure 2.1. Although riblets provide an increased wetted surface area, the net result can be a 10% reduction in viscous drag when compared to a smooth surface.

This chapter summarizes the significant results from other riblet studies with an emphasis of relating it to the current riblet experiment. A more detailed review regarding the developments of riblet research can be found in Walsh,[16] Coustols and Savill,[17] Bandyopadhyay,[18] and Savill.[19] In this chapter, a general discussion of riblet performance in different flow conditions and surface geometries will be introduced first. This is followed by the possible explanations for the riblets' ability to reduce skin friction. Finally, a review of the computational efforts to model riblets in turbulent flows is presented.

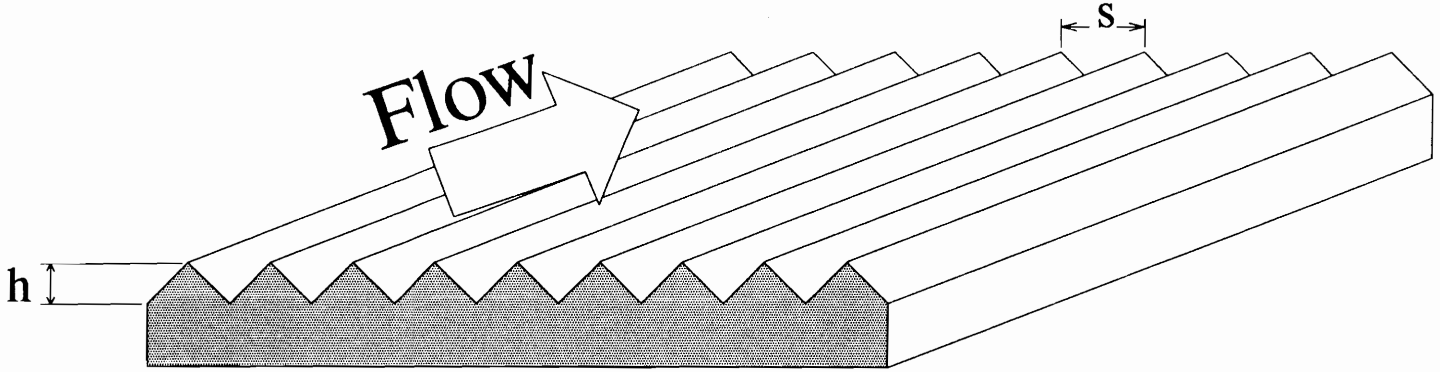

Figure 2.1 Riblet Nomenclature

2.1 Riblet Performance

Early investigations into the drag reduction potential of riblets centered on subsonic and transonic external turbulent flows with simple surface geometries, i.e., flat plate. One of the first researchers to investigate the influence of riblets on a turbulent boundary layer was Walsh. Through an extensive parametric study, Walsh with others[20-23] at N.A.S.A Langley Research Center researched the effectiveness of many different riblet geometries. Some examples of the different shapes investigated are presented in Figure 2.2. In these studies, a V-groove riblet with a height and a spacing about twice the sublayer thickness produced an optimum 8% drag reduction. This result was later confirmed by a number of other researchers.[24-28]

For internal flows, similar results to the above flat plate studies were documented. Most of this research has centered on pipe flow experiments.[29-32] For cascade flows, only one successful riblet study is reported. Fang et al.[33] studied a cascade of NACA-65-0100 compressor blades at low speed. A decrease in losses of more than 10% was reported. Also, the riblets' performance was shown to be insensitive to small changes in the cascade incidence flow angle.

For supersonic flows, riblet research was limited to a few studies in

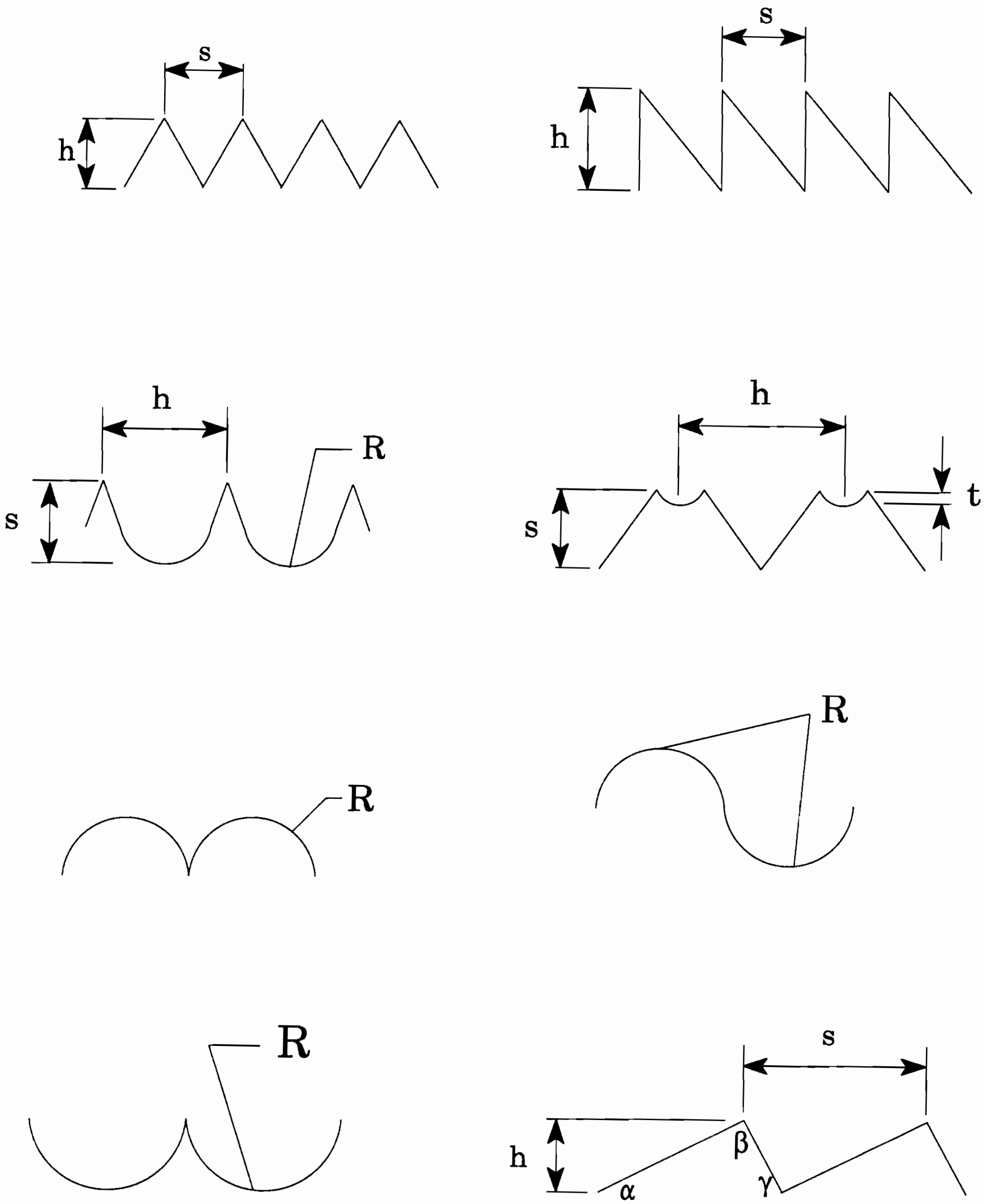

Figure 2.2 Examples of Walsh's Parametric Study

external flows. Robinson[34] analyzed the effects of riblets on the turbulence structure at Mach 2.97. Although no attempt was made to measure the change in drag, Robinson showed that the riblets reduced the intensity of the turbulent fluctuations in the buffer zone of the boundary layer. Gaudet[35] studied the riblet effects on a flat plate. At Mach 1.25, he measured a maximum reduction of 7%. A preliminary flat plate study by Coustols et al.[36] at Mach 1.9 indicated a maximum drag reduction close to 10%. Another riblet study, conducted on a cylindrical centerbody with Mach numbers varying between 1.6 and 2.5, showed a reduction in drag of 4.5%.[37]

Lately, the successful application of riblets has not been restricted to simple surface geometries. For example, studies include the testing of riblets on the surfaces of an aircrafts' nacelle,[38] fuselage,[39] and wing.[40] Wind tunnel testing of riblets on an airfoil at both subsonic and transonic conditions has been conducted.[41-42] Also, riblets have been applied to the three-dimensional surface of a keel of the racing yacht "Stars and Stripes" and a 1/3 scale model of the "Australia II".[43] The conclusions from these experiments reinforce the drag reduction potential found in the flat plate studies.

The results from previous riblet studies indicate that a wide range of riblet heights can decrease the viscous losses in a turbulent boundary layer. By defining a nondimensional riblet height, Savill[19] has shown that most riblet results for subsonic, transonic, and supersonic flows can collapse into one general performance curve. The nondimensional riblet height, h^+,[1] is defined as:

$$h^+ = \frac{\rho_w u_\tau h}{\mu_w} \tag{2.1}$$

where u_τ is the friction velocity, h is the riblet height, μ_w is the viscosity at the wall ,and ρ_w is the density at the wall. Presented in Figure 2.3 is the trend for the riblet height parameter, h^+ versus drag reduction. Figure 2.3 represents a general curve fit of the results from Savill[19] along with results from more recent riblet studies. For the riblet performance trend, the change in drag, ΔD, is defined as:

$$\Delta D = \frac{D_{riblet} - D_{smooth}}{D_{smooth}} \tag{2.2}$$

In Figure 2.3, an optimum reduction is achieved at an h^+ of approximately 13. The trend shows a diminishing riblet benefit for heights that diverge from the optimum riblet height. Below an h^+ of 5 and above an h^+ of 25, the effectiveness of the riblets to reduce viscous drag can be lost or even be detrimental.

The main focus of previous riblet studies has centered on testing riblets in a turbulent boundary layer. As described earlier, riblets can produce a 10% decrease in turbulent viscous losses. In a laminar boundary layer, riblets are not as effective. Rohr et al.[29] studied riblets in a laminar, fully developed pipe

---

[1] Nondimensional riblet spacing, s^+, can also be used.

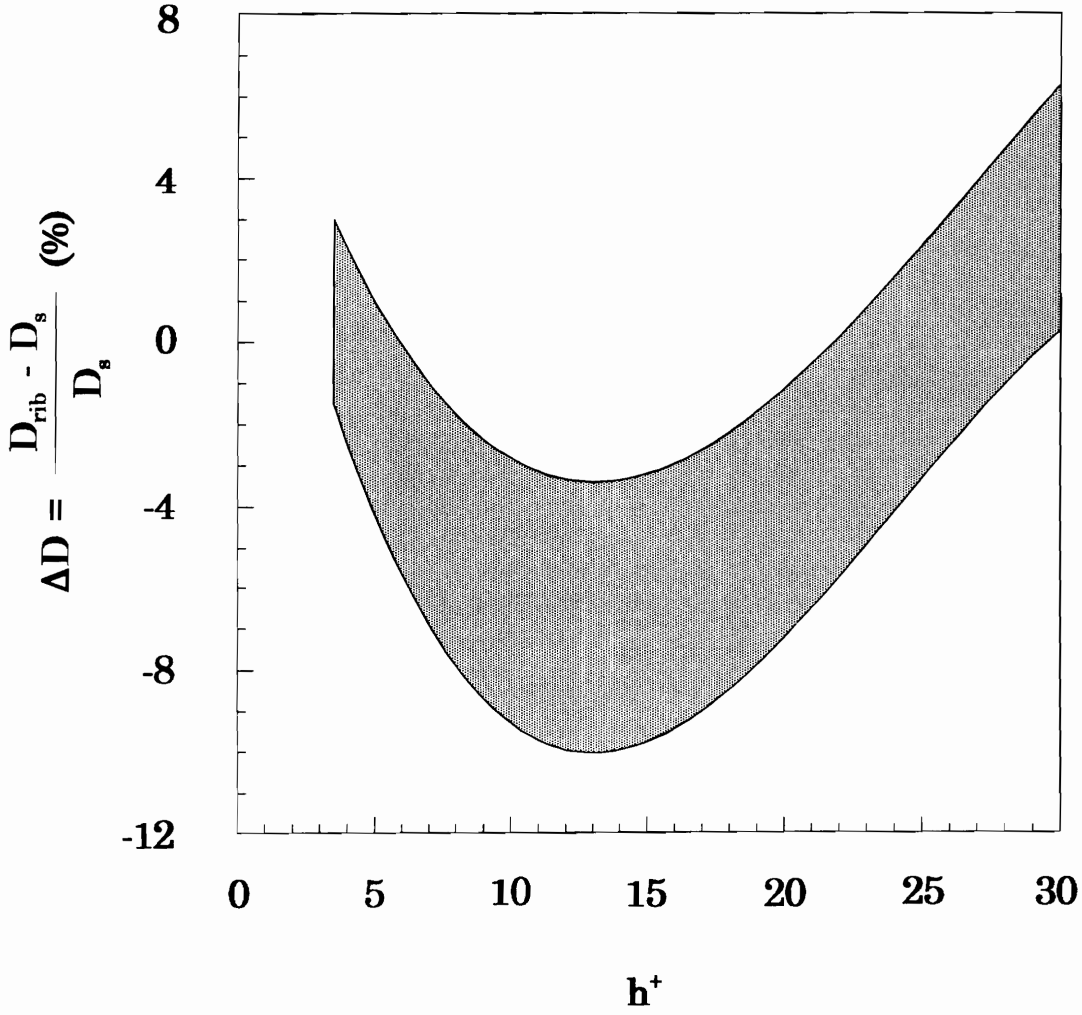

Figure 2.3 Riblet h^+ Parameter Trend

flow and found no significant change in skin friction due to the riblets. In a low speed flat plate study, Djenidi et al.[44] reported that riblets produce only a negligible change in drag for a laminar boundary layer.

Very little attention has been focused on the riblet's effect on the transition of a laminar boundary layer. Typically, riblet tests are conducted in fully turbulent flows as the boundary layer is artificially tripped upstream of the riblets. Only two studies have documented the effect of riblets on transition and their results are contradictory. Newmann and Dinkelacker[45] studied the riblet effects on a cylindrical centerbody located in a water tunnel and concluded that riblets delay the development of the initial turbulent structure. In their study, they attributed part of the measured 13% decrease in viscous drag to the riblet's ability to delay transition. On the contrary, Ladd et al.[46] conducted experiments on the effects of riblets on a flat plate in a water tunnel. They concluded that riblets, similar to roughness, instigate the boundary layer transition to turbulence earlier than a smooth surface.

Even though riblets were successfully tested in a wide variety of different flow environments, they have never been tested in a flow similar to that provided by the STF cascade. Illustrating this point, Table 1 summarizes the previous riblet studies, including the STF cascade study, in terms of surface geometry and flow conditions.

Unlike most riblet studies, the boundary layer in the STF cascade was not artificially tripped--allowing an opportunity to study the riblets effect on transition. In addition, the cascade environment was one of supersonic internal flow where shock-boundary layer interaction predominates. Also present was an overall favorable pressure gradient. This minimizes boundary layer growth and accelerates the flow as it proceeds through the blade passage. More details on the STF cascade's unique flow field are provided later in this document.

Table 1. Summary of Previous Riblet Studies

	Surface Geometry	Flow Conditions		
		Subsonic	Transonic	Supersonic
External:	flat plate	x	x	x
	airplane components	x	x	
	racing yacht	x		
	cylindrical centerbody	x	x	x
Internal:	pipe	x		
	cascade	x		(STF)
	diffuser	x		

2.2 Mechanism for Drag Reduction

At this time, the riblet mechanism to reduce viscous losses is poorly understood. In an attempt to explain the mechanism, numerous low speed studies, involving flow visualization techniques and detailed measurements just above and within the riblet grooves, were initiated. Presently, two potential explanations for the drag reducing effect exist. One idea suggests that riblets alter the turbulent production process; the other hypothesizes that the mechanism is purely a viscous one. The only agreed upon conclusion, from these studies, is that the riblets' drag reducing effect is limited to the inner region of the turbulent boundary layer. This riblet effect produces an apparent thickening of the viscous sublayer and an upward shift in the law of wall profile. As shown later, the above conclusion was helpful to model the riblet effect in the numerical simulation of the STF cascade.

2.2.1 Turbulent Production Mechanism

A number of researchers believe that riblets reduce skin friction by modifying the coherent structure of the turbulent boundary layer. Bacher and Smith[47], through a combined flow visualization and hot-film anemometry study, proposed that secondary vortices form at the riblet peak. These counter-rotating vortices weaken the stream-wise vortices and help retain the low speed fluid with the riblet grooves. In other words, riblets delay the development of the turbulent boundary layer which results in a reduction in the turbulent wall skin friction. In another study, Choi[48] conducted measurements inside and above U-shaped grooves and concluded that riblets operate by restraining the lateral movement of the counter-rotating vortices. Choi results showed a reduction in bursting activity and, therefore, a reduction in one of the main sources of turbulent production. Falco[49] suggested that the result of the thickened sublayer by the riblets may decrease the initial bursting rate.

2.2.2 Viscous Mechanism

Another possible explanation is that the riblets provide a purely viscous process for drag reduction. Detailed studies of the symmetric V-groove riblet design were conducted by a number of researchers to propose a viscous mechanism.[50-52] Measurements from these experiments showed an increase in wall shear stress near the riblet peak, but a substantially reduced shear stress within the riblet valley. Extensive measurements in a riblet groove by Park and Wallace[53] allowed the integration of the riblet wall shear stress. Their results indicate that even though the riblets provide an increase in wetted surface area, the net result produced a lower drag than a smooth surface. Park and Wallace attributed this drag reduction due to the slow moving, viscous dominated fluid within the riblet grooves. This type of flow prevented the high-momentum fluid from above the riblets to penetrate into the lower half of the riblet grooves.

Clearly the understanding of the riblet's mechanism to reduce viscous losses is incomplete. For the STF riblet study, the size of the riblets preclude any detailed measurements in the riblet vicinity. Therefore, this research is limited in studying the effects of the riblets on the supersonic through-flow cascade blades by measuring differences in the wake profile downstream of the cascade.

2.3 Computational Efforts

A significant number of computational efforts have been undertaken in order to better understand the riblet effect. Computational studies have been used to try to explain the riblet drag reduction mechanism and also to optimize riblet shape. In addition, a method to model the riblet effect was developed to predict the performance of riblets on various surface geometries and different flow conditions.

The first riblet computational study was performed by Kahn[54] who used an algebraic Reynolds stress turbulent model over 3-dimensional V-shaped grooves with an aspect ratio (h/s) of 2. Kahn found an optimum riblet height of an h^+ of 8 produced 20% drag reduction. He attributed the reduction to the formation of a secondary vortex prohibiting high momentum fluid into the riblet grooves. These results, however, are in question due to the low mesh resolution used in the study.

Bechert and Bartenwerfer[55] developed a unique approach to study riblets. Using conformal mapping, Bechert and Bartenwerfer charted the linear sublayer profile of a smooth flat plate onto a variety of sublayer-scale riblet surfaces. Their calculations showed that riblets see a substantial reduction in shear stress within the riblet valley and an increase in shear stress near the riblet peak. They concluded that the primary drag reduction mechanism is a viscous one.

Recently, Launder and Li[56] explored the effectiveness of L, V, and U-shaped riblets in turbulent flows by applying a two-equation turbulence model inside the riblet grooves. The optimization process concluded that the U-shape design provided better performance than the commercial V-groove riblet. A similar trend for drag reduction versus riblet height was obtained in this study; however, the optimum size occurred at larger riblet heights than experiments had indicated. The authors attributed the shortcomings to the turbulent model's inability to restrain secondary motions leading to an inefficient amount of momentum exchange.

Both Choi et al.[57] and Chu and Karniadakis[58] used direct numerical simulation to calculate a drag reduction for riblets on a flat plate. Choi et al. indicated the drag reduction resulted from the riblet size restricting the location of the stream-wise vortices to appear above the riblet peak. As a result, only the limited area near the riblet peak is exposed to the induced high-speed fluid from the vortices. In the other numerical simulation, Chu and Karniadakis concluded the mechanism was due to the riblets prohibiting the span-wise motion and the ejection of low speed fluid from the near wall region.

A practical approach for modeling the riblet effect was carried out by McLean et al.[40] In concept, the riblet effect on the turbulent boundary layer is modeled without going into the riblet grooves themselves. By representing the riblet effect in the turbulent model as a "negative roughness" function[2], McLean et al. were able to predict the overall reduction in viscous losses. The advantage of this approach is that only a 2-D numerical simulation is required to simulate the riblet effect in a turbulent boundary layer. In addition, this concept can easily be adapted to predict the global riblet benefit for most numerical simulations regardless of surface geometry and flow conditions.

McLean et al. simulated riblets on an airplane wing. Compared to the experimental results, the simulated results were underpredicted--both in the smooth and riblet case. However, the relative change in viscous losses between the simulated smooth and riblet surfaced wing compared very well with the

---

[2] Rotta[59] describes the roughness function as simply a shift in the reference plane beneath the actual surface.

experimental results. Using the same modeling method, Truong and Pulvin[60] performed a turbulent flow computation with riblets in a diffuser. The computations with the riblet effect showed good agreement with their diffuser experimental results.

The concept for modeling the riblet effect in a turbulent boundary layer was used in the simulation of the supersonic through-flow fan cascade blades. Unlike the studies by McLean et al. and Truong and Pulvin, the predicted reduction in the turbulent skin friction did not match the change in viscous losses due to riblets in the STF cascade. As will be shown later, the reason for the disagreement is that riblets provide two distinct drag reducing functions on the STF cascade blades. Riblets reduce the turbulent viscous losses and also postpone the development of the turbulent boundary layer.

3.0 The Experiment

3.1 Wind Tunnel Facility

The riblet experiments were conducted in the VPI&SU cascade wind tunnel. An overall schematic of the facility and photograph of the 2-D nozzle and test section are presented in Figure 3.1 and Figure 3.2 respectively. The facility is an intermittent blow down tunnel with a run time of approximately 20 seconds. The compressed air is dried, filtered, and cooled to a total temperature of approximately 290 K before entering the storage tanks. A personal computer controls the movement of a butterfly valve via feedback control loop. During tunnel operation, the valve adjusts to maintain a total pressure of 450 kPa in the settling chamber. The settling chamber contains flow straighteners and screens to reduce the freestream turbulence level to approximately 1%.[14] The flow conditions of the facility provide a unit Reynolds number of approximately 48 million per meter based on chord. A 2-D converging-diverging nozzle provides a nominal Mach number of 2.4 to the test section inlet. Downstream of the test section, the air exhausts through a muffler to atmospheric conditions.

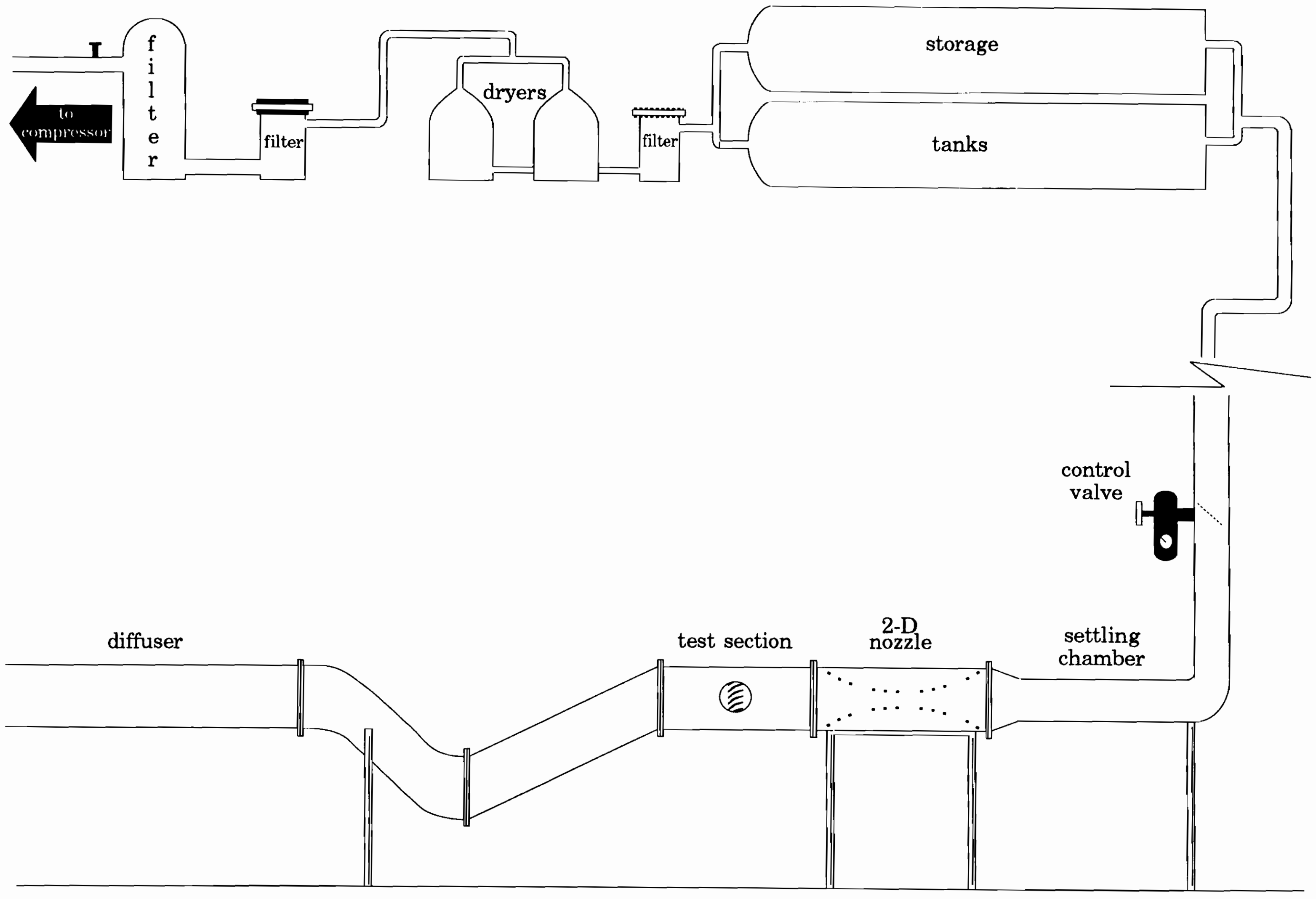

Figure 3.1 VPI&SU Intermittent Cascade Wind Tunnel Facility

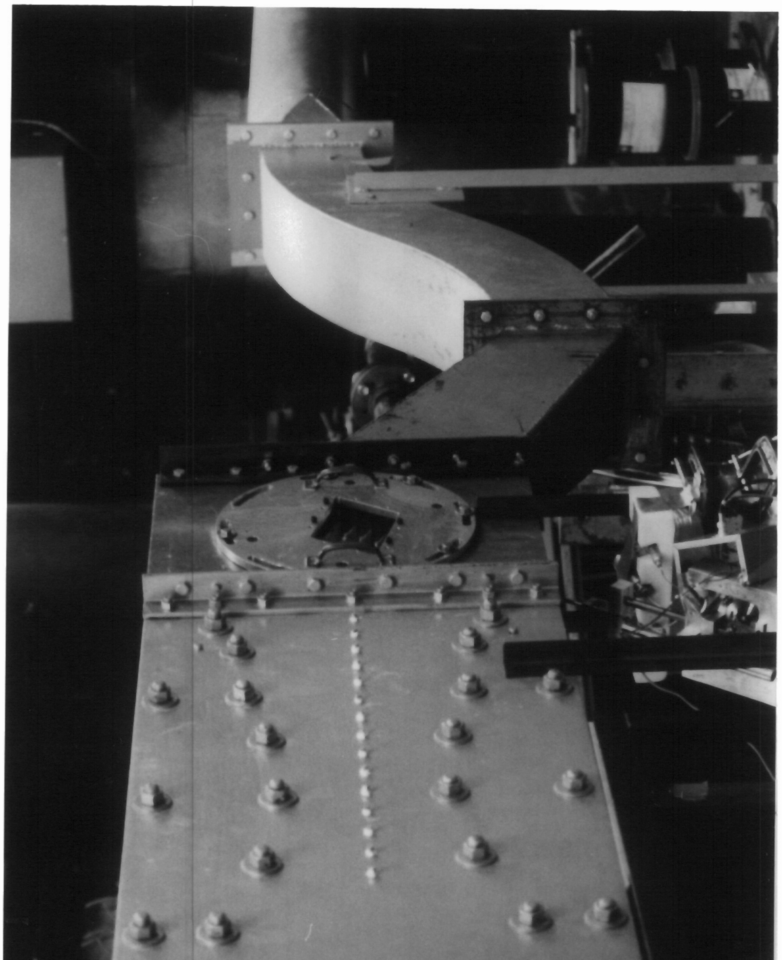

Figure 3.2 Photograph of 2-D Nozzle and STF Cascade Test Section

3.2 STF Test Section

The supersonic through-flow cascade test section is presented in Figure 3.3. The test section is 22.86 cm in height and 15.25 cm in span. The inlet Mach number to the test section is 2.36±0.05.[13] The circular test section doors are designed to rotate for facilitating the testing of blades at different inflow angles. The doors contain plexiglass windows so that shadowgraph photography of the flow field between the blade passages can be taken. The test section consist of six full-scale blades based on the midspan design of N.A.S.A Lewis prototype blades. As seen in Figure 3.4, the six cascade blades have a chord length, C, of 10.03 cm and a span, s, of 3.02 cm. This provides a solidity of 3.32.

Also presented in Figure 3.4 is the definition of the inflow angle and the cascade coordinate system. The design incidence, $i=0°$, for the cascade blades is defined as the direction parallel to the blade suction surface at the leading edge. For the measurements downstream of the cascade, a x-y coordinate system is defined, as shown in Figure 3.4, with the x-direction perpendicular to the trailing edges of the cascade blades and the y-coordinate parallel to the cascade. The origin of the coordinate system is at the trailing edge of the third blade from the bottom of the cascade. All measurement for the riblet experiment were made downstream of the cascade and at the midspan location of the blades.

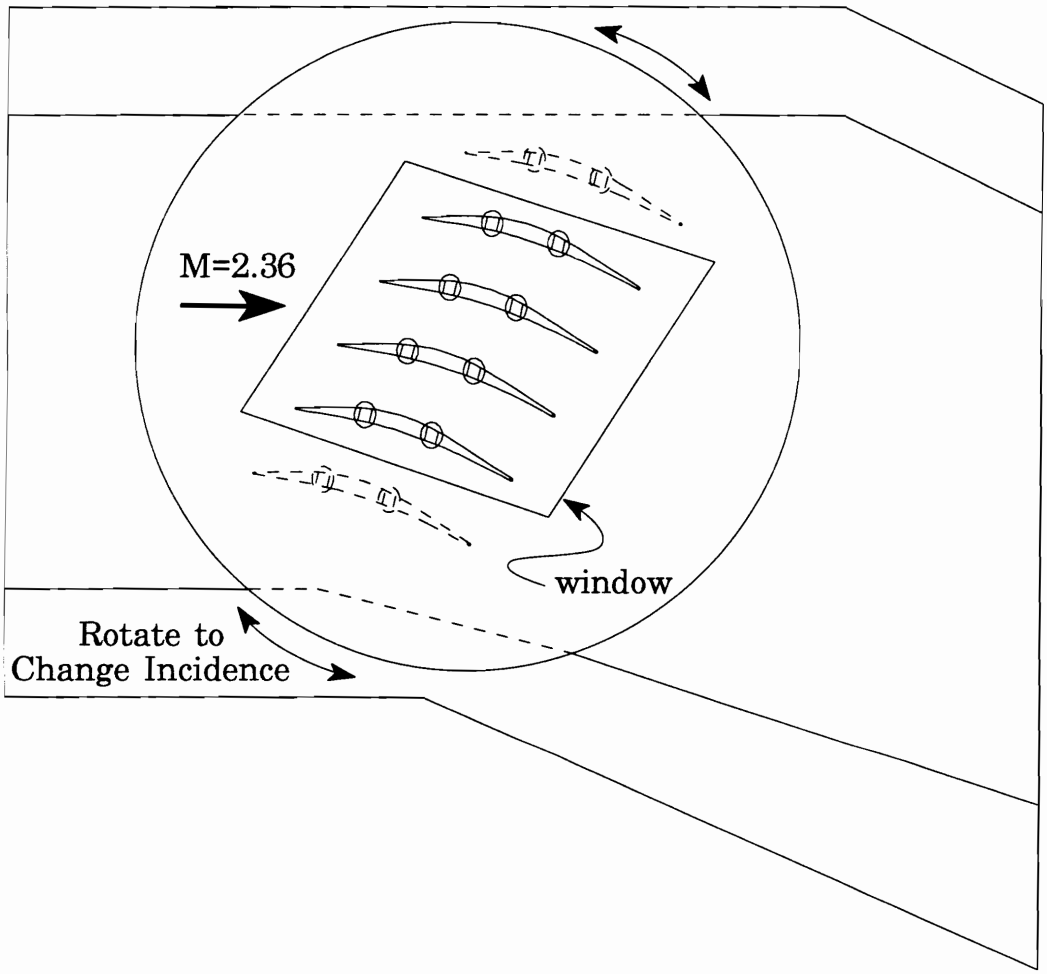

Figure 3.3 STF Test Section

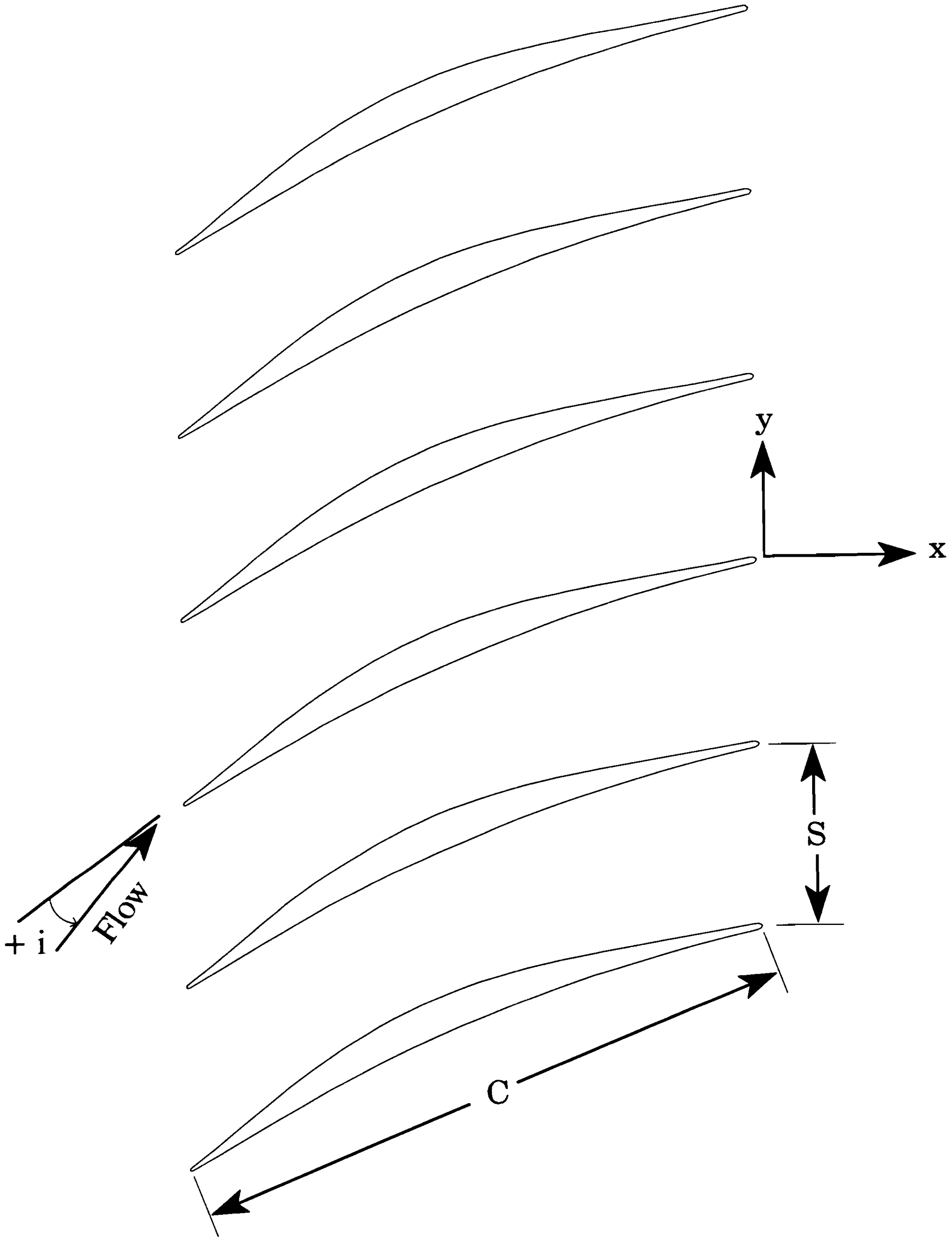

Figure 3.4 STF Cascade Nomenclature

3.3 Pitot-Static Probe

Measurement were made downstream of the cascade using a Pitot-static probe designed by Chesnakas.[13] The probe, shown in Figure 3.5, is designed for two-dimensional supersonic flows. A Pitot tube is centrally mounted on the probe with a parallel plate located on each side. Each plate contains a pressure tap to measure static pressure. Since the flow is supersonic downstream of the cascade, the pitot tube measures the total pressure behind a normal shock. The supersonic conditions in the cascade also required that the plates be located far enough apart so the shocks originating from the front of the plates do not interfere with the flow at the Pitot tube. More detailed information regarding the Pitot-static probe can be found in reference 13.

The Pitot pressure and the static pressure measurements from the probe are used to calculate Mach number, total pressure, P_t, and mass flux, ρu, downstream of the cascade blades. Integration of the calculated profiles produces a mass-averaged loss coefficient which was used to determine the riblet effect on the blades.

3.4 Wind Tunnel Test Procedure

For the riblet study, the Pitot-static probe was positioned downstream

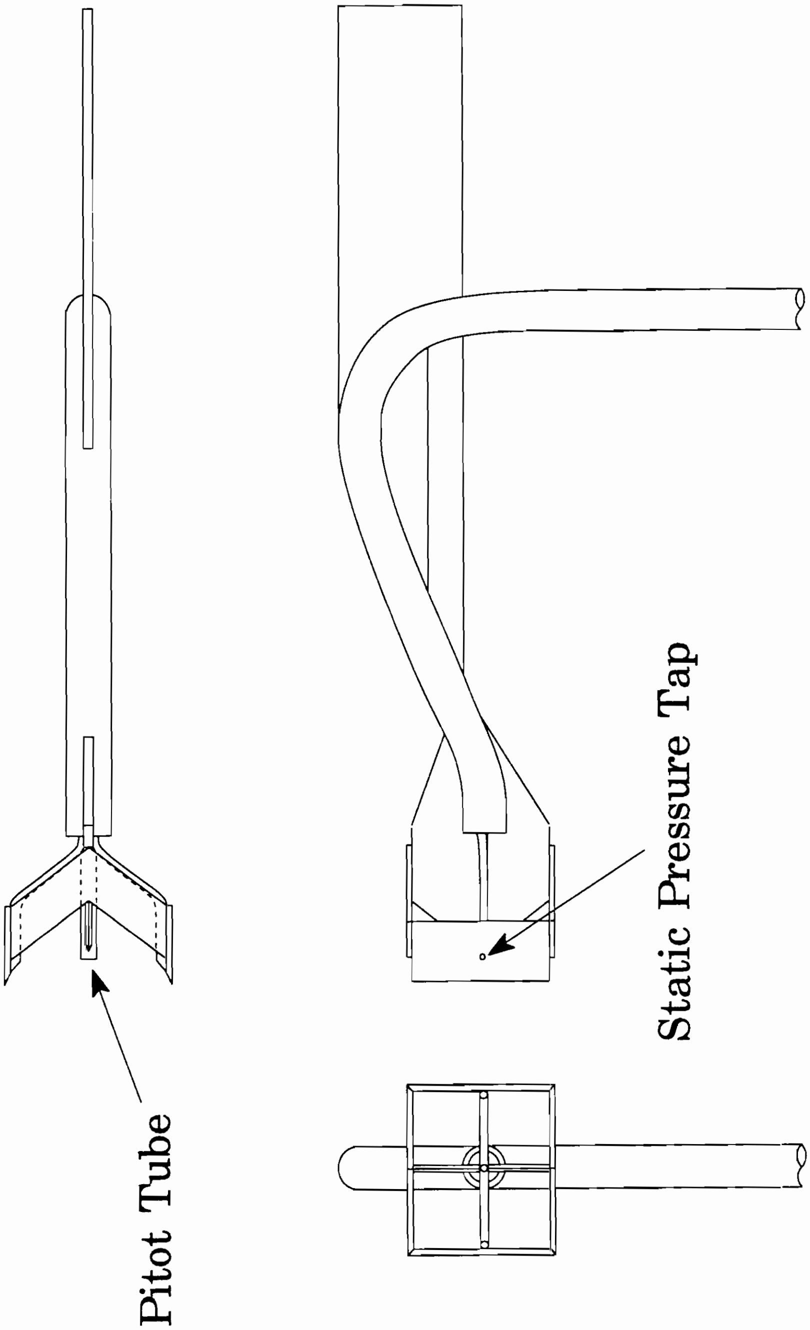

Figure 3.5 Pitot-static Probe

of the cascade at the axially station of x/C=0.37. During a tunnel run, the traverse mechanism moved the probe at a constant speed parallel to the trailing edges of the cascade blades. At a predetermined probe location the data acquisition process was activated. Total pressure and temperature upstream of the cascade along with Pitot, static pressure measurements, and probe location were recorded. The tunnel run time required for a complete probe survey was approximately 10 seconds. The riblet test conditions for different riblet heights and incidence angle investigated in the STF cascade is presented in Table 2.

Table 2. Riblet Test Conditions

Cascade Incidence Angle (deg)	**Riblet Height** (mm)
0	0.023
0	0.033
0	0.051
-10	0.033
+5	0.033

3.5 Data Reduction

In the data reduction process, the resultant Pitot pressure and average static pressure were used to calculate profiles of Mach number, total pressure, and mass flux downstream of the cascade blades. Total pressure profiles for the riblet and smooth covered blades were compared in order to help understand the riblet effect on the blades. Integration of the total pressure profile in combination with the mass flux profile produced a mass-averaged loss coefficient. Comparison of the loss coefficients quantified the performance of riblets on the supersonic through-flow cascade blades.

3.5.1 Mean Flow Calculations

The Mach number is calculated from the one-dimensional gas dynamics relationship involving the ratio of the Pitot pressure, p_p, to the static pressure, p.

$$\left(\frac{p_p}{p}\right)^{\frac{\gamma-1}{\gamma}} = \left(\frac{\gamma+1}{2}\right)^{\frac{\gamma+1}{\gamma}} M^2 \left(\gamma M^2 - \frac{\gamma-1}{2}\right)^{-\frac{1}{\gamma}} \qquad (3.1)$$

A curve fit for the above expression was used to solve for Mach number

$$M = 0.8889857\phi^{0.45676} + 0.020721\phi + 0.0917443 \tag{3.2}$$

where

$$\phi = \frac{p_p}{p} - 0.892929 \tag{3.3}$$

The total pressure downstream of the blades was calculated from the relationship

$$P_{t2} = p\left[1 + \frac{\gamma - 1}{2}M^2\right]^{\frac{\gamma}{\gamma-1}} \tag{3.4}$$

and the mass flux downstream of the cascade from the equation

$$(\rho u)_2 = P_{t2}\, M\left[1 + \frac{\gamma - 1}{2}M^2\right]^{\frac{-1(\gamma+1)}{2(\gamma-1)}} \tag{3.5}$$

3.5.2 Integrated Loss Coefficient

Mass-averaged loss coefficient is calculated by integrating the calculated total pressure and the mass flux for one complete blade spacing, S, to get an overall total pressure, $\overline{P_{t2}}$, downstream of the cascade blades defined as

$$\overline{P_{t2}} = \frac{\int_0^S (\rho u)_2 \, P_{t2} dy}{\int_0^S (\rho u)_2 dy} \tag{3.6}$$

The mass-averaged loss coefficient is calculated from

$$\varpi_2 = \frac{1 - \dfrac{\overline{P_{t2}}}{P_{t1}}}{1 - \dfrac{p_1}{P_{t1}}} \tag{3.7}$$

where P_{t1} and p_1 are the total pressure and static pressure upstream of the cascade blades.

3.6 Riblet Material

The riblet material was manufactured by 3M and consists of vinyl sheeting with machined V-grooves and a self adhesive backing. Riblet material was applied to the surfaces of the blades by starting at the pressure side trailing edge and wrapping the material around the leading edge. The application was completed at the trailing edge of the suction side of the blade. This procedure provided a smooth continuous riblet covered surface for the STF blades.

The application of the riblet material increases the radius of the leading edge. Due to the supersonic nature of the STF cascade, any enlargement of the leading edge radius will result in an increase in the losses from the leading edge shock. As a result, the riblet covered blades were not compared to the smooth bare blades. Instead, the riblet results were compared to a smooth layer result with an equivalent riblet thickness. Since a smooth material with the appropriate thickness of the riblet material could not be obtained, the riblet results were bracketed between the results of one and two layers of a smooth material and compared to the results of an interpolated, equivalent thickness of smooth material. The method used to determine the smooth, equivalent thickness result will be discussed later in this paper.

The application of the smooth material was the same as describe for the riblet material. Figure 3.6 and Table 3 describes the thicknesses of smooth material and the three different sizes of 3M riblet material used in the experiment.

3.7 Riblet Test Procedure

The riblet testing procedure entailed a number of repetitive runs to ensure the effect was the result of the riblets on the blades and not from any variations in the facility or instrumentation. A total of six testing stages were required to complete the riblet test and an outline is presented in Table 4. In each stage, back-to-back runs were completed to ensure testing repeatability.

Table 3. 3M Riblet Material

Material	**Thickness** (mm)
Smooth, one layer	0.081
0.023 mm height riblet	0.099
0.033 mm height riblet	0.135
0.051 mm height riblet	0.137
Smooth, two layers	0.162

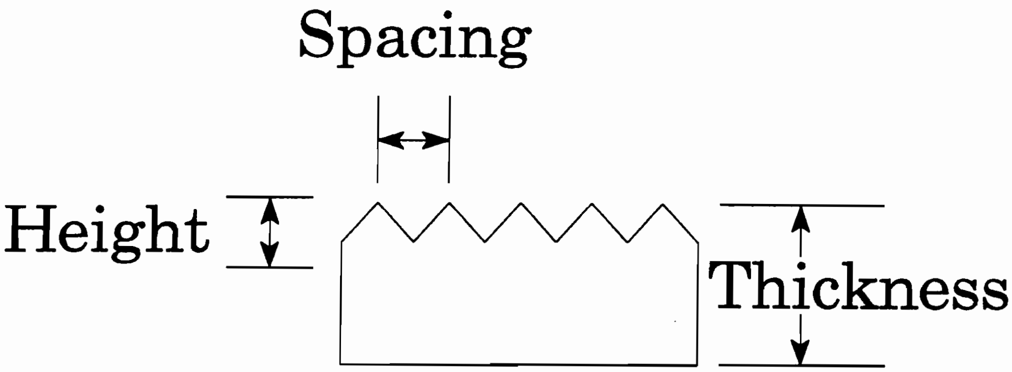

Figure 3.6 Riblet Dimensions

The first stage, designated as the baseline test, involved testing the blades with no material on them. The second and third stages were performed with one and two layers of smooth material on the blades. Next, in the fourth stage, all material was removed from the blades and the baseline test was repeated. The riblet material was applied and tested in the fifth stage. Finally, the bare blade test was repeated to bracket any tunnel variations.

Table 4. Riblet Test Procedure

Stage Number	Description
1	No Material (Baseline)
2	One Layer
3	Two Layers
4	Baseline
5	Riblets
6	Baseline

4.0 Flow Field Description

As described earlier, the test section doors can be rotated to investigate different incidence angles. The major characteristics of the flow field in the STF cascade for design, -10° incidence, and +5° incidence are briefly described below. The flow physics differ for all three incidence angles. Also, the effect of the riblets on the cascade blades' performance varies with incidence angle. The description of the flow field is based on a combination of techniques: surface oil flow visualization, surface pressure measurements, and shadowgraph photography. Additional details on the STF cascade flow field can be found in Chesnakas[13] and Andrew.[15]

4.1 Design Incidence

A schematic of the major flow field features of the STF cascade at design incidence is displayed in Figure 4.1. The Mach number in the STF cascade is 2.36 with a Reynolds number based on chord of 4.8 million. A favorable pressure gradient exist through the blade passage. This limits boundary layer growth and helps prevent massive flow separation. Bow shocks originate at the leading edge of the blade and move downstream into the blade passage where they reflect on adjacent blade surfaces. At design incidence, the blades

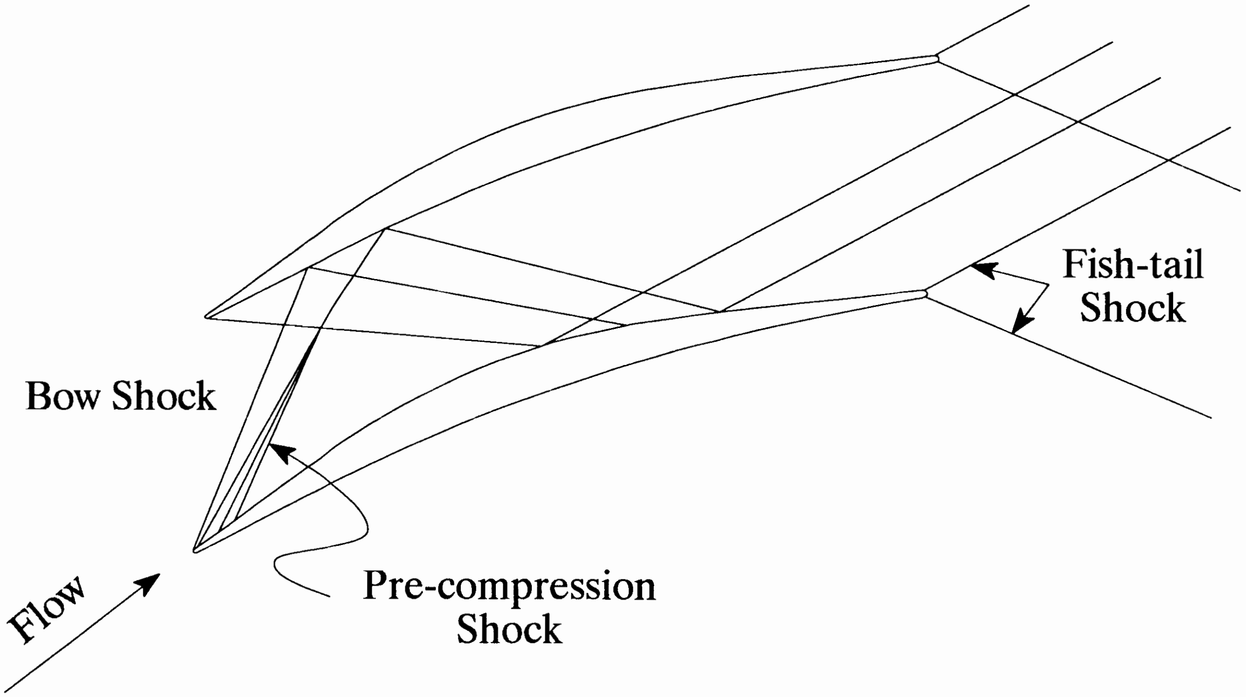

Figure 4.1 Flow Field Description, Design Incidence

are designed to prevent boundary layer separation from the shock-boundary layer interaction. A pre-compression wave forms due to a coalescence of Mach lines above the concave curvature at the leading edge suction surface. This shock reflects from the adjoining pressure surface at 1/4 chord and back to the suction surface near 3/4 chord. At the trailing edge, weak "fishtail" shocks adjusts flow conditions between the suction and pressure side of the blade.

Due to supersonic conditions, the losses in the cascade are the result of both viscous and shock effects. Riblets are effective in reducing viscous losses and therefore are able to decrease only a certain percentage of the total losses in the cascade. Chesnakas[13] developed a method to account for the different loss mechanisms in the STF cascade. At design incidence, Chesnakas estimated the viscous losses to be 33% of the total losses in the STF cascade. At N.A.S.A Lewis Research Center,[61] computational results indicate that the viscous losses are nearly 50% of the total losses in the cascade at design incidence.

4.2 -10° Incidence

The flow field description for the off-design case of -10° incidence is illustrated in Figure 4.2(a). The most noticeable difference between design and -10° incidence is the separation of the boundary layer due to the shock impingement on the blade pressure surface. The shock-separated region is

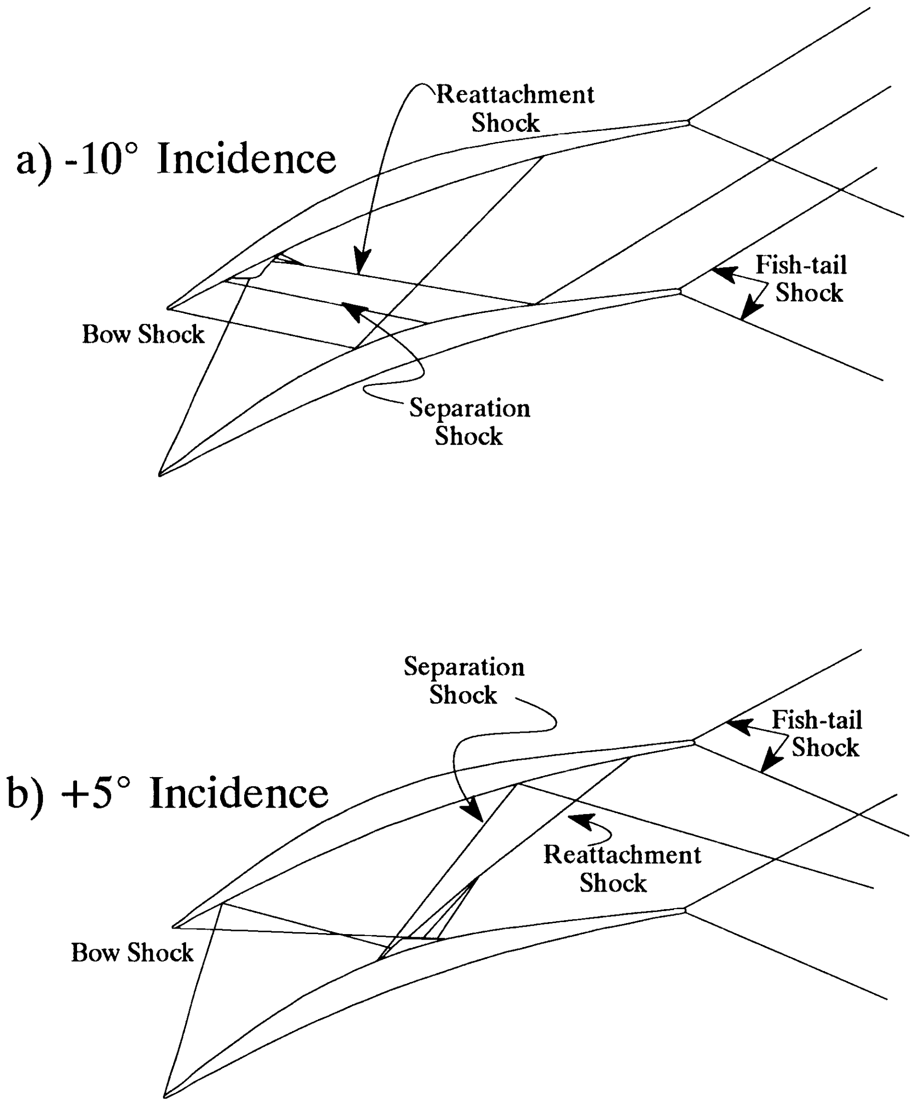

Figure 4.2 Flow Field Description, Off-Design Incidence

located near the leading edge. The separated flow reattaches to the blade surface forming a bubble. This separation bubble is followed by a highly localized adverse pressure gradient on the blade surface. As a result of the shock-boundary layer interaction, a separation shock and reattachment shock are formed and impinge on the opposing suction side blade surface. Viscous losses are calculated to be 17%[13] to 35%[61] of the total losses at the -10° incidence case.

4.3 +5° Incidence

The flow field for the +5° incidence is represented in Figure 4.2(b). Similar to the -10° case, the shock-boundary layer interactions is severe enough to produce a separation bubble in the boundary layer. However for the +5° case, the location of the bubble is at the mid-chord region of the blade's suction surface. The resultant separation and reattachment shocks of the bubble propagate downstream striking the adjoining pressure surface before exiting the blade passage. In the +5° incidence case, 25%[13] to 40%[61] of the cascade losses are estimated to be viscous losses.

5.0 Experimental Results

For the STF cascade riblet study, the riblet effects were evaluated by comparing the mass-averaged loss coefficients of the riblet covered blades to blades having an equivalent layer of smooth material. Downstream total pressure profiles were also compared in order to better understand the riblet effect on the blades. In addition to the riblet study, a separate leading edge study was conducted for the purpose of determining how to interpolate for the equivalent layer of smooth material for the riblet study.

In the riblet study, three different size riblets were investigated at design incidence. All three sizes produced a decrease in losses; however, only the optimum riblet size was investigated at off-design conditions of +5° and -10° incidence. Also examined in the riblet study were shadowgraphs focused on the leading edge of the blades--where the transition of the laminar boundary layer occurred. Unlike conventional riblet studies, the reduced viscous losses in the STF cascade are attributed to two different effects. As will be shown below, the riblets decreased the turbulent viscous losses and also delayed the onset of the turbulent boundary layer on surface of the blades.

5.1 Effect of Leading Edge Thickness on Losses

As described in Chapter 3, the riblet material was applied to the blades by wrapping it around the leading edge. For the enlarged leading edge radius, the losses in cascade increase due to the leading edge bow shock effect. In order to determine the reduction in viscous losses from the riblets, the riblet results were compared to a smooth layer result, with an equivalent leading edge thickness to the riblet material. The method to calculate for an equivalent smooth layer result is presented below.

To determine the effect of an increased leading edge thickness on the losses of the cascade, a number of layers of smooth material were applied only to the leading edge of the blades. The blades were tested with one, two, and three layers of smooth material. For the cascade, a relationship between loss coefficient and number of layers of material was determined for design and off-design incidence angles. The first layer of material was applied to the blade surface at approximately 5% chord on suction surface. The material was wrapped around the leading edge and ended at approximately 5% chord on the pressure surface of the blade. Each additional layer of material overlapped the previously applied layer so that the smoothest possible transition with the blade surface was maintained. The final layer of smooth material covered less than 10% of the chord on each side of the blade surface.

In Figure 5.1, the mass-averaged loss coefficient of the STF cascade blades is shown to increase linearly with increasing leading edge radius. A

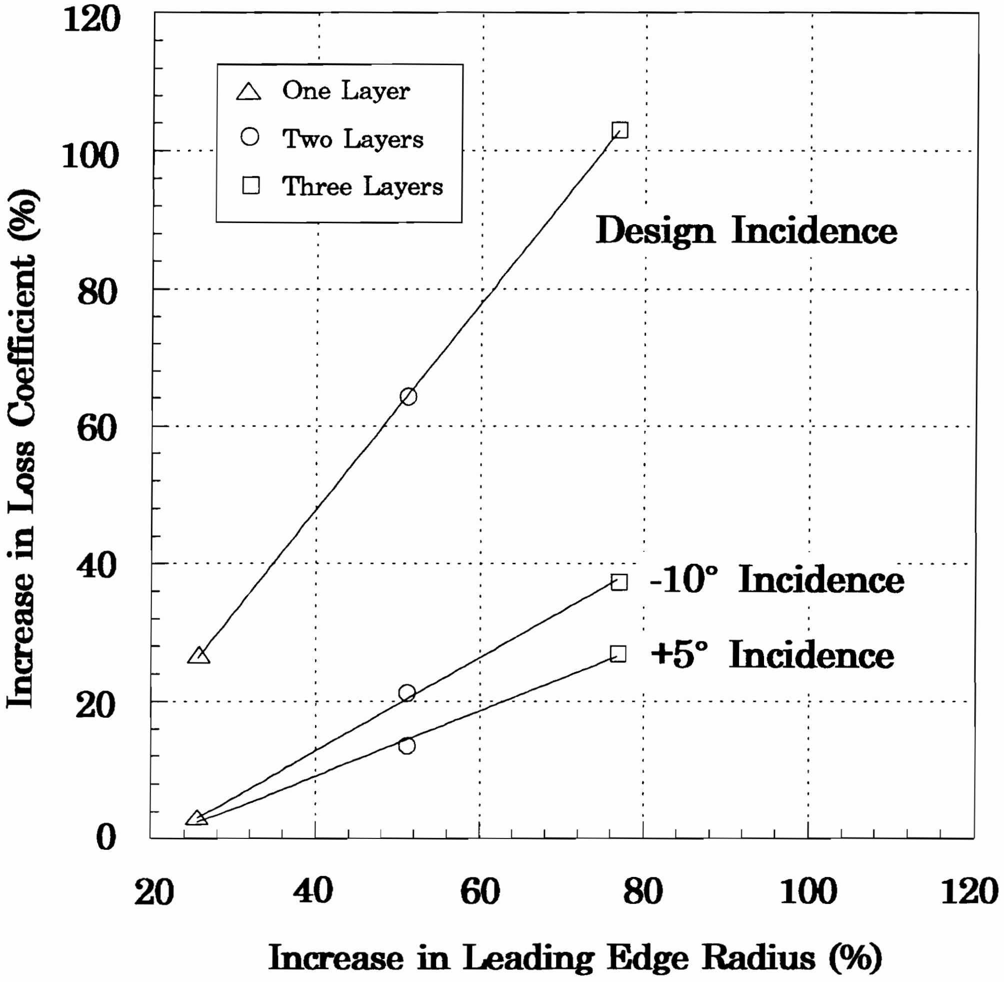

Figure 5.1 Effect of Increased Leading Edge Thickness on Losses

linear effect is seen for design as well as off-design conditions. One significant finding from this study is that a linear interpolation can be used to calculate a smooth layer result, with an equivalent thickness to the riblet material, for use in the riblet study.

Unlike the smooth material, the thickness of the riblet material is not constant and varies by the amount of the riblet height. Therefore, the effect of the riblet material on the leading edge of the blades was investigated. The 0.033 mm riblet material was applied only to the leading edge of the blades and tested at design incidence. Next, the riblet leading edge result was compared to the smooth layer results in order to determine an equivalent smooth layer thickness that produces the same increase in loss coefficient as the riblet material.

Presented in Figure 5.2 are the results of the leading edge study at design incidence, including the riblet leading edge result. The range for the thickness of riblet material is marked on the horizontal axis by the words "base" and "peak". The horizontal line indicates the value for the increase in loss coefficient due to the riblets on the leading edge. As seen in Figure 5.2, the horizontal line intersects the smooth layer results at the riblet "peak" location. This indicates that the best estimate for an equivalent leading edge thickness of the smooth material is the riblet "peak" thickness. Thus all results of the riblet study are based on the equivalent thickness measured to the peak of the riblet.

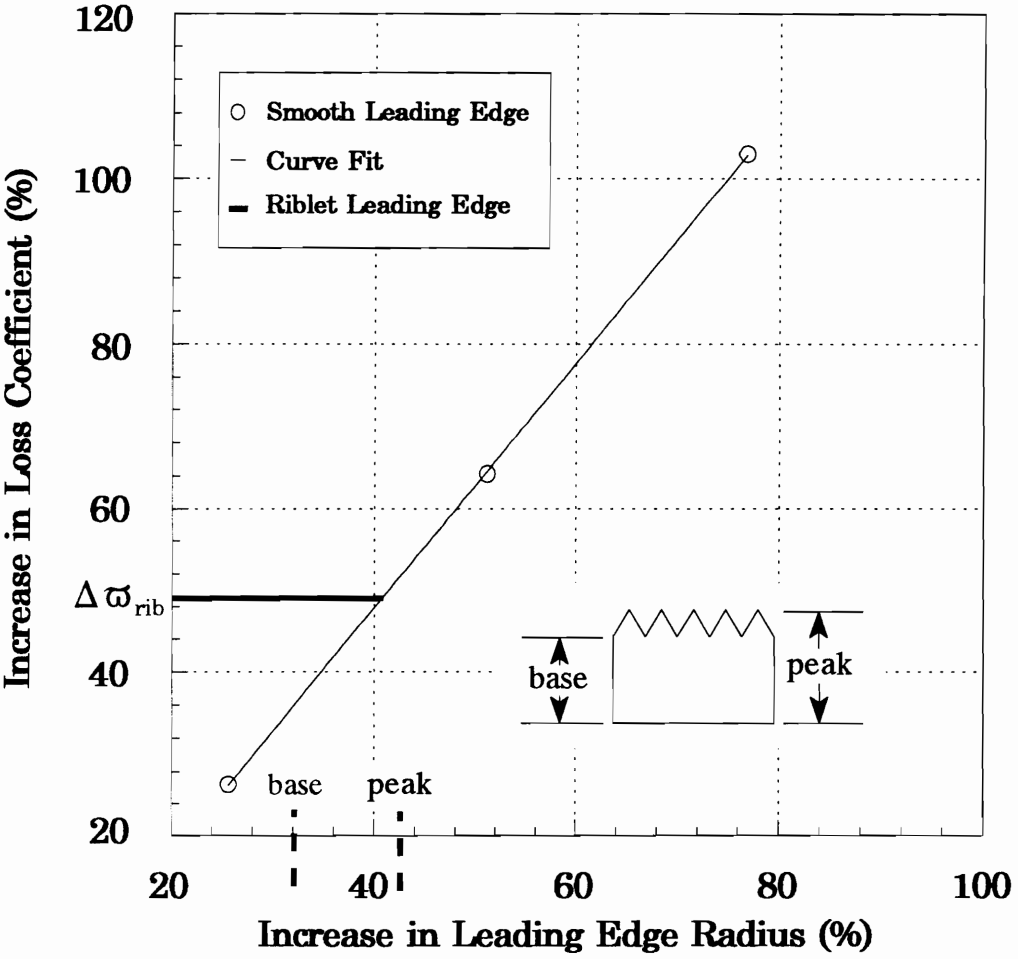

Figure 5.2 Equivalent Riblet Leading Edge Thickness

5.2 Effect of Riblet Height on Loss Reduction

For the riblet height study, three different riblet heights were tested at design incidence: 0.023 mm, 0.033 mm, and 0.051 mm. These were the only commercially available sizes that have shown to reduce viscous losses in previous supersonic riblet studies. For the three sizes tested in the STF cascade, the 0.033 mm height riblet material provided the optimum benefit, with a reduction in mass-averaged loss coefficient, $\Delta\varpi$, of 8.5%. The reduction in mass-averaged loss coefficient was defined as:

$$\Delta\varpi = \frac{\varpi_{riblet} - \varpi_{smooth}}{\varpi_{smooth}} \tag{5.1}$$

The uncertainty of the results was ±2% and was based on the uncertainty of the calculated loss coefficient for consecutive runs with similar testing conditions. More information on the uncertainty analysis is presented in Appendix A. For a later tunnel entry, the repeatability of this experiment was shown to be very good and within the ±2% uncertainty band.

As described in Chapter 2, a wide range of riblet heights will produce a decrease in viscous losses. Presented in Figure 5.3(a) is the results, with their uncertainty band, for the three sizes tested in the STF cascade. The maximum benefit of 8.5% occurs at the intermediate height tested of 0.033 mm. Smaller

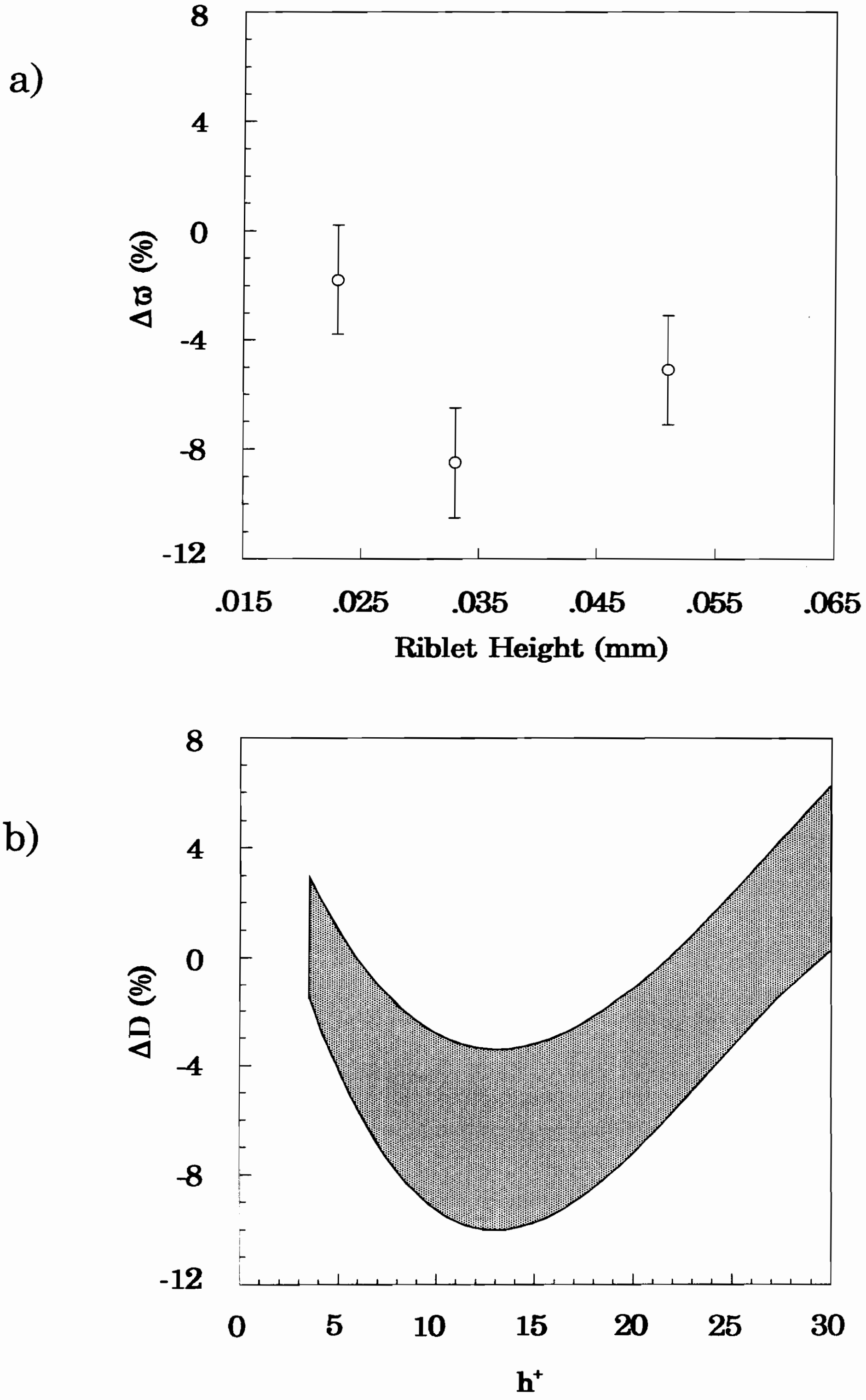

Figure 5.3 Effect of Riblet Height on Loss Coefficient

benefits of 1.8% and 5.1% result from the 0.023 mm and 0.051 mm height riblets, respectively. In Figure 5.3(b), the general riblet performance trend from previous studies found in Figure 2.3 is presented. The STF riblet height results demonstrate a comparable trend to previous riblet results and illustrates the importance of choosing the appropriate riblet height for the STF cascade.

In addition to the riblet height study, a Reynolds number study was conducted in the STF cascade. Here, the 0.033 mm riblets were tested at different total upstream pressures and compared to equivalent smooth layer results. The purpose of this study was to change the local h^+ parameter on the blade's surface without modifying the physical height of the riblets. The results from this study show the same trend as the riblet height study. Details for the Reynolds number study are provided in Appendix B.

The comparison of the mass-averaged loss coefficient provides an assessment of the overall performance of the riblet covered STF cascade; however, it does not indicate where the benefit occurs. To better understand the riblet effect on the STF cascade blades, total pressure profiles of the riblet and equivalent layer of smooth material are compared.

It should be pointed out again that the equivalent smooth layer result is an interpolation between the results of one and two layers of smooth material. As shown in Appendix C, any increase in the leading edge thickness of the STF blades will move the bow shocks impingement location on the blade surfaces and, as a result, the location of the reflective shocks in the probe survey. When the reflected shock encounters the Pitot-static probe, the shock wave disrupts the flow around the probe.[13] This appears as a decrease or small dip in the total pressure profile. Due to the interpolation of the total pressure profile, the comparison between the riblet and equivalent smooth layer total pressure profiles does not produce all the details. However, some general observations can still be made from the comparison.

The optimum riblet height of 0.033 mm and the equivalent layer of smooth material profiles are shown in Figure 5.4. The total pressure profiles are nondimensionalized by the total pressure measure upstream of the STF cascade test section. The traverse location, y, is nondimensionalized by inter-blade spacing S. The profiles consist of a pitch-wise traverse at an axial location of x/C=0.37 downstream of the cascade blades. The profile starts at a location of y/S=-0.5 in the core flow and moves toward the pressure surface side of the wake. At y/S=-0.28 in the profile, the location of the "fishtail" shocks are indicated by the small spike in the total pressure profile. Finally, the profile passes through the blade wake and ends in the core flow region above the suction surface of the wake at y/S=0.5.

The total pressure profile comparison in Figure 5.4(a) demonstrates that the riblets provide a reduction in mass-averaged loss coefficient. The higher values of total pressure in the riblet profile is indicative of lower losses. The only two regions where the riblet profile is lower than the smooth layer are at

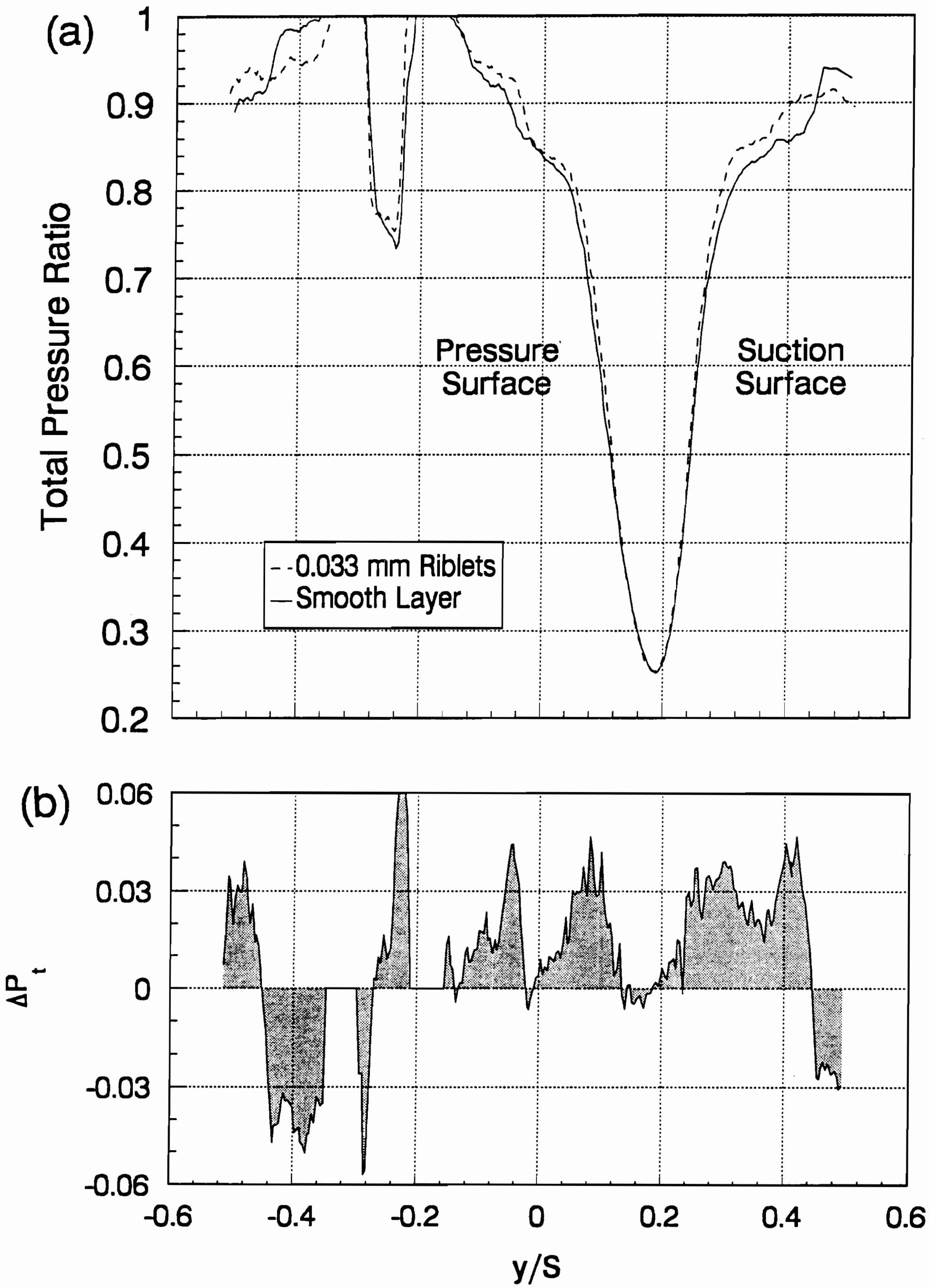

Figure 5.4 Total Pressure Profile Comparison, Design Incidence

y/S=-0.5 and y/S=0.44. In the riblet profile, these are the locations of the reflected shocks. Small changes in the total pressure are present throughout the profiles; both in the wake and core flow regions. Through the integration of the profiles, the total difference in loss coefficient amounts to 8.5%.

Due to the steep gradient in the wake region of the total pressure profiles, the amount of change between the two profiles is difficult to distinguish. Presented in Figure 5.4(b) is the difference in total pressure, Δp_t, between the riblet and the equivalent smooth layer in the survey. Positive values of Δp_t indicate a local riblet benefit. Clearly most of the net gain from the riblet effect is seen in the wake region. However at the wake minimum location of y/S=0.19, very little difference exist between the two profiles. Most of the riblet effect in the wake region is seen on either side of the wake minimum. This indicates that the riblets are effective in reducing viscous losses on both the pressure and suction sides of the blade.

For the 0.023 mm and 0.051 mm height riblets, a smaller effect was seen in the comparison of the total pressure profiles. These results are presented in Appendix D.

5.3 Off-Design

The off-design cases of +5° and -10° incidence were tested with the optimum riblet height of 0.033 mm. As described earlier, the flow physics inside the STF cascade significantly changes at the off-design conditions. Due to changes in the flow field, the riblets' effect on the performance of the cascade blades also differs from the design incidence result.

The effect of the riblets on the STF cascade blades for the off-design study are presented in Table 4. A small benefit of 2.5% is provided by the riblets at +5° incidence. A drawback of 3.0% is seen for the -10° incidence. Compared to the benefit provided by the riblets at design incidence, the riblet effect is small. To better understand the difference in the riblets' effects for the off-design cases, total pressure profiles of the riblet and equivalent layer of smooth material are compared.

Table 5. Off-design Results

Incidence	**Change in ϖ (%)**
+5°	-2.5
0°	-8.5
-10°	3.0

For the +5° incidence, the total pressure profile comparison is presented in Figure 5.5. A 2.5% reduction in mass-averaged loss coefficient for the riblet covered blades is calculated for this off-design case. In the wake region, the

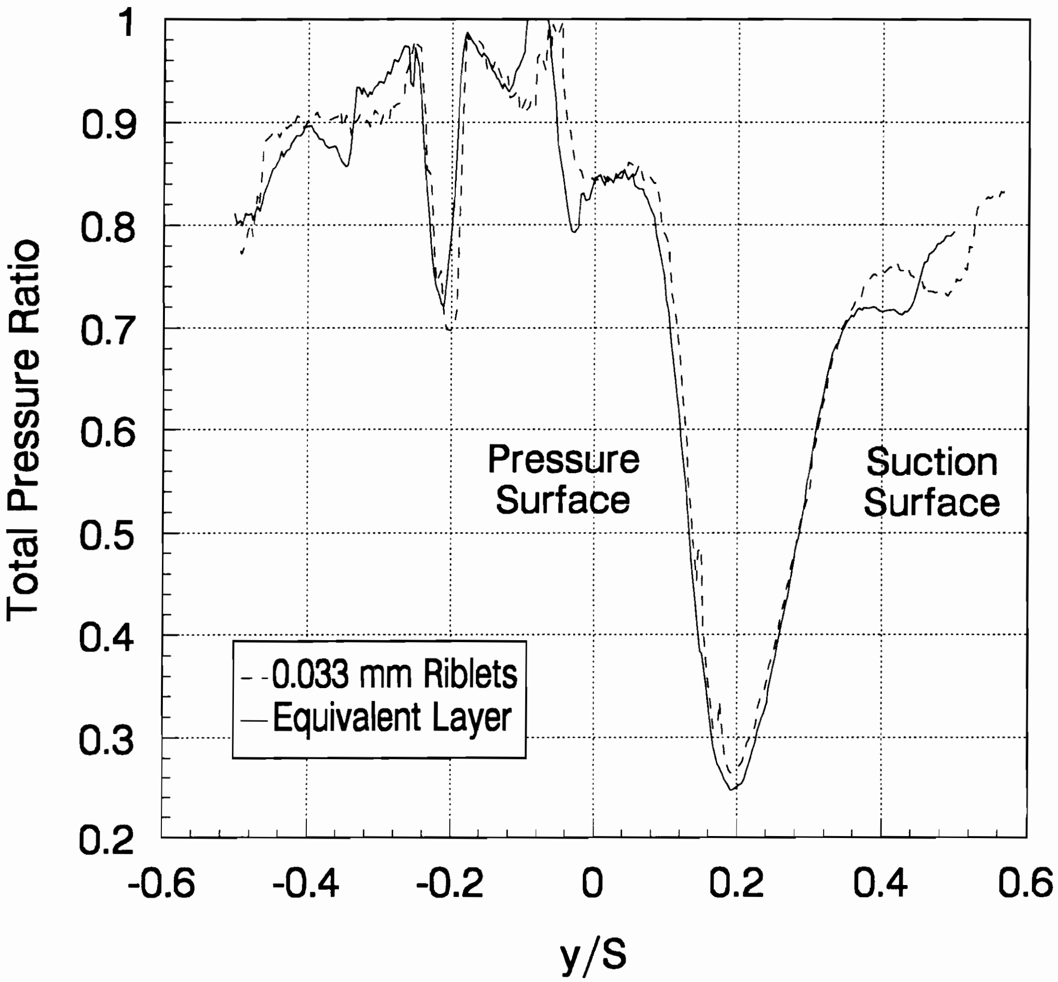

Figure 5.5 Total Pressure Profile Comparison, +5° Incidence

amount of riblet benefit differs between the suction and pressure side. Only a small difference between the profiles exist on the suction side of the blade wake as compared to the pressure side. This seems to indicate that the riblet size on the blade pressure surface is no where near an optimum height. In the core flow region between y/S=0.36 and y/S=0.52 are consecutive dips in the profiles; the first occurs in the equivalent layer and the second in the riblet profile. As described earlier, the shift in the dip location is a result of the movement of the reflective shock.

Unlike the case of +5° incidence, the riblets' effect at -10° incidence produced an increase in losses. The comparison between the total pressure profiles is presented in Figure 5.6. Recall at -10° incidence, the flow field is characterized by a shock-separated boundary layer region and localized adverse pressure gradient on the pressure surface of the blade. In Figure 5.7, the location where the riblet profile is considerably lower than the smooth layer profile is in the outer fraction of the pressure side of the wake, y/S=0.0 to -0.2 region. As described by Andrew,[15] this is the location where the boundary layer-separation effects appear in -10° incidence downstream profiles. Therefore, it is hypothesized that the presence of the riblets in the separated boundary layer region contributes to the 3% increase in mass-averaged loss coefficient.

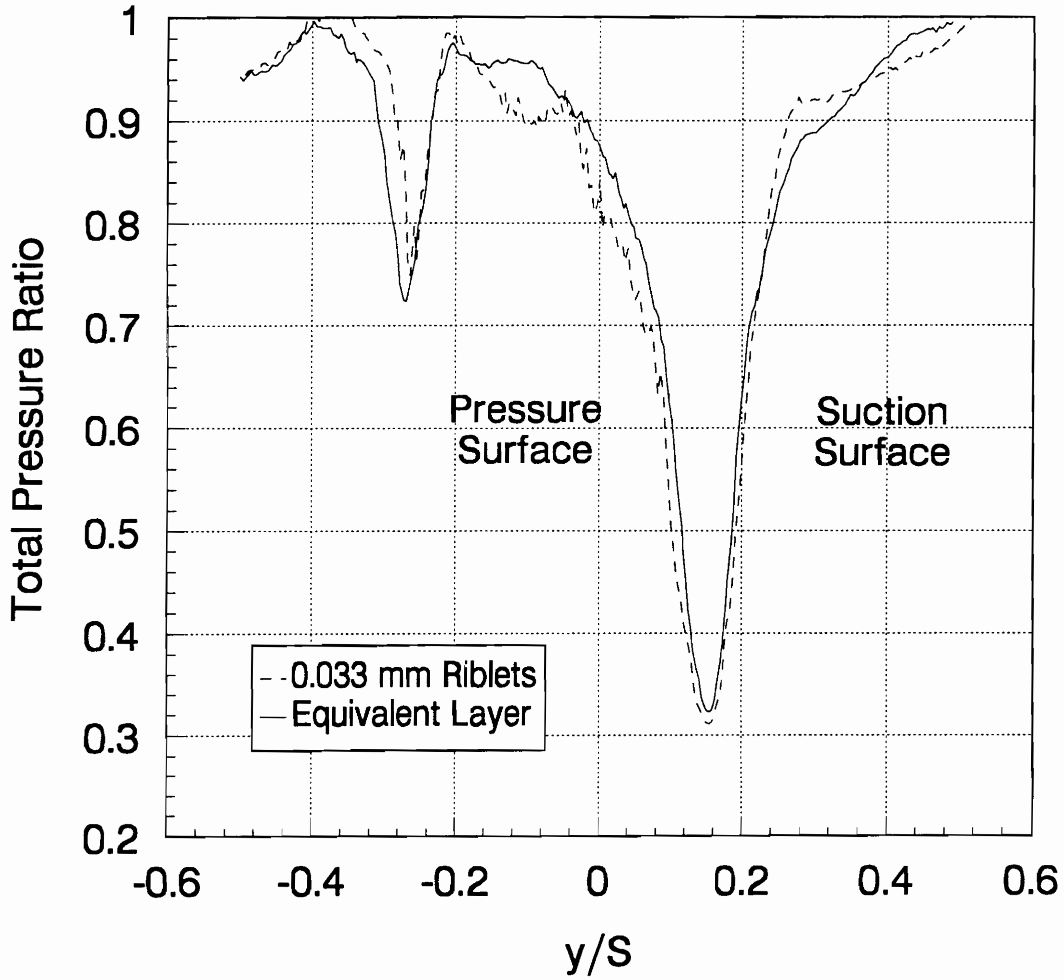

Figure 5.6 Total Pressure Profile Comparison, -10° Incidence

5.4 Influence of Yaw Angle

In actual turbomachinery, riblets would encounter 3-D flow effects on the blade surface. Therefore the effect of riblet misalignment to the mean flow direction, yaw angle, was investigated in the STF cascade. In this study, the optimum riblet height material was applied to the blades at 15° off the mean flow direction and tested at design incidence.

The results from this study, along with previous riblet yaw studies, are presented in Figure 5.7. Indicated on the horizontal axis is the yaw angle, α. The vertical axis is defined as change in riblet effect, from yaw effects, divided by the maximum riblet benefit. The maximum riblet benefit occurs at α=0°. In all previous studies, the riblet effect is defined as a change in drag, ΔD. For the STF study, the riblet effect is described as a change in loss coefficient, $\Delta\varpi$.

As indicated in the figure 5.7, most of the earlier riblet yaw studies were conducted on a flat plate. The trend shows that the riblet benefit diminishes as yaw angle increases. At yaw angles greater than 30°, the results from the riblet yaw studies no longer show a riblet benefit and, in fact, most studies exhibit an increase in the viscous losses when compared to a smooth surface. For the STF cascade study, the yaw effects are consistent with the these earlier studies. At 15° yaw, most of the 8.5% benefit seen for this optimum riblet height is lost.

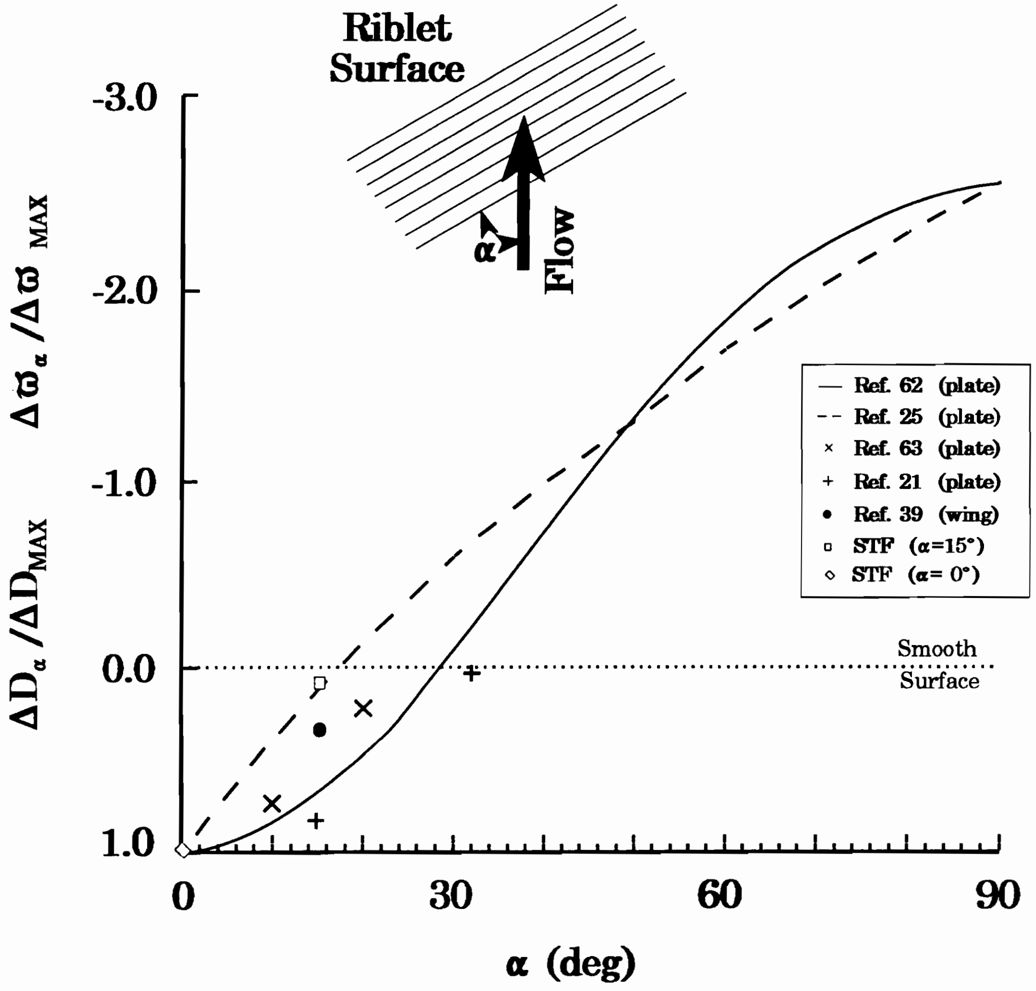

Figure 5.7 Yaw Effects on Riblet Performance

5.5 Leading Edge Shadowgraph

The losses in the STF cascade are the result of both shock and viscous effects. Therefore, the maximum 8.5% decrease in loss coefficient represents a significantly greater reduction in the viscous losses. As described in Chapter 4, the viscous losses in the cascade at design incidence are no more than 1/2 of the total losses. Taking into account the increase in losses due to the enlarged leading radius of the blades from the riblet material, the 8.5% decrease in the total loss coefficient corresponds to approximately a 25% decrease in the viscous losses. This is much greater than the 10% decrease in turbulent viscous losses that has been reported by other researchers and suggests that the riblets are decreasing the viscous losses in another manner. As a result, the effect of riblets on transition location on the blade surfaces was investigated.

As described earlier, very little research concerning the influence of riblets on the transition of a laminar boundary layer has been conducted. In previous shadowgraphs of the STF flow field,[14] the location of transition was difficult to determine as the developing boundary layer is thin. Therefore, new shadowgraphs were taken that focused on the leading edge of the two middle blades in the cascade.

Three different testing conditions were examined for the shadowgraph study. Shadowgraph pictures were taken of the two blades covered with smooth material and covered with riblet material. Also a shadowgraph picture with one blade covered with smooth material and the other covered with riblet material was taken. This was done to ensure that any movement in the transition location was due to the material on the blades and not to any variations between the different tunnel runs.

To illustrate the effect of riblets on transition, only one shadowgraph picture is presented here. Shown in Figure 5.8 is a shadowgraph focused on the leading edge of the two STF blades located in the middle of the cascade. The top blade, as marked, has a smooth covered surface. The 0.033 mm riblet material covered the lower blade. The circular objects in the shadowgraph are the pins used to support the blades to the plexiglass windows. Since this a copy of the original picture, the transition locations on the surface of the blades surfaces is difficult to see.

In Figure 5.8, it appears that the smooth surface blade shows transition has begun on the suction side of the smooth surface blade at the approximate location of 15% chord. On the riblet covered blade, there is no apparent sign of turbulent structure near the blade's pressure surface at this location. The transition location on the suction side of the riblet covered blades is difficult to determine. However, it appears that the boundary layer may continue to be laminar on the suction side until it approaches the location where the shock impinges the blade at approximately 50% chord. On the pressure surface, the transition location is approximately 10% chord for both the riblet and smooth

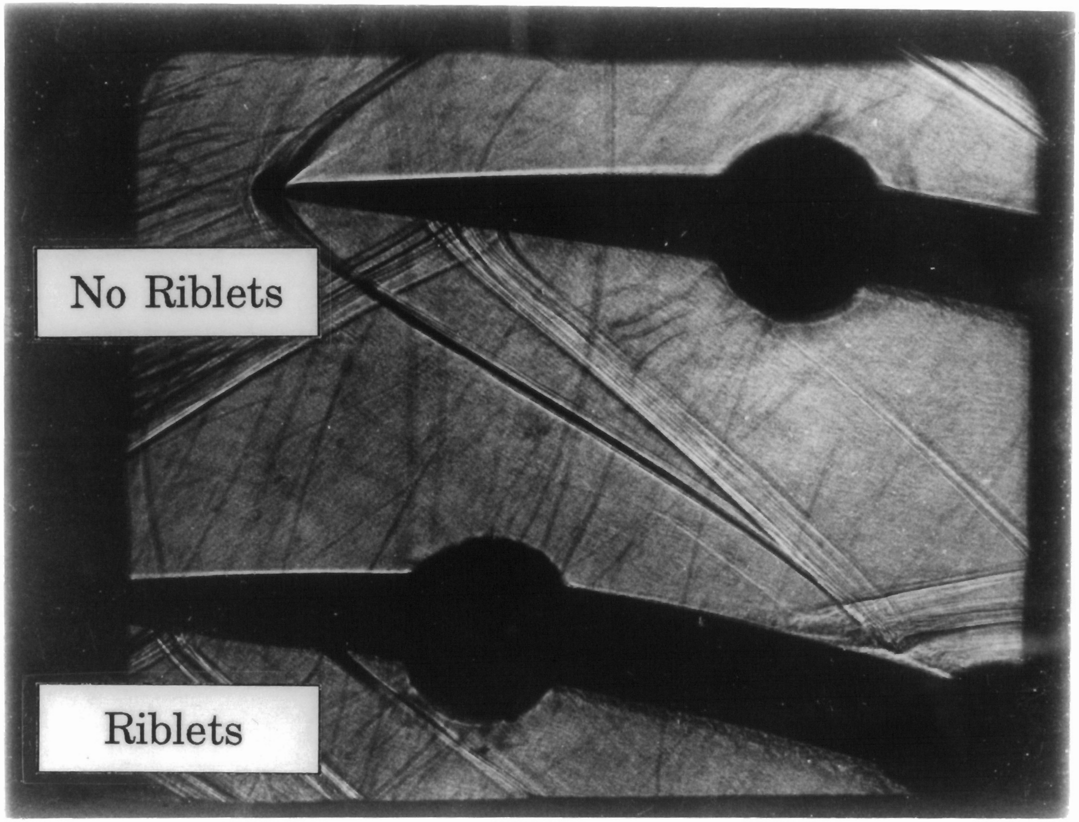

Figure 5.8 Shadowgraph of Leading Edge Boundary Layer, Design Incidence

surface blades. This is due to the fact the bow shock impinges the pressure surface at this location and initiates the turbulent boundary layer.

It is hypothesized that riblets are able to dampen the original disturbances that lead to transition in the STF cascade blades. Possibly, the slow moving fluid inside the riblet grooves is sustaining the laminar boundary layer. At design incidence, the pressure gradient on the blade's suction surface becomes favorable around 20% chord and continues until the shock impingement location at 50% chord. Perhaps, the combination of the riblets and the favorable pressure gradient on the blade surface is responsible for the laminar boundary layer existing up to the shock impingement location. For the smooth blade surface, the boundary layer is already turbulent at 20% chord and the mild pressure gradient would effect the turbulent boundary layer by only minimizing it growth.

Obviously, preserving the laminar boundary layer further downstream on the STF blade surface will lower the viscous losses. Evidence from the shadowgraph indicates that the riblets are providing another drag reducing functions on the STF blades. In additional to reducing the turbulent viscous losses, riblets are able to delay the transition location of the turbulent boundary layer on the STF blades. As will be shown in the numerical simulation section of this paper, only the combination of the two riblet effects reproduced the substantial decrease in losses that were measured for the optimum, 0.033 mm, riblet size at design incidence.

6.0 Numerical Simulation

Experimentally, two different riblet effects were observed on the STF blades: a reduction in turbulent viscous losses and a delayed transition location of the turbulent boundary layer. In the numerical simulation, the two riblet effects were studied separately in order to determine the contribution from each riblet effect on the total decrease in losses. The delayed transition effect was established by initiating the turbulent boundary layer further downstream on the blade's suction surface in the simulation. Modelling for the decrease in turbulent viscous losses required modifying the existing turbulent model. The numerical simulation focused on the flow field for design incidence, with an emphasis for modeling the situation where there is an optimum riblet benefit.

First, a brief description of the CFD code and mesh used in the simulation is provided. Next, the original Baldwin-Lomax turbulent model is presented. This is followed by a description of the method to include riblet effects in the Baldwin-Lomax model. Finally, the method used to simulate the delayed transition effect on the boundary layer is described.

6.1 Numerical Model

The code used to calculate the STF cascade flow field was ANSERS (**A**lgorithm for the **N**avier-**S**tokes **E**quations using a **R**eimann **S**olver) developed by Thomas and Walters.[64] Significant improvements to the original code have been developed by Taylor,[65] Brock,[66] and Andrew.[15] In ANSERS, the compressible, two-dimensional, full Reynolds-averaged Navier-Stokes equations are solved by a time marching method. The integral conservation law form of the governing equations are solved with a cell-centered finite-volume formulation. The upwind scheme of Roe[67] was used to evaluate the inviscid flux terms. The viscous fluxes were determined by a second-order accurate central differencing method.

A periodic C-mesh was used to model the STF cascade blade. The mesh was generated with an elliptic grid generator developed by Sorenson.[68] The grid, shown in Figure 6.1, contains 481 cells in the stream-wise direction and 61 cells in the pitch-wise direction. Grid points are closely packed to the blade surface with additional points concentrated near the leading and trailing edges to ensure proper resolution of the flow physics.

Figure 6.1 STF Fan C-grid

6.2 Turbulent Model

The Baldwin-Lomax[69] turbulent model was used to provide closure for the ANSERS code. This model was chosen for to its robustness and ease of implementation. The Baldwin-Lomax model is an algebraic eddy viscosity model which handles the turbulent boundary layer as a composite of two layers; an inner and outer region. To model for a reduction in turbulent viscous losses, one parameter in the turbulent model was modified. Presented first is a description of the original turbulent model. This will be followed by the formulation to include riblet effects in the Baldwin-Lomax model.

6.2.1 Original Baldwin-Lomax Model

Inner Region

The Van Driest formulation of the eddy viscosity is used in the inner region:

$$(\nu_t)_i = (\kappa \, y_n \, D)^2 \; |\omega| \tag{6.1}$$

where κ is the von Kármán constant, equal to 0.4. y_n is the normal distance from the wall and ω is the vorticity. The Van Driest damping factor, D, is defined as:

$$D = 1 - \exp\left(-\frac{y^+}{A^+}\right) \tag{6.2}$$

where for a smooth surface A^+ is 26 and y^+ is defined as:

$$y^+ = \frac{\rho\, u_\tau\, y_n}{\mu} \tag{6.3}$$

The friction velocity, u_τ, in the above equation is defined as:

$$u_\tau = \sqrt{\frac{\mu_w}{\rho_w}\frac{\partial u}{\partial y}\bigg|_w} \tag{6.4}$$

Outer Region

In the outer region, the eddy viscosity is defined as:

$$(\nu_\tau)_o = K\, C_{cp}\, F_{wake}\, \gamma \tag{6.5}$$

where the Clauser constant, K, is equal to 0.168 and C_{cp} is equal to 1.6. The F_{wake} parameter is defined as the minimum of the two formulas:

$$F_{wake} = \frac{C_{wk}\, y_{max}\, U^2{}_{diff}}{F_{max}} \quad or \quad F_{wake} = F_{max}\, y_{max} \tag{6.6}$$

The value of the constant C_{wk} is 1.0. The value of F_{max} and Y_{max} in wall bounded flows are calculated from the moment-of-vorticity equation:

$$F(y) = y_n \, |\omega| \, D \tag{6.7}$$

For wake flows, the Van Driest damping factor, D, in the above equation is equal to 1.0. The maximum value of the moment-of-vorticity for a given stream-wise station is defined as F_{max}. Y_{max} corresponds to the traverse location of the F_{max} value. The magnitude of the velocity difference between the maximum and minimum for a given stream-wise location is shown as:

$$U_{diff} = U_{max} - U_{min} \tag{6.8}$$

Note that the value of U_{min} is zero for wall bounded flows due to the no-slip boundary condition. The Klebanoff intermittency function, γ, is defined as:

$$\gamma = \left(1 + 5.5 \left(\frac{C_{kleb} \, y_n}{y_{max}}\right)^6\right)^{-1} \tag{6.9}$$

with the value of C_{kleb} equal to 0.3.

The complete profile of the eddy viscosity, ν_τ, at a given stream-wise location is given by:

$$\nu_\tau = \left\{ \begin{array}{ll} (\nu_\tau)_i & 0 \leq y_n \leq y_c \\ (\nu_\tau)_o & y_c \leq y_n \end{array} \right\} \tag{6.10}$$

where y_c is the smallest value of y_n at which the values from the inner and outer formulations are equal.

6.2.2 Riblet Turbulent Model

A method to simulate the riblet effects on the STF cascade blades was developed for the Baldwin-Lomax turbulent model. Rather than physically model the riblets themselves, the turbulent model was modified to simulate for a decrease in turbulent viscous losses by adjusting the A^+ parameter in the Van Driest damping factor equation (Eqn. 6.2). This idea for modelling the riblet effect is based on the work conducted by Schetz and Nerney[70], who successfully modeled surface roughness effects with the Reichardt turbulent model.

As addressed in Chapter 2, the riblets' effects in a turbulent boundary layer are a reduction in viscous losses and a corresponding shift in the law of the wall profile. As illustrated in the law of the wall plot in Figure 6.2, riblets act like "negative roughness" with a shift upward and to the left from the smooth surface profile in the logarithmic region. On the other hand, an increase in drag, from roughness effects, produces a shift downward and to the right. The slope of the lines for both roughness and riblets effects, however, remains the same as the smooth surface line.[28,71]

In the Van Driest damping factor equation, the A^+ value of 26 was chosen because it provided the best agreement with the experimental, smooth surface law of the wall profiles. For the same reason, different values of A^+ can be used to describe the micro-surface effects on a turbulent boundary layer

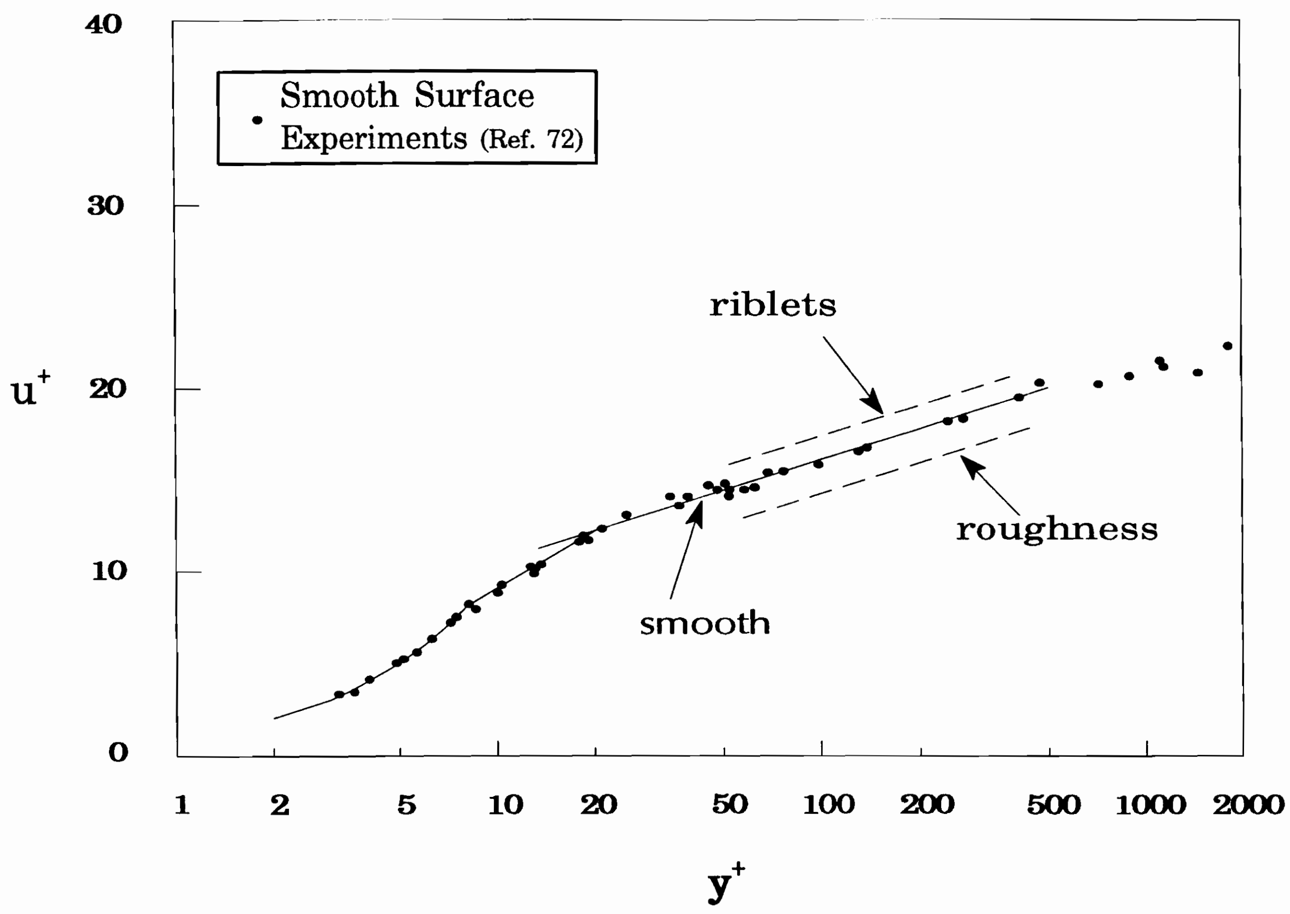

Figure 6.2 Surface Effects on the Wall of the Law Plot

profile. When comparing with smooth surface results, higher values of A^+ would represent a reduction in viscous drag and lower values would represent an increase viscous drag.

To determine the influence of different A^+ values on a turbulent boundary layer profile, a numerical flat plate simulation, with zero pressure gradient, was conducted. The inflow conditions for the flat plate simulation were the same as the supersonic through-flow cascade. For the flat plate study, the range of A^+ values varied between 24 and 37. Starting with an A^+ of 24 in the Van Driest damping equation, the flat plate simulation was computed. The calculated viscous drag was compared to the smooth surface result (A^+=26). Next, the A^+ value was incremented by one and the simulation was repeated. This procedure continued until the change in viscous drag, ΔD, was determined for the complete range of A^+ values.

The flat plate simulation results, relating A^+ to ΔD, are presented in Figure 6.3. For the range of A^+ values investigated, a near linear effect is seen in the change in viscous drag. Compared to the smooth surface result, the A^+ value of 24 produces a 2.4% increase in viscous losses. On the other hand, the A^+ value of 37 decreases the viscous losses by 10.9%. As will be shown later in this chapter, the range of A^+ values and their corresponding changes in drag are used to simulate the varied riblet effect on the blade surface.

The modification to the A^+ parameter in the Baldwin-Lomax model can reproduce the riblet effects on a turbulent boundary layer. To illustrate this

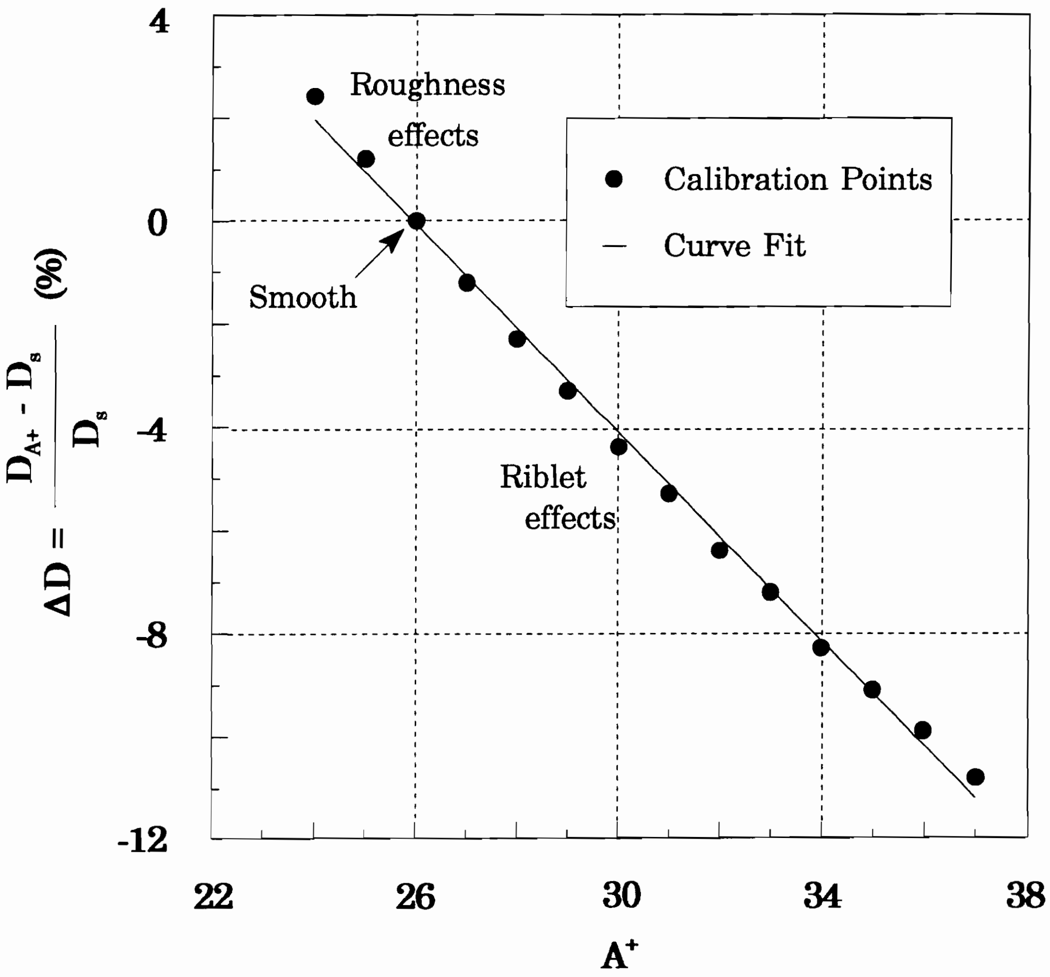

Figure 6.3 A$^+$ vs. ΔD, Flat Plate Simulation

point, profiles of the law of the wall for different values of A^+ are presented in Figure 6.4. By increasing the A^+ value, the wall law profiles in the logarithmic region are shifted upward. This change in the law wall profiles coincides with the experimental riblet results.[28,43] In another illustration, shown in Figure 6.5, a comparison of the riblet effect between experimental and numerical boundary layer profiles are introduced. The experimental velocity profiles are the result of a riblet study on a 1/3 model of the racing yacht "Australia II".[43] The numerical profiles were generated in the above flat plate simulation. Both the experimental and numerical results show a similar riblet effect which confirms the validity of the numerical riblet model. In the turbulent boundary layer, the difference between the riblet and a smooth surface velocity profile is seen only in the near wall region.

Unlike the flat plate study, the STF cascade simulation will not have a constant riblet effect--constant A^+ value--over the blade surface. Due to the flow conditions in the STF cascade, the local riblet effect will vary along the blade surface. In the STF simulation, an estimated h^+ profile on the blade surface is calculated to help determine the localized riblet effect. Recall from Figure 2.3, previous riblet studies show a trend for h^+ parameter versus change in viscous drag. This information is used to model riblet effects by developing a relationship between the riblet height parameters, h^+, and the modified Van Driest parameter, A^+.

The procedure to relate values of h^+ to A^+ requires matching the change

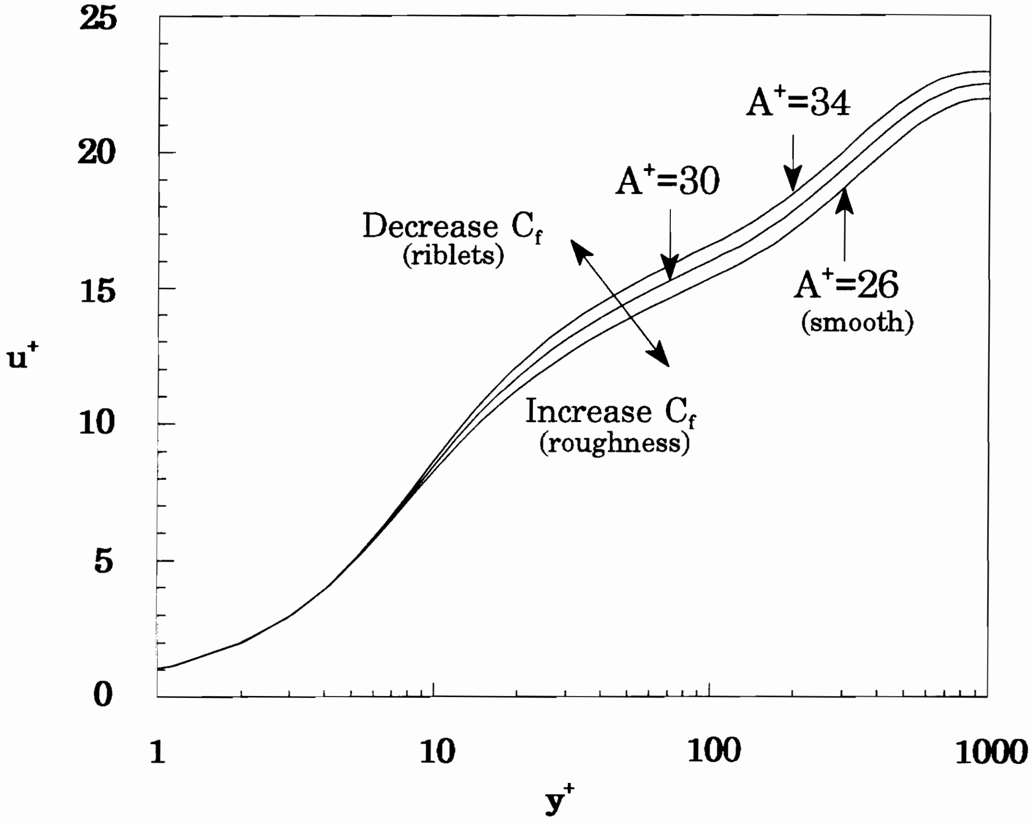

Figure 6.4 A$^+$ Effect on Law of the Wall

a) Experimental

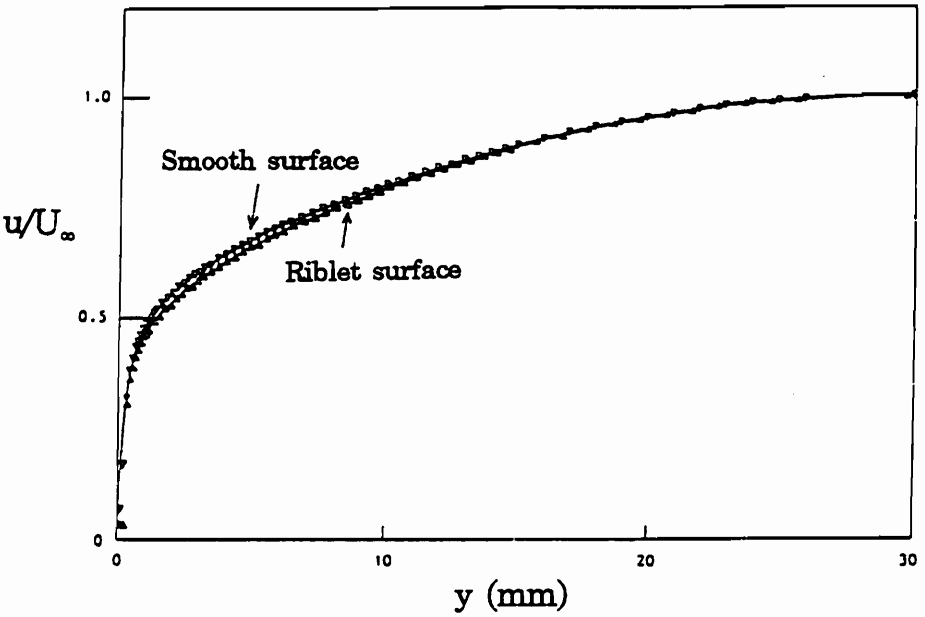

b) Numerical

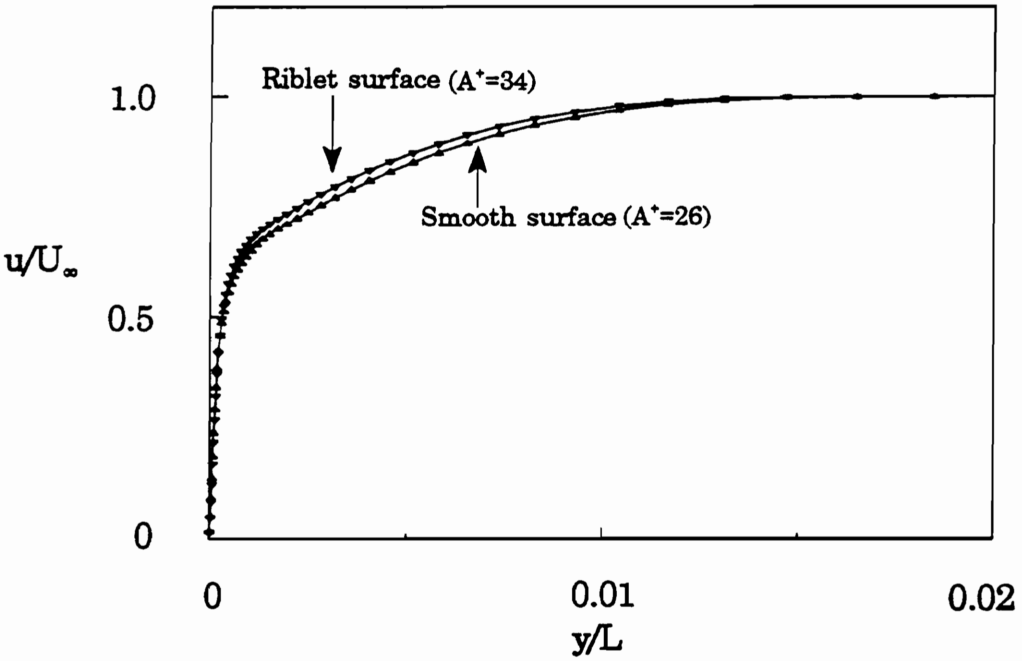

Figure 6.5 Riblet Effect on Velocity Profiles Comparison

in viscous drag, ΔD, from the h^+ trend found in Figure 2.3 with the flat plate simulation results. A flow chart of the process is shown in Figure 6.6. Figure 6.6(a) is the riblet trend from figure 2.3. The curve with the greater drag reduction from the riblet trend data was used in order to produce an optimum benefit for the STF simulation. Recall that the bottom curve has a maximum reduction of 10% at approximately an h^+ of 13 and shows a drag increase for riblets higher than an h^+ of 30. Figure 6.6(b) is the result of the flat plate simulation which relates the A^+ parameter to change in drag, ΔD.

The relationship between A^+ and h^+ used in the STF numerical simulation is presented in Figure 6.7. Below an h^+ of 3.5, the surface is considered to be hydraulically smooth and therefore the value of A^+ was set equal to the smooth surface value of 26. The maximum value of A^+ of around 35.8 is seen at the optimum riblet height, h^+, of 13.

The process for simulating the riblet effect for a decrease in viscous losses involves a number of steps. First, the flow field for smooth blades, $A^+=26$, is simulated. With the smooth blade results, an estimated h^+ profile of the blade surface for an optimum riblet height is computed. A corresponding A^+ profile is generated from the Figure 6.7 and then placed into the CFD code. The flow field for the local riblet effect is then calculated.

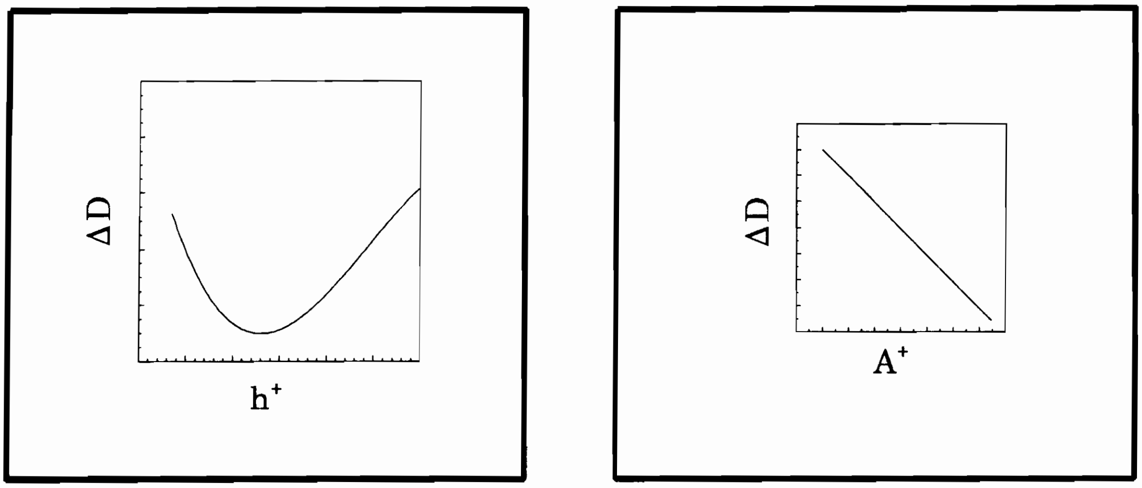

a) from Figure 2.3

b) from Figure 6.3

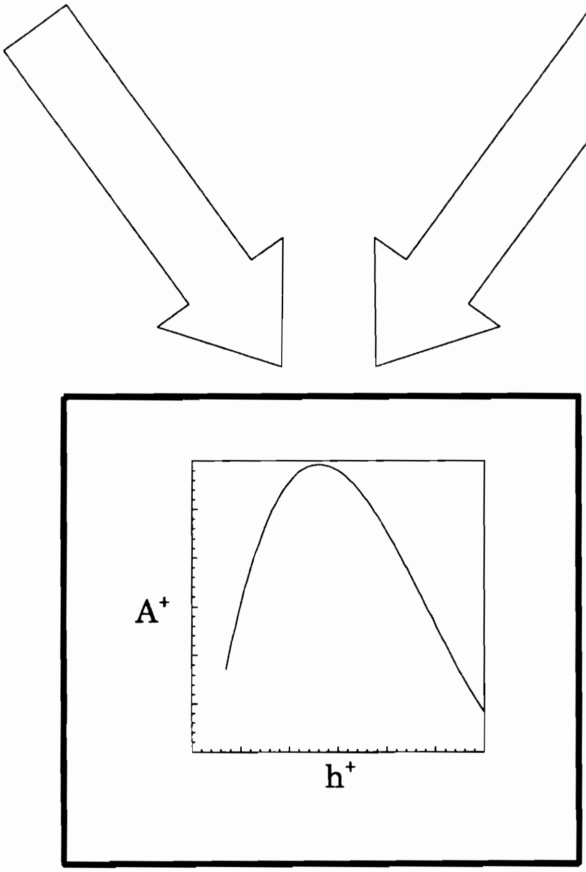

c) h^+ vs. A^+

Figure 6.6 h^+ vs. A^+, Flow Chart

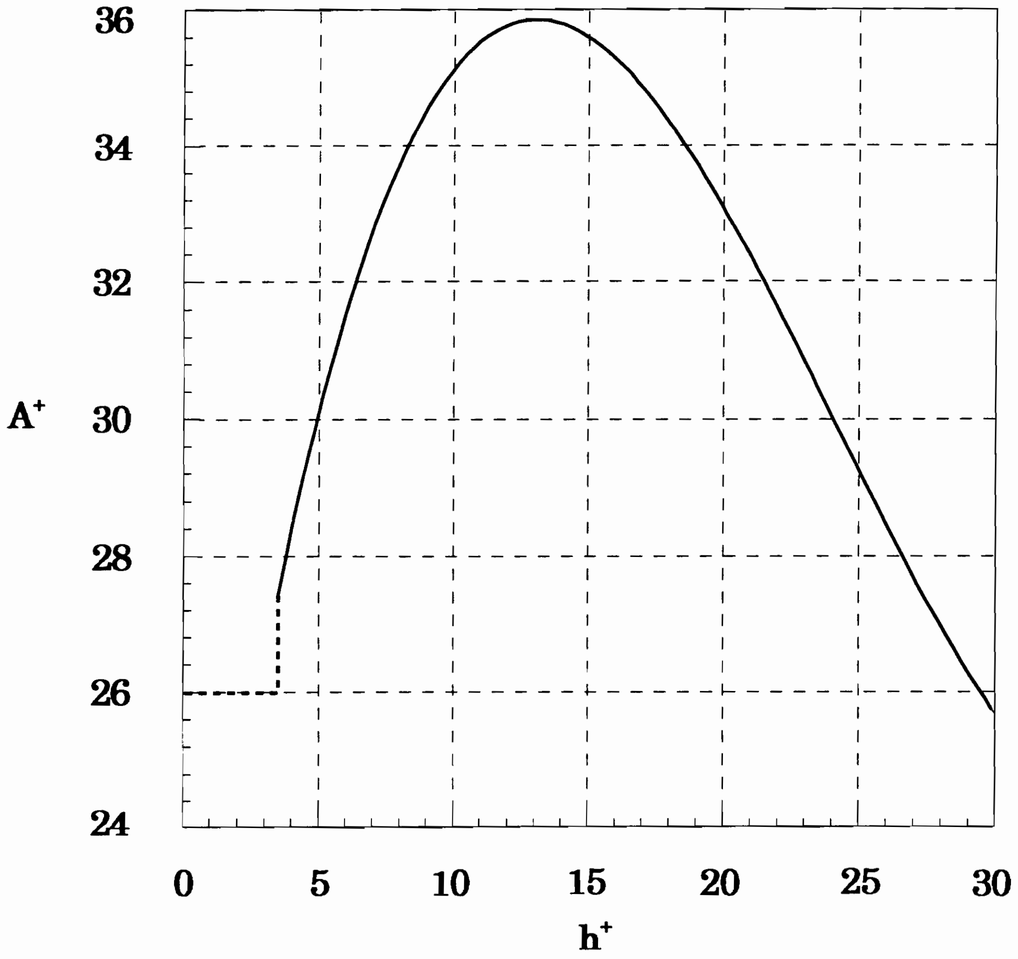

Figure 6.7 Optimum Profile of h$^+$ vs. A$^+$

6.3 Model Riblet Effect - Delayed Transition

In the numerical simulation, the transition was delayed by moving the location where the turbulent boundary layer begins on the blade surface. Figure 6.8 shows the location of transition used in the numerical simulation for both the smooth and riblet covered blades. For smooth blades the transition occurs at approximately 15% chord on the suction side and 10% on the pressure side. For the simulation of the riblet covered blades, the inception of the turbulent boundary layer was moved to the 50% chord location on the suction side. In this study, the transition process was not modelled. The boundary layer was simulated to be either laminar or turbulent.

In this chapter, a method to model riblet effects on the STF blades was described. This method involved moving the transition location on the suction surface of the blade and, also, modifying the Baldwin-Lomax turbulent model. In the following chapter, the results from the simulated riblet effects are presented.

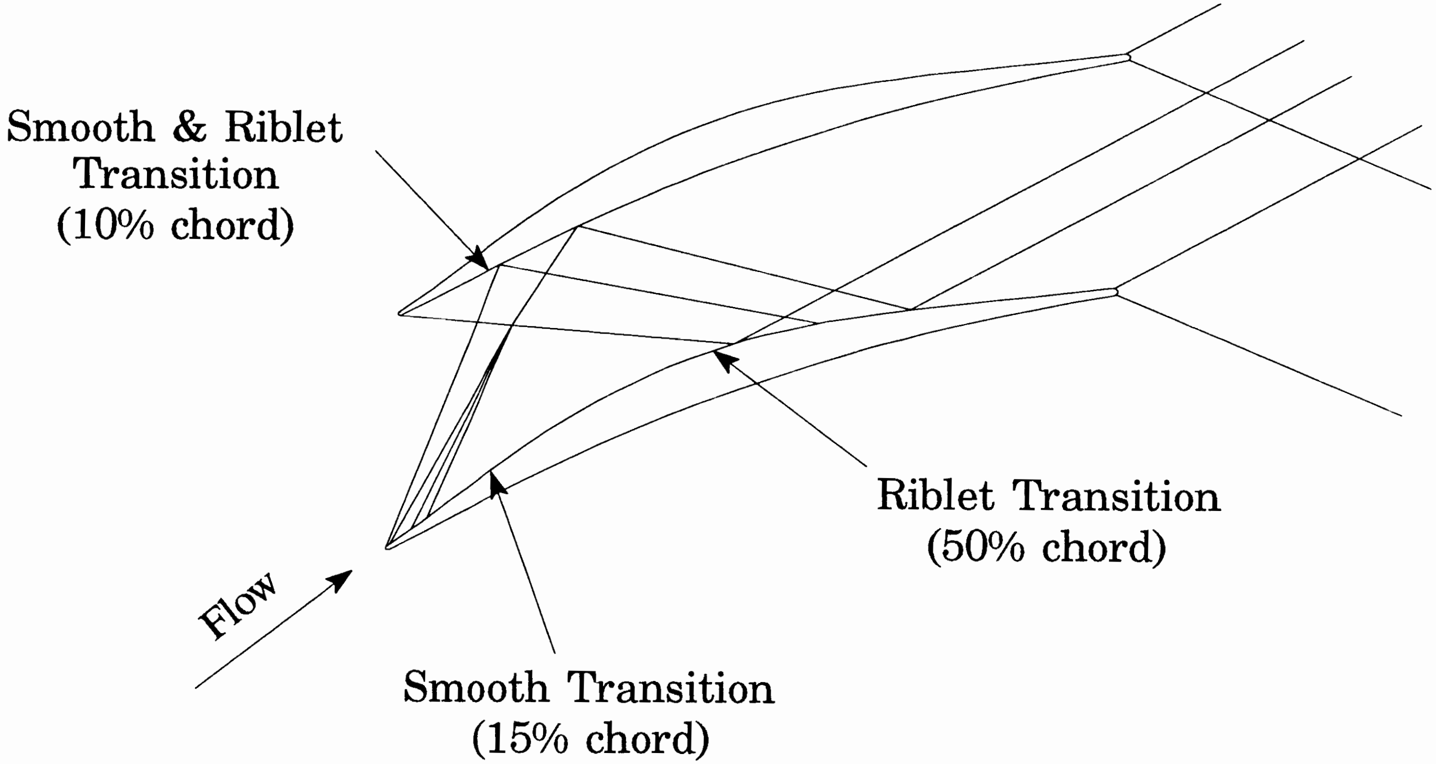

Figure 6.8 Locations for Transition in the Numerical Simulation

7.0 Numerical Results

Numerical simulations for both the smooth and riblet covered STF cascade blades were conducted. As described earlier, riblets produced two distinct effects on the STF blades. As anticipated, riblets decrease the turbulent viscous drag; but in the STF cascade, they also delayed the transition of the turbulent boundary layer on the suction side of the blade. The purpose for the STF simulation was to determine if the two riblet effects would account for the optimum decrease in loss coefficient that was observed experimentally. Also in the numerical simulation, the two riblet effects were studied separately, in order to estimate the contribution of each effect on the total reduction in viscous losses.

This chapter begins with a review of the previous efforts at VPI&SU to simulate the STF cascade flow field. These simulation efforts focused on predicting the experimental flow field of the original blade design. The purpose of this numerical study is to simulate the change in performance of the STF cascade due to riblets.

7.1 Background on STF Simulation

Previous research involving the numerical simulations of the STF cascade were conducted by Chesnakas[13] and Andrew.[15] Chesnakas found, for the design incidence angle, that the simulated flow field generally agreed with the experimental results. In the simulation, some details were not predicted; however, these discrepancies did not greatly effect the global results--as the integrated loss coefficient was well predicted. For the off-design incidence angles, larger differences exist between the measured and calculated results. This was attributed to the inadequate modeling of the strong shock-boundary layer interaction that is characteristic of the off-design conditions.

In an effort to improve the off-design simulations, Andrew substantially modified the grid and incorporated a more complex turbulent model into the CFD code. Originally an H-mesh was used by Chesnakas in the simulation of the STF blades. Andrew developed a body-fitted, periodic C-mesh for the STF simulation. The new mesh improved the clustering of cells near leading and trailing edge of the blade surface. Also, additional cells were positioned in the mid-chord region to capture the shock-boundary layer interaction. For the -5° incidence simulation, the Baldwin-Lomax model was replaced by the Johnson-King model. Previously, the Johnson-King model had demonstrated the ability to predict transonic shock-separated flows by accounting for non-equilibrium effects. To simulate the cascade flow field, Andrew modified the Johnson-King turbulent model for use in internal flows. These changes to the STF cascade simulation, however, were found not to improve the prediction for the off-design condition.

Due to strong shock-boundary layer interaction at off-design conditions, the numerical simulation for the riblet effects on the STF blades was performed only for design incidence. From the riblet numerical investigation, the results for four different simulations are presented. In the first simulation, the flow field was calculated for the smooth blades. This simulation served as the baseline test and was compared to the simulated riblet results. In the next two simulations, the two riblet effects, turbulent viscous reduction and delayed transition, were calculated separately. Finally, in the last simulation, the combination of the two riblet effects was computed to determine the total decrease in viscous losses.

7.2 STF Simulation Results

The numerical simulation of the STF flow field for the smooth surface blades is represented by the static density contours shown in Figure 7.1. From the shadowgraph in Chapter 5, the boundary layer is known to become turbulent at approximately 10% chord on the pressure side and 15% on the suction side. For the CFD simulation, the boundary layer was designated to be turbulent beginning at these locations on the blade surfaces. Comparison of the static density contours with the schematic of shock structure, previously presented in Figure 4.1, shows good agreement. The bow shocks and their reflection on the blade surfaces are well reproduced in the numerical

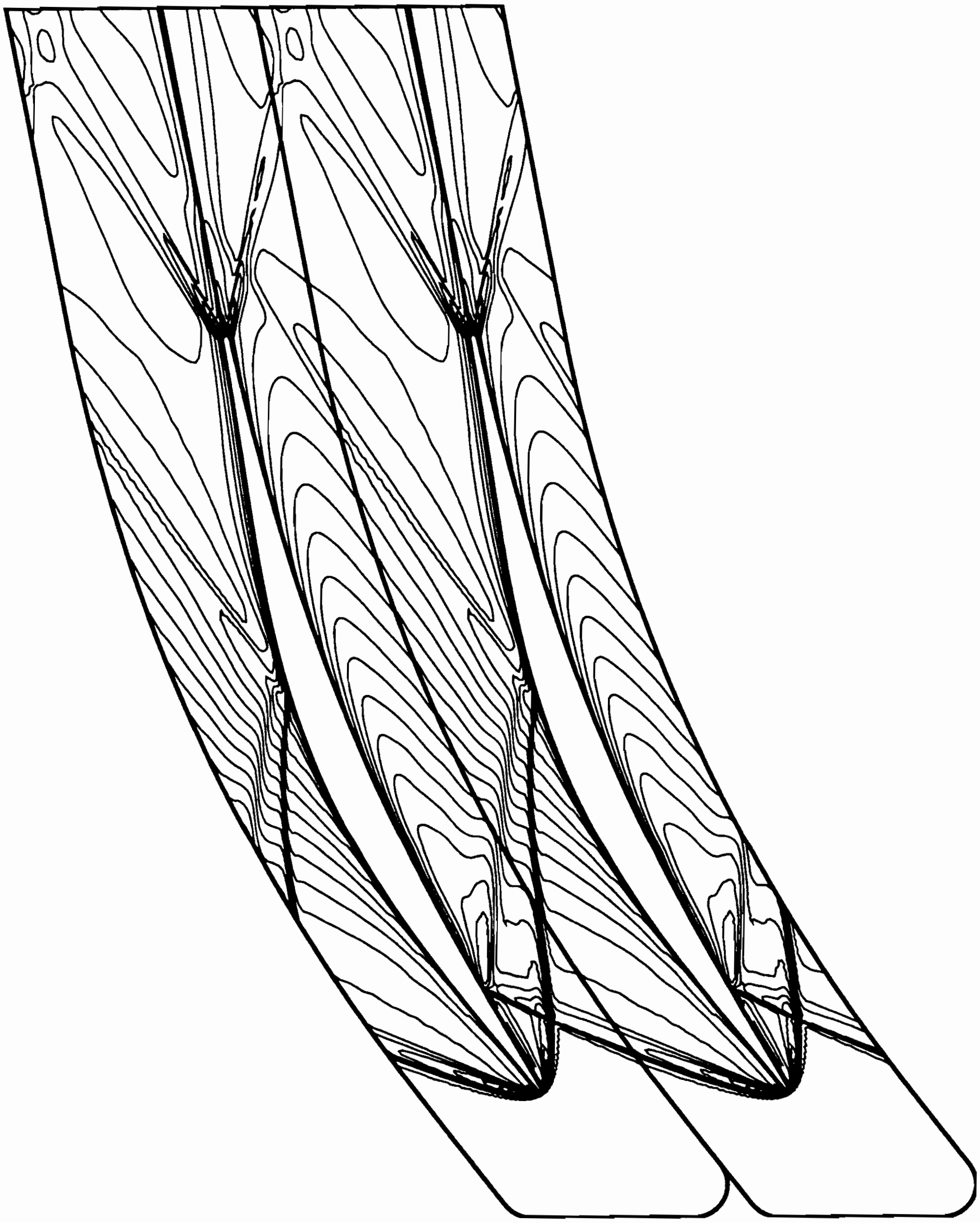

Figure 7.1 Static Density Contours, Design Incidence

simulation. The only discrepancy, seen in the contours, is the simulation's failure to reproduce the pre-compression shock and its reflection on the blade pressure surface.[3]

The calculated skin friction for the smooth blade is presented in Figure 7.2. The location of transition is indicated by the sharp increase in the skin friction values at approximately 10% chord on the pressure and 15% chord on the suction surface of the blade. In the mid-chord region on the suction surface, the skin friction plot indicates that the boundary layer separates and reattaches from impingement of the leading edge bow shock. The region of separated flow on the STF blades was confirmed by surface oil flow visualization.[15] Following the separation region on the suction surface, another sharp drop in the coefficient of friction exist. This is the result of the impingement of the bow shock reflecting from the above pressure surface and striking the suction surface at approximately 57% chord.

To simulate the local riblet effect, an estimate of the optimum h^+ profile for the blade surface is calculated from the smooth surface results. A corresponding A^+ profile on the blade surface is generated from the h^+ profile in the process describe in Section 6.2.1. Both the h^+ and A^+ profiles are presented in Figure 7.3. In this figure, values for h^+ and A^+ are shown for the whole blade surface, including the laminar boundary layer region. As will be

---

[3] Chesnakas and Andrew were also unable to produce the pre-compression shock in their simulations.

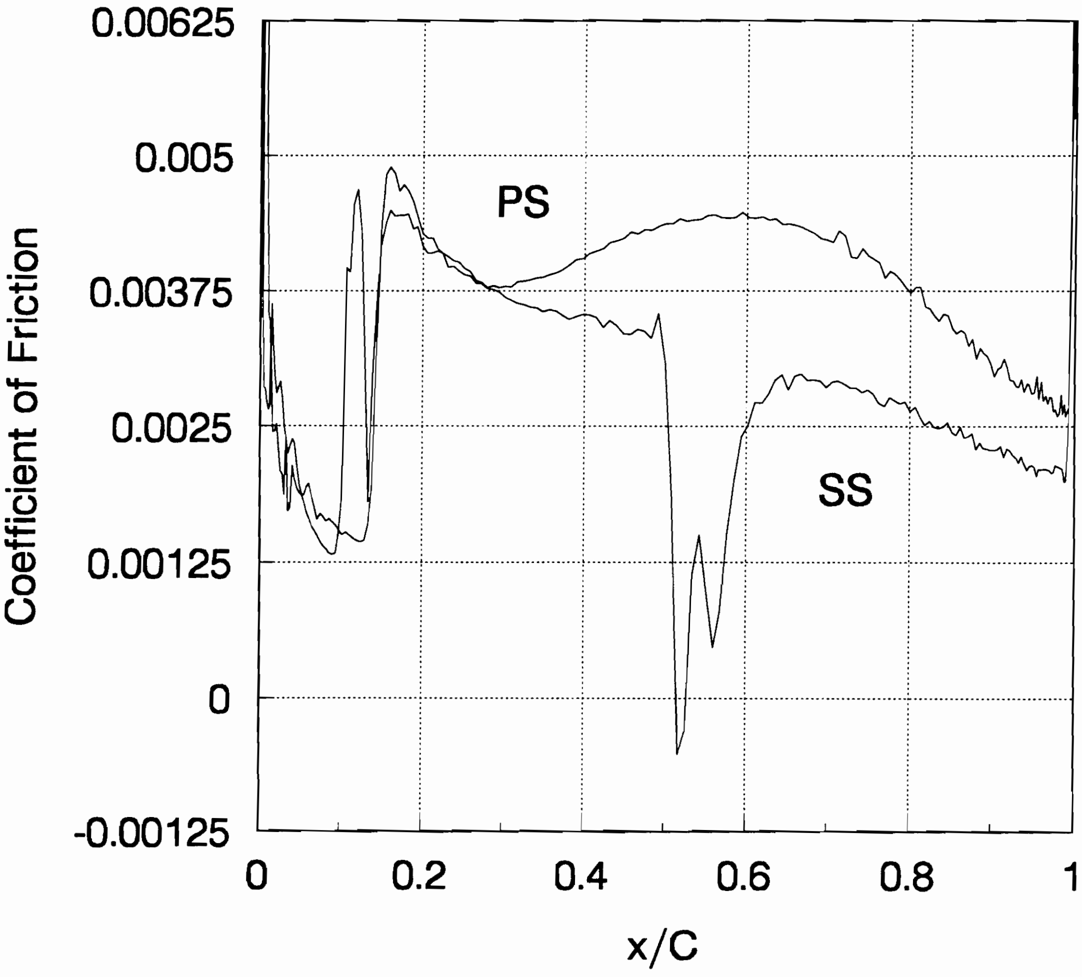

Figure 7.2 Skin Friction Coefficient, Smooth Surface

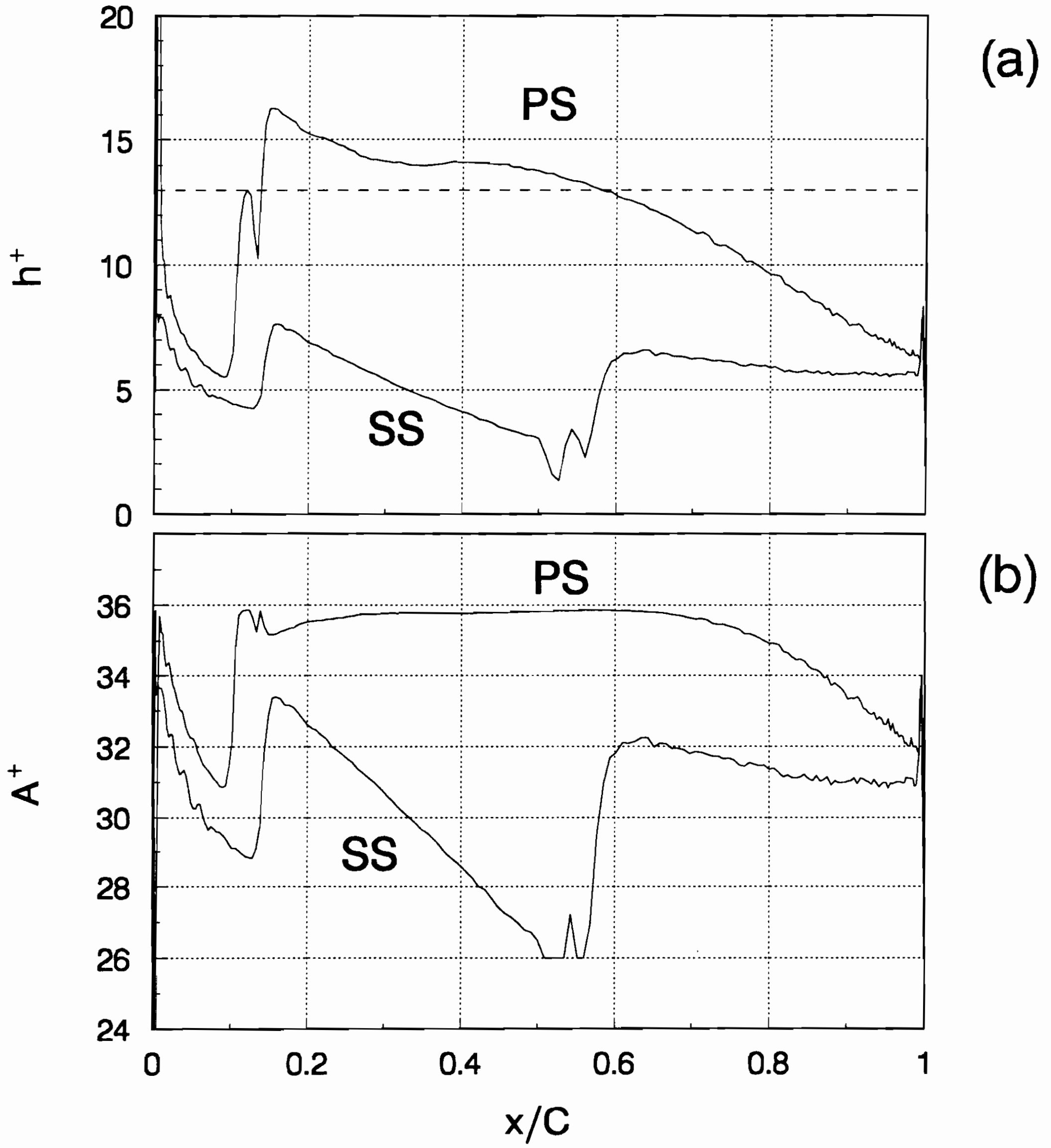

Figure 7.3 Local Riblet Effect Profiles, h^+ and A^+

shown later, these laminar values of A^+ are not used when computing the riblet effect on the turbulent boundary layer.

In figure 7.3(a), the h^+ values indicate that the riblet effect will not be constant over the blade surface. Most of the riblet benefit--from reducing the turbulent viscous losses--will come from the pressure side of the blade. The h^+ values on the pressure side are near the optimum riblet height value, represented by the dashed line.

As previously discussed in Chapter 6, higher A^+ values represents a greater decrease in viscous losses. In Figure 7.3(b), a maximum riblet benefit is shown to occur after the impingement of the leading edge bow shock on the pressure surface, x/C=0.15, and extend past the mid-chord location of the blade, x/C=0.7. In this region, the local riblet effect will produce a near constant 10% decrease in viscous losses. This region is characterized by a favorable pressure gradient and an accelerated flow. After 70% chord, the amount of benefit from the riblets slowly decreases, indicated by lower A^+ values, at blade locations further downstream on the pressure surface.

On the suction side of the blade, a smaller local riblet benefit is seen. After the shock impingement at the mid-chord region, the riblet effect is nearly constant with an A^+ value between 31 and 32.

For the first riblet simulation, the flow field in the STF cascade was computed for a riblet effect that only produces a decrease in turbulent viscous losses. This simulation does not include the delayed transition effect. For the simulation, the constant A^+ value of 26 was replaced with the varied A^+ value profile shown in Figure 7.3(b).

The varying riblet effect in the simulation of the STF cascade is observed by comparing skin friction values. A comparison of the calculated skin friction between the riblet and smooth surface is presented in Figure 7.4. Near the leading edge, there is no difference in the coefficient of friction as the boundary layer is laminar. As expected, the riblet effect produced lower values of skin friction. The greatest decrease in skin friction is seen on the pressure surface side of the blade. In the region following the shock impingement at x/C=0.15 to x/C=0.7, the riblet effect produced a localized decrease coefficient of friction of approximately 10%. On the suction side, the modelled riblet effect resulted in a small change in the coefficient of friction.

The overall effect from the localized reduction in viscous losses on the blade surfaces is determined by the change in mass-averaged loss coefficient. This riblet effect, modelling only for a decrease in the turbulent viscous losses, produced a 2.5% change in loss coefficient. This change in loss coefficient is much smaller than the experimental optimum riblet results. However, the reduction in turbulent viscous losses is only one part of the riblet effect on the STF cascade blades.

In the next riblet simulation, the effect of only a delayed transition was calculated. The transition of the boundary layer was relocated further downstream, near the shock impingement location on the suction surface, at

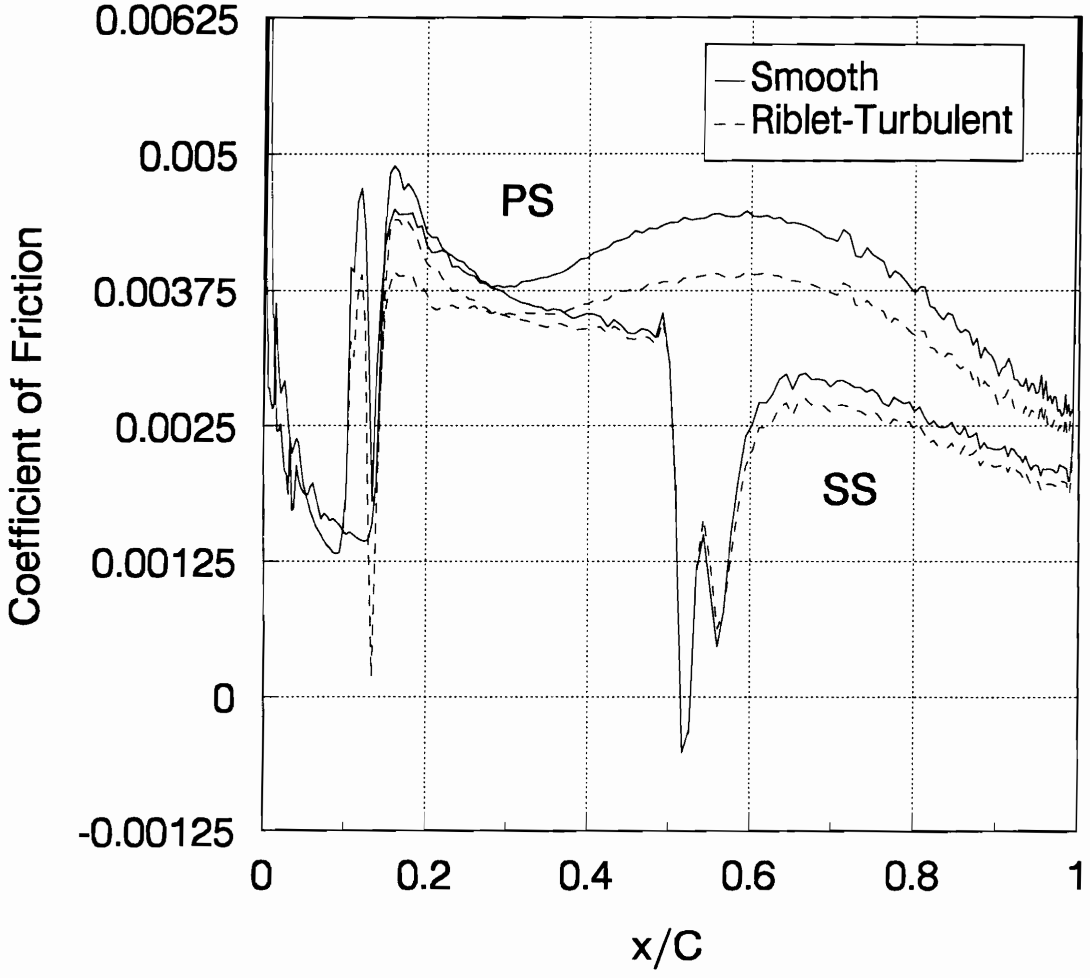

Figure 7.4 Comparison of Friction Coefficient, Turbulent Reduction

50% chord. On the pressure surface, as indicated by the shadowgraph shown in Chapter 5, the shock impingement on the blade surface at approximately 10% chord is responsible for the formation of the turbulent boundary layer. Therefore, the transition location did not move, due to the riblets, on the pressure surface side of the blade.

The flow field for the STF cascade with the riblet effect of only delaying transition was computed. The localized result on the blade surface from this riblet effect is seen in the comparison of the coefficient of friction profiles in Figure 7.5. The delayed transition effect produces a markedly lower coefficient of friction on the first half of the suction surface of the blade. The average difference in the coefficient of friction between the turbulent and laminar boundary layer in this region is approximately 60%. After 50% chord, both profiles represent a turbulent boundary layer. As a result of delayed transition, the turbulent boundary for the riblet blades is less developed than the smooth blades. This results in an increase in the coefficient of friction for the second half of blades suction surface. The overall effect of delaying transition, until the shock impingement location on the suction surface, is a 4% decrease in mass-averaged loss coefficient.

In the final numerical simulation, the flow field for the combined riblet effects was computed. In the numerical study, the combined riblet effect simulates for a delayed transition and a decrease in turbulent viscous losses. The comparison of the calculated skin friction between the combined riblet

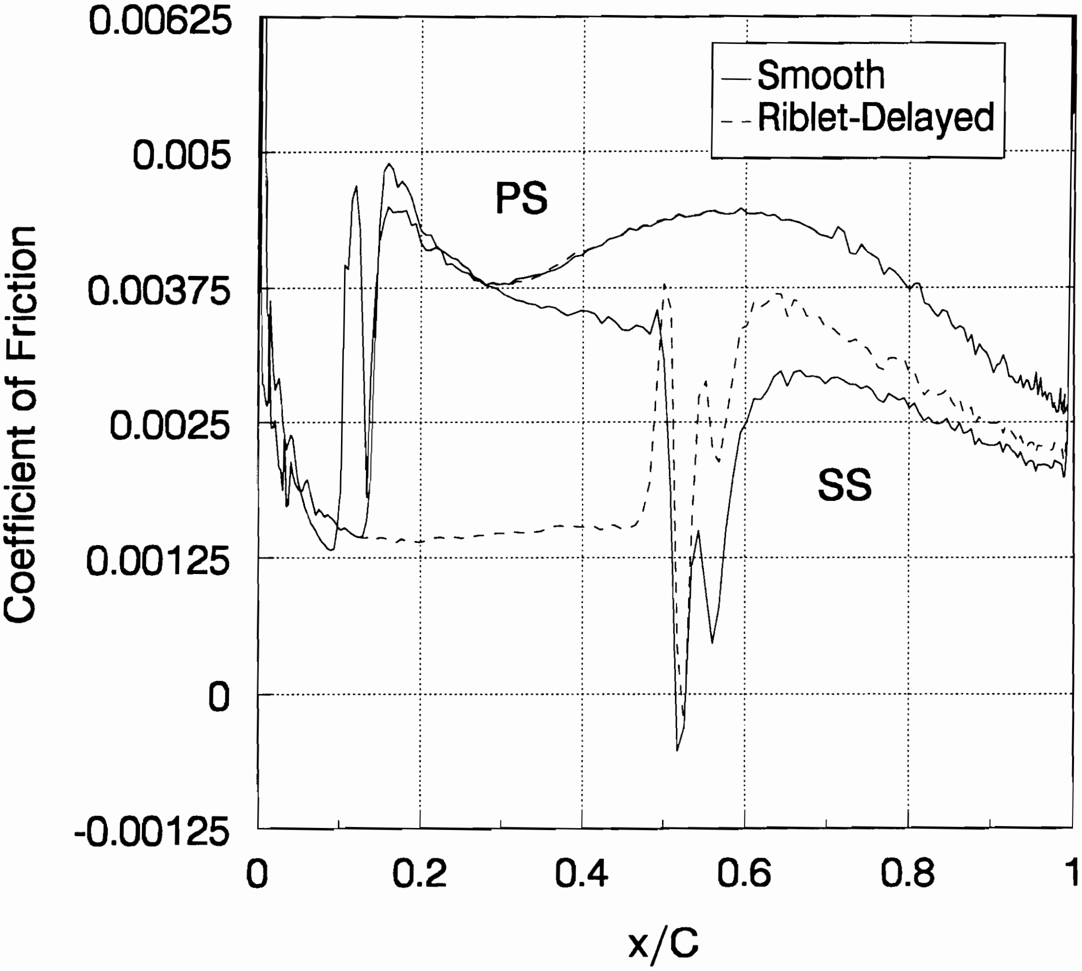

Figure 7.5 Comparison of Friction Coefficient, Delayed Transition

effect and the smooth surface is presented in Figure 7.6. On the pressure side, a near optimum decrease in the turbulent viscous losses is seen. For the suction surface, the delayed transition is responsible for most of the decrease in viscous losses.

The change in loss coefficient for a combined riblet effect was 6%. This numerical result is comparable to the measured experimental result and supports the conclusion based on the leading edge shadowgraph that transition was delayed on the STF blades.

To investigate the simulated results in more detail, the total pressure profiles for the smooth and combined riblet effect were compared. Presented in Figure 7.7 are the total pressure profiles for the riblet and smooth case, along with a plot showing the difference between the two profiles. For Figure 7.7(a), the riblet profile shows higher total pressure values through out the survey. For the total pressure profile downstream of the cascade, the riblet effect produces a wake that is thinner and less deep.

In Figure 7.7(b), the difference between the profiles, ΔP_t, illustrates that the riblet benefit occurs on both sides of the blade's surface but not by the same for amount. The suction side, where transition was delayed, shows a peak difference between the profiles occurs in mid portion of the suction side wake. For the pressure side wake, the riblet effect produces a smaller difference between the two profiles. At the wake minimum point, a slightly smaller change in total pressure profiles exist compared to changes on either

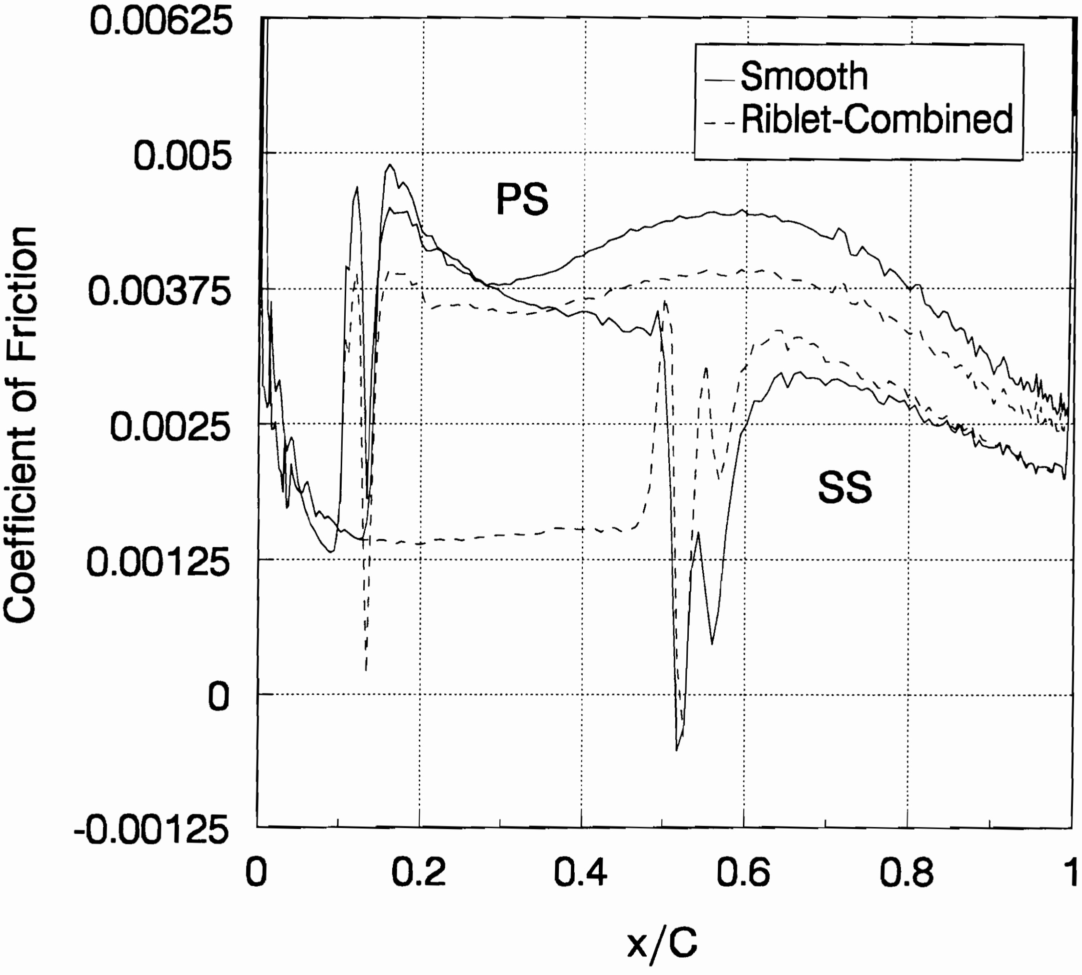

Figure 7.6 Comparison of Friction Coefficient, Combined Effect

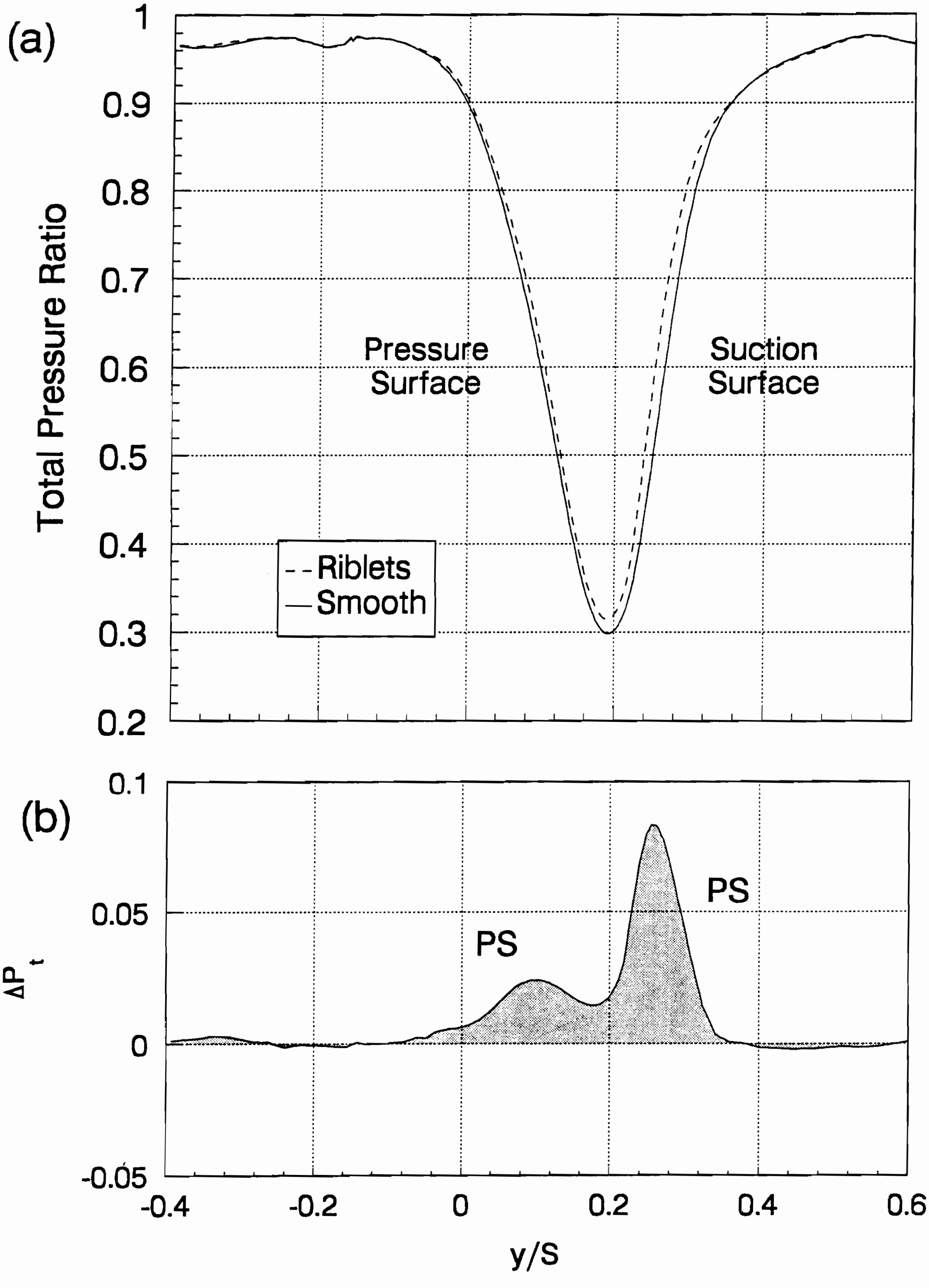

Figure 7.7 Total Pressure Profile Comparison, Numerical

the suction or pressure side wake.

As seen in the numerical investigation, a significant local decrease in viscous losses on the blades surface produces a much smaller change in the mass-averaged loss coefficient. As mentioned earlier, shock losses in the cascade account for a good portion of the total losses. Therefore, this suggests that only a combined riblet effect--delayed transition and decrease in turbulent viscous losses--is able to produce the significant decrease in losses that were measured experimentally.

8.0 Conclusions

The focus of this research was to improve the performance of the supersonic through flow cascade blades by reducing the viscous losses. This was accomplished by applying riblets to the surface of the blades. The effect of the riblets on the performance of the cascade blades were investigated for different riblet heights, cascade incidence angles, and Reynolds numbers. For this riblet study, measurements were made downstream of cascade blades. The total pressure profile and integrated loss coefficient from the riblet covered blades were compared to smooth covered blades results to determine the riblet effect.

Results from previous studies have demonstrated that riblets will reduce the viscous losses in a turbulent boundary layer. Most of these studies were conducted on simple wall geometries with the boundary layer being tripped upstream of the riblets. A general trend for the riblet performance was produced by relating an h^+ parameter to the change in viscous drag. The h^+ parameter is a function of the riblet height and the local flow parameters on the blade surface.

In the STF cascade, the flow field provided a unique environment for a riblet study. The STF cascade is characterized by shock-boundary layer interactions and an overall favorable pressure gradient in the blade passage.

Additionally, the boundary layer is initially laminar on the pressure and suction side of the smooth blade surface.

At the design incidence angle, three different height riblets were tested. All three sizes produced a decrease in the loss coefficient when compared to the smooth covered blades. The optimum riblet height lowered the mass-averaged loss coefficient by 8.5%. Comparison of the total pressure profiles revealed that the riblet covered blades produces a thinner wake downstream of the cascade. A riblet benefit was seen on both the suction and pressure side of the wake.

The effect of riblet height on the performance of the STF blades produced a result similar to the trend for the h^+ parameter from previous riblet studies. The importance in matching an appropriate riblet height with the flow conditions was seen at the off-design incidence angles and different cascade Reynolds number, where the optimum riblet height produced a smaller change in the cascade's mass-averaged loss coefficient.

A shadowgraph study was carried out to determine the riblet effect on the location of the turbulent transition on the blade surfaces. At design incidence, the optimum riblet height delayed the transition location on the suction side of the blade. For the riblet covered blades, the decrease in viscous losses was attributed to two distinct riblet effects. Similar to other riblet studies, the riblets decreased the viscous losses in the turbulent boundary layer. The unexpected riblet effect was the change in the transition location on the suction side of the STF blades. The combination of the two riblet effects are credited for producing the optimum riblet benefit found at design incidence.

In addition to the experimental study, a numerical investigation of the riblet effect on the STF cascade was conducted. A simple method was developed to model both riblet effects on the blades. Conclusions from numerical study indicate that 2/3 of the total decrease in losses are the result of delaying the transition location. The final 1/3 decrease in loss coefficient comes from the decrease in turbulent viscous losses.

Appendix A

Uncertainty Analysis

This section serves to quantify the errors associated with the riblet experiment. Since the purpose of riblet study was to measure small differences between the riblets and equivalent smooth layer, the uncertainty analysis is based on the relative errors associated with the change in the calculated loss coefficient. As a result, a separate study was conducted to determine the change in the loss coefficient for consecutive runs with similar testing conditions.

The original bare blades were tested at the design incidence angle with a Reynolds number of 4.8 million based on chord. A total number of 17 runs were conducted to ensure a sufficient sample size for the uncertainty analysis. Between each tunnel run, the blades were removed and re-inserted into the test section in order to simulate the testing procedure used in the riblet experiment.

Statistical analysis was used to determine the relative error in the calculated loss coefficient between tunnel runs. A histogram of this result is presented in Figure A.1. A 99% confidence interval was used to determine the uncertainty in the riblet study.

In the riblet study, the uncertainty in the change in loss coefficient between the riblet and equivalent smooth covered blades was estimated to be ±2%. The procedure to determine the uncertainty is illustrated in Figure A.2. The upper and lower bounds of the 99% confidence interval for the smooth and riblet results are represented by dashed lines. An equivalent layer result, with confidence interval, is linear interpolated to the riblet height location. The estimated maximum and minimum change in loss coefficient is determined by the upper and lower values in the confidence intervals of the equivalent layer and riblet results. The uncertainty band for the riblet study was the difference between the actual change in loss coefficient and the maximum and minimum values.

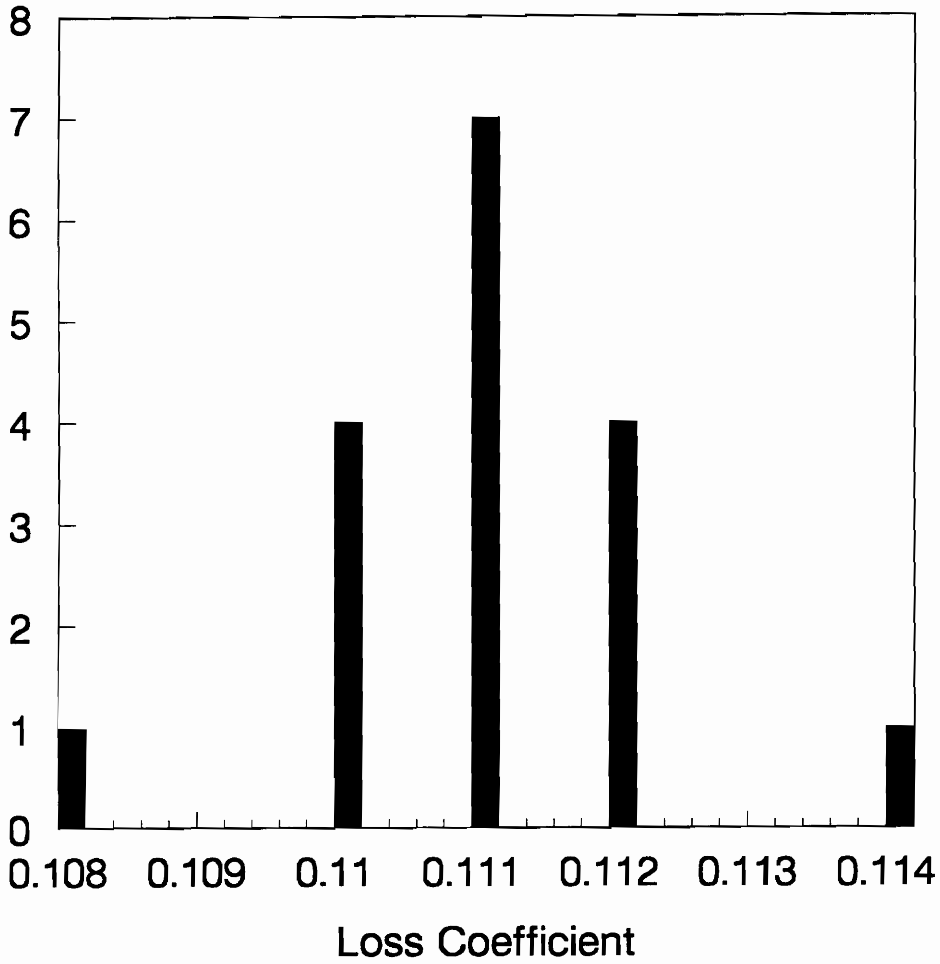

Figure A.1 Loss Coefficient Histogram

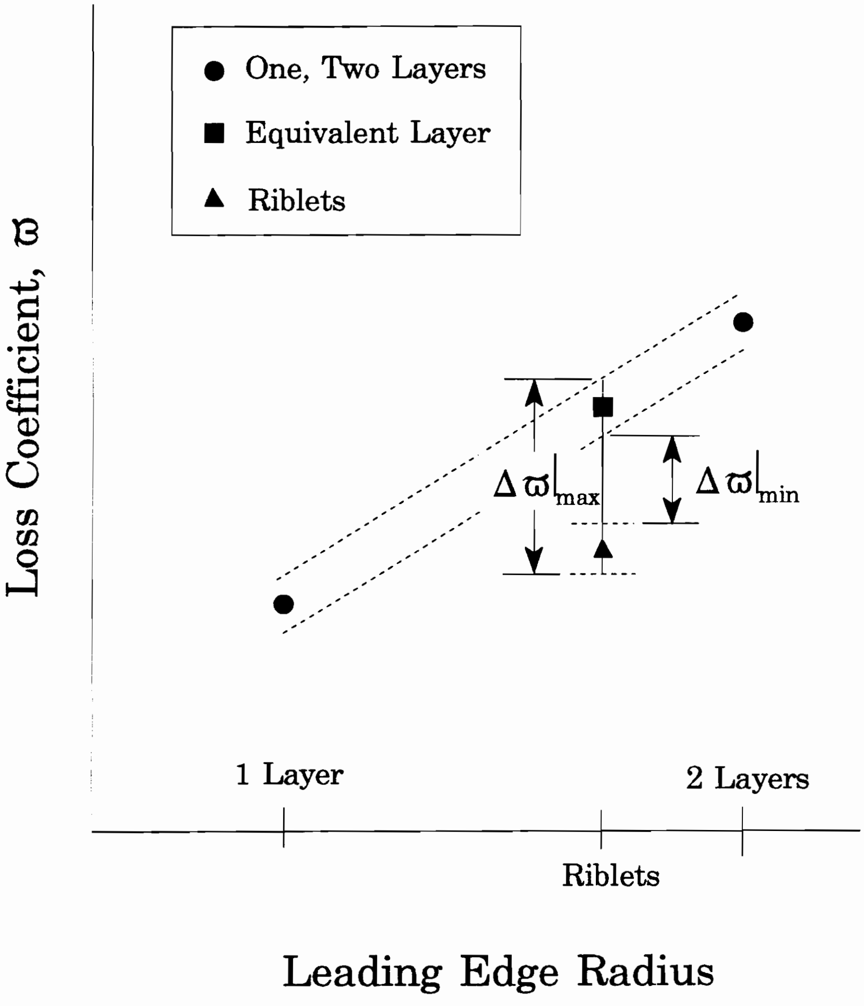

Figure A.2 Illustration of Uncertainty Analysis

Appendix B

Effect of Reynolds Number on Loss Reduction

The riblet effects on the STF blades were investigated for different cascade Reynolds numbers. The goal of this study was to determine if changes in flow conditions could produce a similar trend as in the riblet height study. This study complements the riblet height study as changes in the cascade Reynolds number produces a change in the local h^+ parameter on the blade surface. This is accomplished, however, without changing the physical riblet height. The reader will recall that the h^+ parameter is a function of the local values of friction velocity, viscosity, and density, as well as the riblet height. The study was conducted at the design incidence angle with the optimum riblet height of 0.033 mm.

For the STF cascade, the Reynolds number is determined by the total pressure upstream of the test section. In the Reynolds number study, the control valve was adjusted so that the tunnel could operate at any desired total pressure. This study was conducted at three different Reynolds numbers based on chord: 3.2, 4.8, and 5.9 million.

In the Reynolds number study, the testing procedure was identical to the riblet height study. However at each stage of the test, the procedure was repeated for the different Reynolds number conditions. For each Reynolds number, the riblets' effects were evaluated by comparing the mass-averaged loss coefficients of the riblet covered blades to blades having an equivalent layer of smooth material.

Figure B.1 shows the effect of Reynolds number on the loss reduction for riblets. Included in Figure B.1 are the results from the riblet height study. The Reynolds number and riblet height are indicated on the two different horizontal axis. The vertical axis is defined as the change in loss coefficient, from riblet height or Reynolds number, divided by the maximum riblet benefit. In Figure B.1, the Reynolds number and riblet height studies show a similar trend with an optimum riblet condition and a decrease in the benefit at the other conditions. These studies demonstrate that the optimum riblet benefit is a function of both riblet height and flow conditions. For the STF cascade design incidence, the optimum riblet benefit is produced with the 0.033 mm riblets at a Reynolds number based on chord of 4.8 million.

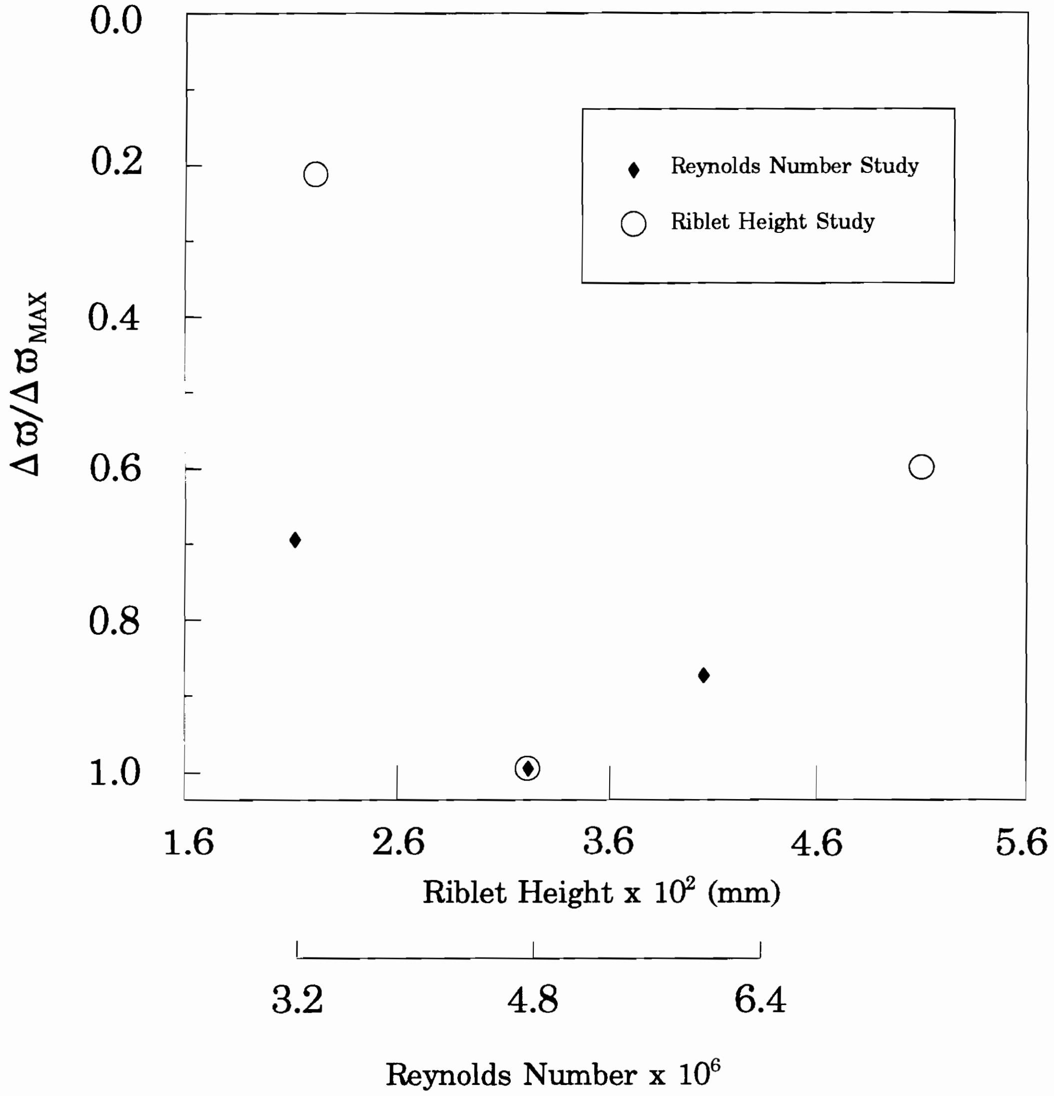

Figure B.1 Effect of Reynolds Number & Height on Loss Reduction

Appendix C

Effect of Increased Leading Edge Radius on Bow Shock Movement

In the riblet study, the application of the material increased the leading edge radius of the STF blades. One and two layers of smooth material and the riblet material were applied to the blades. In the STF cascade, any increase in the leading edge radius produces a change in the location of the bow shocks. Since the bow shocks are confined within the blade passage, they impinge and reflect on the surface of the blades as the propagate downstream. Ultimately, the reflected shocks appear downstream of the cascade at the probe traverse location. When a reflective shock wave strikes the Pitot-static probe, the wave disrupts the flow around the pitot tube.[13] As a result, the reflective shock appears as a small dip or decrease in the total pressure profile.

Since the riblet effect produces small changes in the total pressure profile. The effect from the movement of the reflective shock could be interpreted incorrectly, as a riblet effect. Shadowgraph photography was used to determine if the movement of the reflective shocks are great enough to be observed at different locations in the total pressure profiles.

Any increase in the leading edge radius will result in the movement of the leading edge bow shocks. A schematic of this effect for design incidence is illustrated in Figure C.1. Moeckel[73] had modelled the profile of a detached shock in front of a planar body to be hyperbola in shape. The shape of hyperbola produces a near normal shock in front of the body and an oblique shock--decreasing in shock strength as it moves from the body--on either side.

By applying material around the leading edge, the bow shock moves from its original position for two reason. First, the furthest point forward on the leading edge of the blade has moved upstream. As a result, the bow shock forms at a location, the thickness of the applied material, further upstream. Secondly, the frontal area of the leading edge is larger. This increases the length of the normal component of the bow shock and shifts the oblique portion of the bow shock further away from the blade.

Shadowgraph photography was used to determine the extent of the leading edge bow shock movement in the riblet study. In Figure C.2, shadowgraphs of the flow field for the STF blades, covered with two different thicknesses of smooth material, are introduced. The circular objects that appear in the shadowgraph are the supports used to secure the blades to the plexiglass side wall.

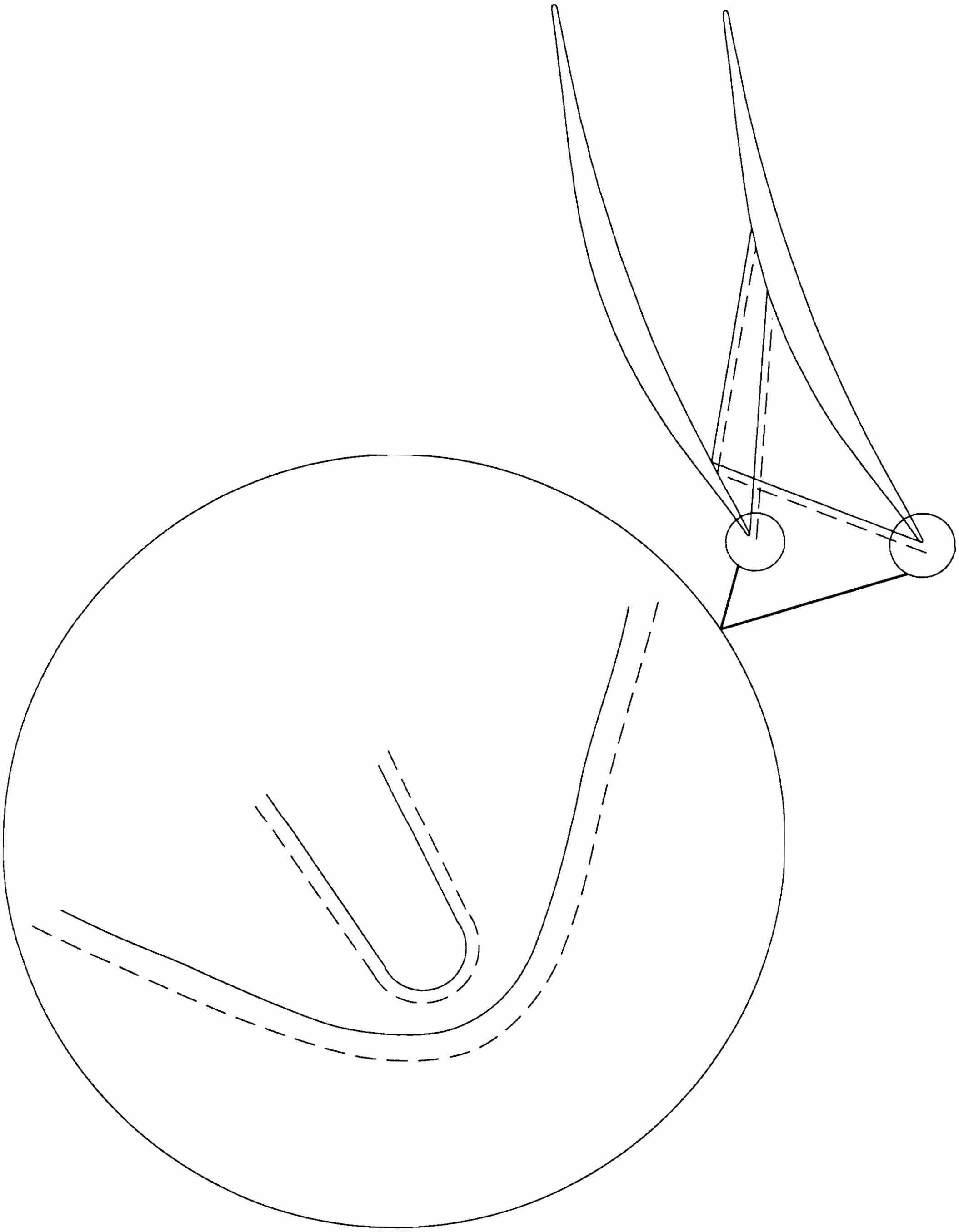

Figure C.1 Illustration of Leading Edge Shock Movement

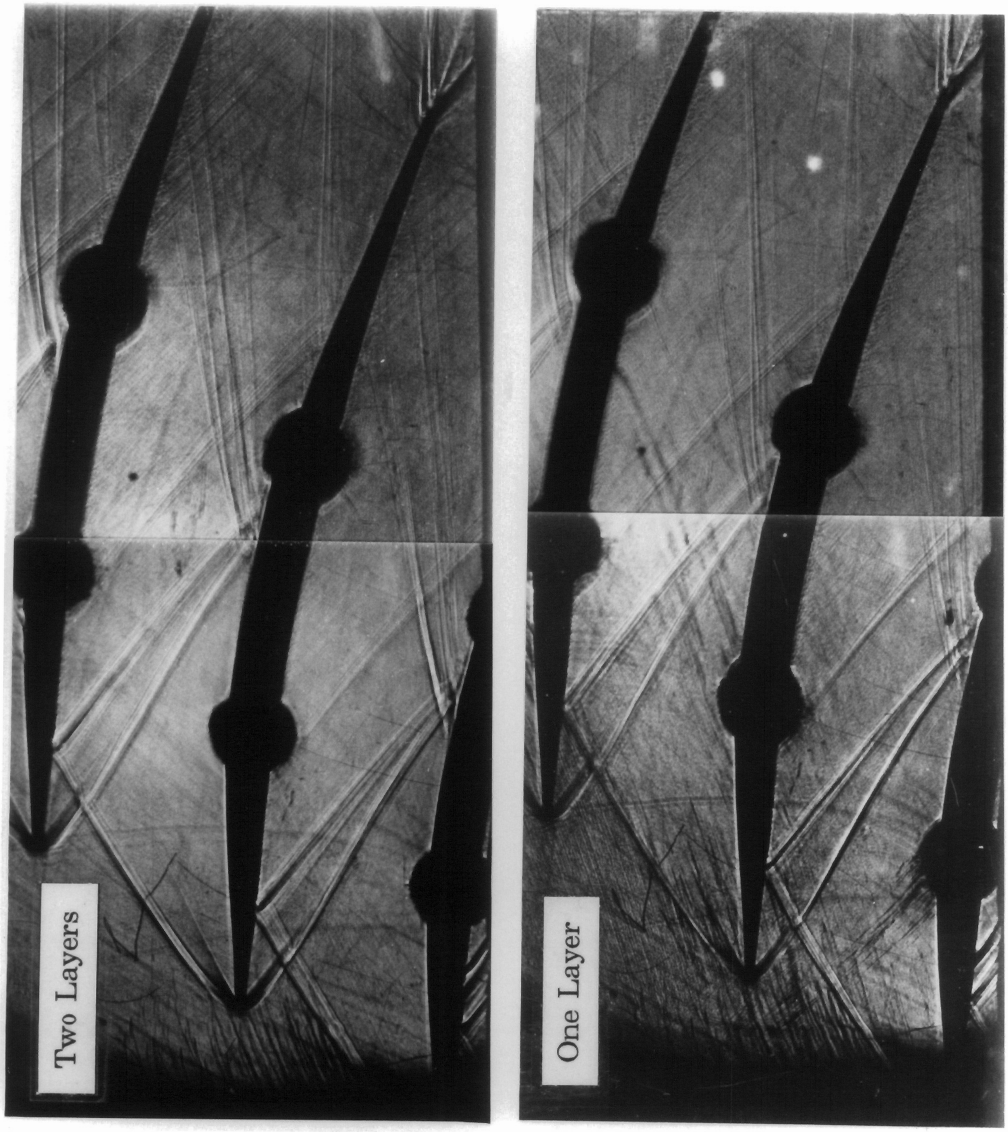

Figure C.2 Shadowgraph of Leading Edge Shock Movement

In the top shadowgraph, two layers of smooth material were applied to the blades as described in Section 3.6. The bottom photograph shows the flow field for the blades covered with a single layer of smooth material. For the shadowgraph photos, the blades are positioned at the design incidence angle and tested at Reynolds number based on chord of 4.8 million.

Comparison of the two shadowgraphs reveals the extent of the bow shock movement from an increased leading edge radius. The movement of the shock location is determined by examining the impingement points on the blade surface. For the two layer material, the impingement of the bow shock near the leading edge of the pressure surface has clearly moved upstream relative the one layer shadowgraph. The leading edge shock impinges the two layer covered blade at approximately 15% chord. The impingement of the leading edge shock appears to strike the single layer covered blade at 17% chord.

The movement of the leading edge shock is also seen in the mid-chord region of the suction side. For the two layer covered blades, the leading edge bow shock impinges the blades surface at 50% chord. The impingement location is 52% chord for the single layer covered blades. From the comparison of the shadowgraphs, the difference in the shock locations between one and two layers of smooth material on the blades will appear in the total pressure profiles.

A clear example of the movement of the reflective shocks in the total pressure profiles is presented in Figure C.3. One layer, two layers, and the interpolated equivalent thickness results are presented for the -5° incidence case. The movement of the reflective shock due to increase leading edge radius is seen on the suction surface side of the wake. At the location y/S=0.44, the reflective shock produces a dip in the two layer, total pressure profile. For the one layer, the reflective shock appears in the total pressure profile at y/S=0.56.

Since the equivalent layer total pressure profile is interpolated from the one and two layer results, the reflective shock does not appear at the appropriate location in the equivalent thickness profile. Instead, the interpolation produces two smaller dips in the equivalent total pressure profile. As a result, the comparison between the total pressure profiles of the riblet and equivalent smooth layers show differences that are not due to riblet effects. This does not, however, change the global result as shock movement effect should cancel out in the integration of the loss coefficient.

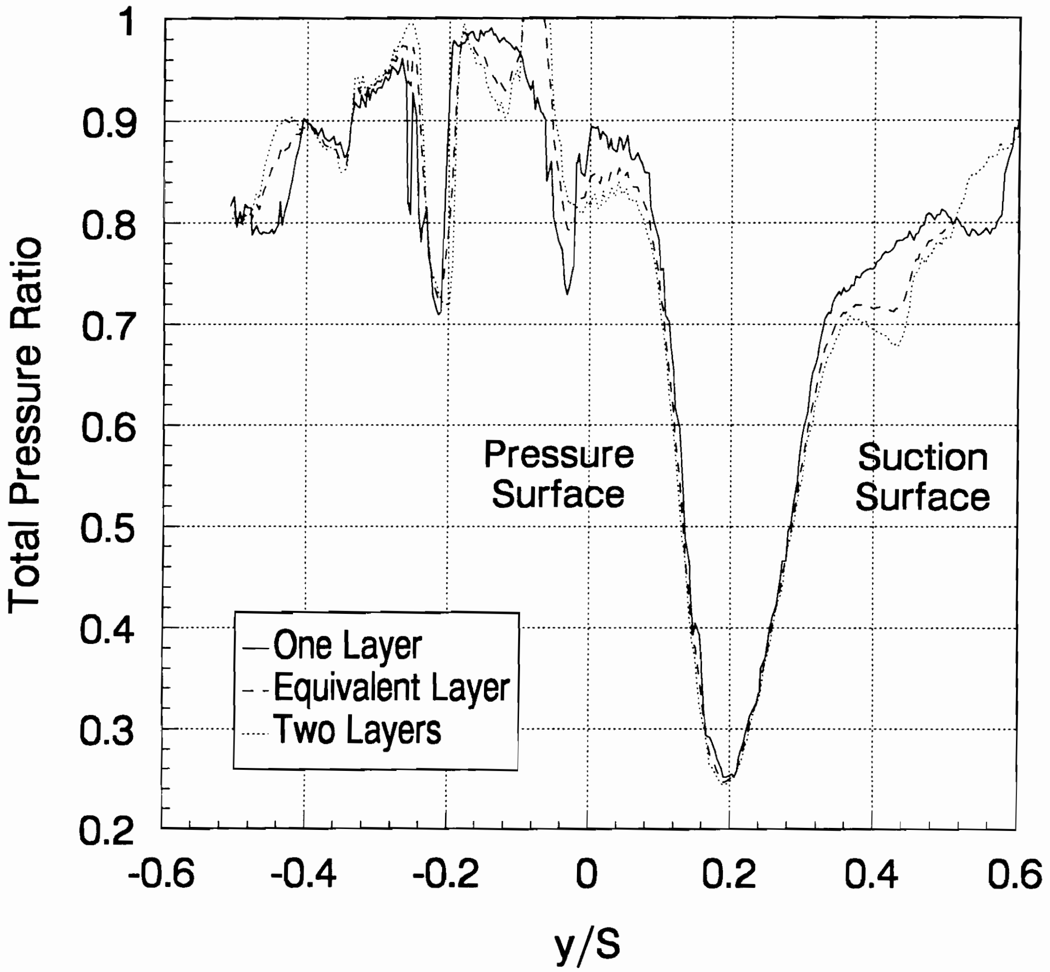

Figure C.3 Leading Edge Shock Movement Effect on Total Pressure

Appendix D

Riblet Height study

This section serves to document the results for the non-optimum riblet heights of 0.023 mm and 0.051 mm tested at design incidence. Recall from the riblet height study, the height of 0.023 mm and 0.051 mm produced a decrease in mass-averaged loss coefficient of 1.8% and 5.1% respectively. The total pressure profiles of the riblet covered and the equivalent smooth covered blades are displayed in Figure D.1 for the 0.023 mm riblets and in Figure D.2 for 0.051 mm riblets.

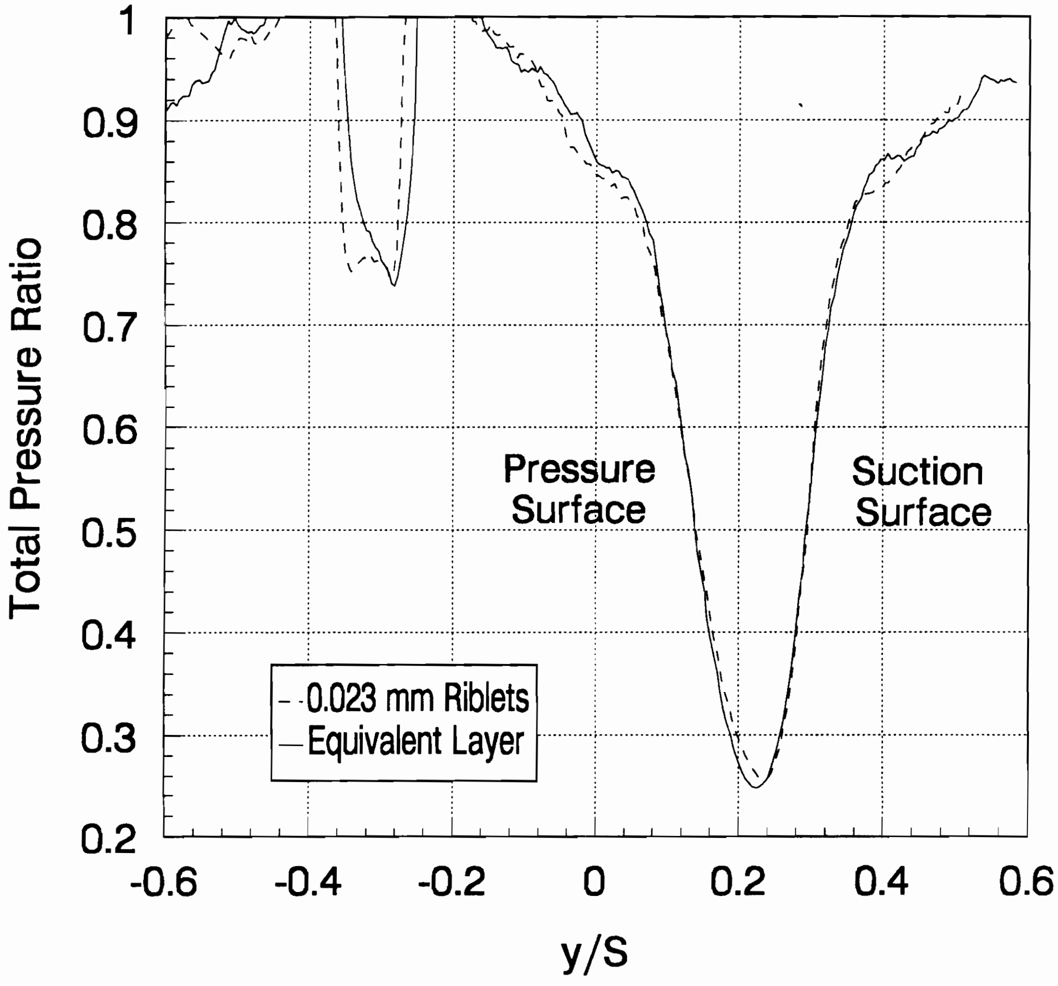

Figure D.1 Total Pressure Profile Comparison, 0.023 mm Riblets

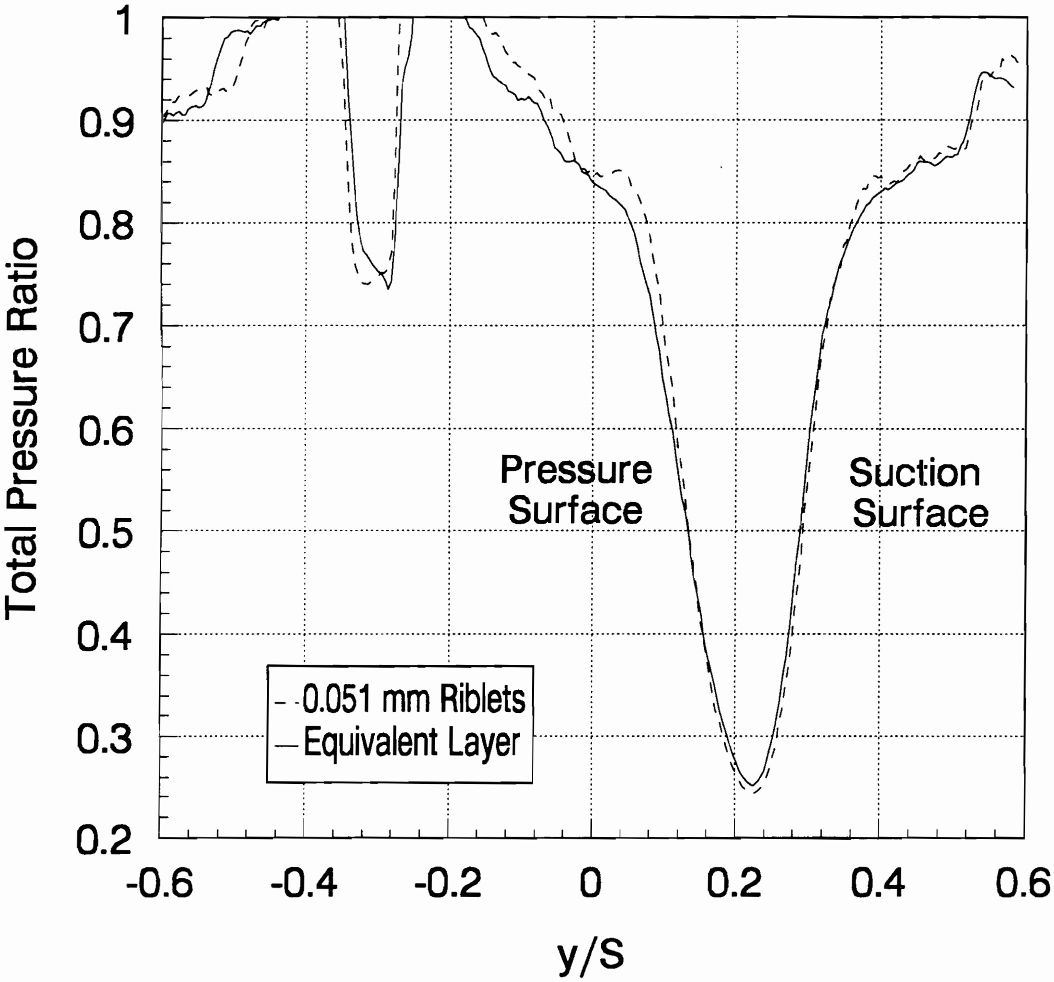

Figure D.2 Total Pressure Profile Comparison, 0.051 mm Riblets

References

1. Ferri, A., "Problems Related to Matching Turbojet Engine Requirements to Inlet Performance as Function of Flight Mach Number and Angle of Attack," Proceedings of a Conference on Air Intake Problems in Supersonic Propulsion, J. Fabri, Ed., AGARDograph No. 27, AGARD, France, 1956.

2. Trucco, T.S., "Study of Variable Cycle Engines Equipped with Supersonic Fans, Final Report, NASA-CR-134777, 1975.

3. Franciscus, L.C., "Supersonic Through-Flow Fan Engines for Supersonic Cruise Aircraft," NASA-TM-78889, 1978.

4. Tavares, T.S., "A Supersonic Fan Equipped Variable Cycle Engine for a Mach 2.7 Supersonic Transport," NASA-CR-177141, 1985.

5. Kepler, C., and Champagne, G., "Performance Potential of (an) Air Turbo-Ramjet Employing Supersonic Through-Flow Fan," AIAA Paper No. 89-0010.

6. Franciscus, L.C., "The Supersonic Through-Flow Turbofan for High Mach Propulsion," NASA-TM-100114, 1987.

7. Saunders, N.T., and Glassman, A.J., "Turbomachinery technology for High-Speed Civil Flights," NASA TM 102092.

8. Boxer, E., "The Variable-Pitch Supersonic Inflow Compressor and Its Application in a Hypersonic Engine," Proceedings from a Conference on Hypersonic Aircraft Technology, NASA SP-148, 1967, pp. 401-416.

9. Savage, M., Boxer, E., and Erwin, J.R., "Resume of Compressor Research at the NACA Langley Laboratory, "*Journal of Engineering for Power*, Vol. 83, No. 3, July 1961, pp. 269-285.

10. Breugelmans, F.A.E., "The Supersonic Axial Inlet Component in a Compressor," ASME Paper No. 75-GT-26, March 1975.

11. Wood, J.R., Schmidt, J.F., Steinke, R.J., Chima, R.V., and Kunik, W.G., "Application of Advanced Computational Codes in the Design of an Experiment for a Supersonic Throughflow Fan Rotor," ASME Paper No. 87-GT-160.

12. Schmidt, J.F., Moore, R.D., Wood, J.R., and Steinke, R.J., "Supersonic Through-Flow Fan Design," AIAA Paper No. 87-1746.

13. Chesnakas, C.J., "Experimental Studies in a Supersonic Through-Flow Fan," Doctoral Dissertation, Department of Mechanical Engineering, Virginia Polytechnic Institute and State University, Blacksburg, VA, May 1991.

14. Bowersox, R.D.W., "Meanflow and Turbulence Measurements in the Wake of a Supersonic Through-Flow Fan," Master of Science Thesis, Department of Aerospace and Ocean Engineering, Virginia Polytechnic Institute and State University, Blacksburg, VA, January 1990.

15. Andrew, P.L., "Experimental and Numerical Investigation of the Off-Design Flow Physics," Doctoral Dissertation, Department of Mechanical Engineering, Virginia Polytechnic Institute and State University, Blacksburg, VA, August 1992.

16. Walsh, M.J., "Riblets,": in Viscous Drag Reduction in Boundary Layers(eds. by D.M. Bushnell and J.N. Hefner) Progress in Astronautics and Aeronautics, Vol. 123, 1990, pp. 203-261.

17. Coustols, E. and Savill, A.M., "Turbulent Skin-Friction Drag Reduction by Active and Passive Means: Part I", AGARD-R-786, AGARD, March 1992, pp. 8:1-53.

18. Bandyopadhyay, P.R., "Review-Mean flow in Turbulent Boundary Layers Disturbed to Alter Skin Friction," *Journal of Fluids Engineering*, Vol. 108, June 1986, pp. 127-140.

19. Savill, A.M., "Drag Reduction by Passive Devices-a Review of Some Recent Developments," in Structure of Turbulence and Drag Reduction, Editor Gyr, A., Springer-Verlag, 1990.

20. Walsh, M.J., "Turbulent Boundary Layer Drag Reduction Using Riblets," AIAA Paper No. 82-0169.

21 Walsh, M.J. and Anders,Jr., J.B., "Riblet/LEBU Research at NASA Langley," Applied Scientific Research, Vol. 46, No. 3, 1989, pp.255-262.

22. Walsh, M.J. and Lindemann, A.M., "Optimization and Application of Riblets for Turbulent Drag Reduction," AIAA Paper No. 84-0347.

23. Walsh, M.J. and Weinstein, L.M., "Drag and Heat Transfer on Surfaces with Small Longitudinal Fins," AIAA Paper No. 78-1161.

24. Enyutin, G.V., Yu, A., Samoilova, N.V., Fadeev, I.V., and Shumilkina, E.A., "Experimental Investigation of the Effect of Longitudinal Riblets on the Friction of a Flat Plate," Fluid Dynamics, Vol. 23, No. 2, March-April, 1987, pp. 284-289.

25. Rohr, J.J., Andersen, G.W., Reidy, L.W., and Hendricks, E.W., "A Comparison of the Drag-Reducing Benefits of Riblets in Internal and External Flows," *Experiments in Fluids*, Vol. 13, 1992, pp. 361-368.

26. Squire and Savill, A.M., "Drag Measurements on Planar Riblet Surfaces at High Subsonic Speeds," Applied Scientific Research, Vol. 46, No. 3, 1989, pp.229-243.

27. Gillcrist, M.C. and Reidy, L.W., "Drag and Noise Measurements on an Underwater vehicle with a Riblet Coating,": In *Drag Reduction in Fluid Flows* (eds. R.H.J. Sellin & R.T. Moses, Ellis Horwood Publishers) pp. 99-106, 1989.

28. Sawyer, W.G. and Winter, K.G., "An Investigation of the Effect on Turbulent Skin Friction of Surfaces with Streamwise Grooves," *Proceedings of Turbulent Drag Reduction by Passive Means Conference*, Royal Aeronautical Society, London 15-17 september 1987.

29. Rohr, J., Anderson, G.W., and Reidy, L.W., "Experimental Investigation of the Drag Reducing Effects of Riblets in Pipes,": In *Drag Reduction in Fluid Flows* (eds. R.H.J. Sellin & R.T. Moses, Ellis Horwood Publishers) pp. 43-52, 1989.

30. Liu, K.N., Christodoulou, G., Riccius, O., and Fulachier, L., "Drag Reduction in Pipe Lined with Riblets," *AIAA Journal*, Vol. 28, No. 10, October 1990, pp. 1697-1698.

31. Nitschke, P., "Experimental Investigation of Turbulent Flow in Smooth and Longitudinal Grooved Tubes," NASA-TM-77480.

32. Nakao, S., "Application of V Shape Riblets to Pipe Flows," *Transactions of the ASME, Journal of Fluid Engineering*, Vol. 113, December 1991, pp. 587-590.

33. Feng, C., Yan-Ping, T., and Mao-Zhang, C., "An Experimental Investigation of Loss Reduction with Riblets on Cascade Blade Surfaces and Isolated Airfoils," ASME Paper No. 90-GT-207.

34. Robinson, S.K., "Effects of Riblets on Turbulence in a Supersonic Boundary Layer," AIAA Paper No. 88-2526.

35. Gaudet, L., "Properties of Riblets at Supersonic Speed," Applied Scientific Research, Vol. 46, No. 3, 1989, pp. 245-254.

36. Coustols, E. and de Zotti, A. : in Proceedings of the 5th European Drag Reduction Working Meeting, Teddington, November 1990.

37. Coustols, E. : in Proceedings of the 6th European Drag Reduction Working Meeting, Eindhoven, November 1991.

38. Stockman, N.O., Latapy, M.O., Andrew, T.L., and Rogers, D.H., "Scale Model Test of an Isolated Turbofan Nacelle with Riblets," SAE Paper No. 912128.

39. Walsh, M.J., Sellers, W.L, and McGinley, C.B., "Riblet Drag Reduction at Flight Conditions," AIAA Paper No. 88-2554.

40. McLean, J.D., George-Falvy, D.N., and Sullivan, P., "Fight-Test of Turbulent Skin-Friction by Riblets," *Proceedings of Turbulent Drag Reduction by Passive Means Conference* , Royal Aeronautical Society, London 15-17 september 1987.

41. Coustols, E., "Behavior of Internal Manipulators: "Riblet" Models in Subsonic and Transonic Flows," AIAA Paper No. 89-0963.

42 Caram, J.M. and Ahmed, A., "Development of the Wake of an Airfoil with Riblet," *AIAA Journal*, Vol. 30, December 1992, pp. 2817-2818. Also presented as AIAA paper No. 89-2199.

43. Choi, K., Pearcey, H.H., and Savill, A.M.," Test of Drag Reducing Riblets on a One-Third Scale Racing Yacht," *Proceedings of Turbulent Drag Reduction by Passive Means Conference*, Royal Aeronautical Society, London 15-17 , September 1987.

44. Djenidi, L., Liandrat, J., Anselmet, F., and Fulachier, L., "Numerical and Experimental Investigation of the Laminar Boundary Layer over Riblets," Applied Scientific Research, Vol. 46, No. 3, 1989, pp.263-270.

45. Newmann, D. and Dinkelacker, A., "Drag Reduction by Longitudinal Riblets on the Surface of a Streamwise Aligned Body of Revolution,": In *Drag Reduction in Fluid Flows* (eds. R.H.J. Sellin & R.T. Moses, Ellis Horwood Publishers) pp. 93-98, 1989.

46. Ladd, D.M., Rohr, J.J., Reidy, L.W., and Hendricks, E.W., "The Effects of Riblets on Laminar to Turbulent Transition," *Experiments in Fluids*, Vol. 14, 1993, pp. 1-9.

47. Bacher, E.V. and Smith C.R., "A combined Visualization-Anemometry Study of the Turbulent Drag Reduction Mechanisms of Triangular Micro-Groove Surface Modifications," AIAA Paper No. 85-0548.

48. Choi, S., "Near-Wall Structure of a Turbulent Boundary Layer with Riblets," *Journal of Fluid Mechanics*, Vol. 208, 1989, pp. 417-458.

49. Falco, R., "Correlation of Outer and Passive Wall Region Manipulation with Boundary Layer Coherent Structure Dynamics and Suggestions for Improved Devices," AIAA Paper No. 89-1026.

50. Gallagher, J.A. and Thomas, A.S.W., "Turbulent Boundary Layer Characteristics over Streamwise Grooves," AIAA Paper No. 84-2185.

51. Hooshmand, A., Youngs, R.A., Wallace, J.M., and Balint, J.L., "An Experimental Study of Changes in the Structure of a Turbulent Boundary Layer Due to Surface Geometry Changes," AIAA Paper No. 83-0320.

52. Vukoslavcevic, P., Wallace, J.M., and Balint, J.L., "On the Mechanism of Viscous Drag Reduction Using Streamwise Aligned Riblets: A Review with New Results," *Proceedings of Turbulent Drag Reduction by Passive Means Conference*, Royal Aeronautical Society, London 15-17 september 1987.

53. Park, S. and Wallace, J.M., "Flow Alteration and Drag Reduction by Riblets in a Turbulent Boundary Layer," AIAA Journal, Vol. 32, No. 1, January 1994, pp. 31-38.

54. Kahn, M.M.S., "A Numerical Investigation of the Drag Reduction by Riblet Surfaces," AIAA Paper No. 86-1127.

55. Bechert, D.W. and Bartenwerfer, M., "The Viscous Flow on Surfaces with Longitudinal Ribs," *Journal of Fluid Mechanics*, Vol. 206, 1989, pp. 105-129.

56. Launder, B.E. and Li, S., "On the Prediction of Riblet Performance with Engineering Turbulence Models," in Proceedings of the 6th European Drag Reduction Meeting, Eindhoven, November, 1991.

57. Choi, H.C., Moin, P., and Kim, J., "Direct Numerical Simulation of Turbulent Flow over Riblets," *Journal of Fluid Mechanics*, Vol. 255, 1993, pp. 503-539.

58. Chu, D.C. and Karniadakis, G.E., "A Direct Numerical Simulation of Laminar and Turbulent Flow over Riblet-Mounted Surfaces," *Journal of Fluid Mechanics*, Vol. 250, 1993, pp. 1-42.

59. Rotta, J.C., "Turbulent Boundary Layers in Incompressible Flows," Progress in Aeronautical Sciences, Ferri, A., Küchemann, D., and Sterne L.H.G., Editors, 1962, pp. 1-220.

60. Truong, T.V. and Pulvin, P.H., "Influence of Wall Riblets on Diffuser Flow," Applied Scientific Research, Vol. 46, No. 3, 1989, pp. 217-227.

61. Tweedt, D.L., Moore, R.D. and Chima, R.V., "Supersonic Througflow Fan Research-Baseline Fan Experimental and Computational Results," Supersonic Throughflow Technology Workshop, Lewis Research Center, October 14, 1993.

62 Gaudet, L., "Properties of Riblets at Supersonic Speed, "Applied Scientific Research, Vol. 46, No. 3, 1989, pp. 245-254.

63 Coustols, E., "Behavior of Internal Manipulators: "Riblet" Models in Subsonic and Transonic Flows," AIAA Paper No. 89-0963.

64. Thomas, J.L., and Walters, R.W., "Upwind Relaxation Algorithms for the Navier Stokes Equations," *AIAA Journal*, Vol. 25, No. 4, April 1987, pp. 527-534.

65. Taylor, A.C., III, "Convergence Acceleration of Upwind Relaxation Methods for the Navier-Stokes Equations," Doctoral Dissertation, Department of Mechanical Engineering, Virginia Polytechnic Institute and State University, Blacksburg, VA, July 1989.

66. Brock, J.S., "A Modified Baldwin-Lomax Turbulence Model for Turbomachinery Wakes," Master of Science Thesis, Department of Mechanical Engineering, Virginia Polytechnic Institute and Sate University, Blacksburg, VA, January 1991.

67. Roe, P. L., "Approximate Riemann Solvers, Parameter Vectors, and Difference Schemes," *Journal of Computational Physics*, Vol. 43, 1981, pp. 357-372.

68. Sorenson, R.L., "A Computer Program to Generate Two-Dimensional Grids About Airfoils and Other Shapes by the Use of Poisson's Equation," NASA-TM-81198.

69. Baldwin, B.S. and Lomax, H., "Thin Layer Approximation and Algebraic Model for Separated Turbulent Flows, " AIAA Paper No. 78-257.

70. Schetz, J.A. and Nerney, B., "The Turbulent Boundary Layer with Injection and Surface Roughness," *AIAA Journal*, Vol. 20, No. 9, September 1977, pp. 1268-1294.

71. Schetz, J.A., Foundations of Boundary Layer Theory for Momentum, Heat, and Mass Transfer, Prentice-Hall, Inc., Englewood Cliffs, New Jersey, 1984.

72. Moeckel, W.E., "Approximate Method for Predicting the Form and Location of Detached Shock Waves Ahead of Plane or Axially Symmetric bodies," NACA TN-1920, July 1949.

73. Clauser, F. H., "The Turbulent Boundary Layer," in *Advances in Applied Mechanics*, Vol. IV, Academic Press, New York, 1956.

Vita

The author was born in Redlands, California in December of 1964. His family moved to Springfield, Virginia in the summer of 1974. In June of 1983, he graduated from Lake Braddock Secondary School. Before entering college, he traveled with his parents to Virginia Tech. His first impression of Tech was the sight of Lane Stadium. While looking at this huge structure through a chain-linked fence, he read the timeless phrase "Home of the Fighting Gobblers". At that specific moment in time, the author felt a strong desire to leave the Tech campus and return home. Little did the author realize that he would spend the next ten years of his life at this institution.

In the fall of 1983, he entered Virginia Tech as an Accounting major. Immediately, he realized the error of his ways and transferred into the Department of Mechanical Engineering. The author completed his Bachelor of Science Degree in Mechanical Engineering in May of 1988, graduating *summa cum laude*. He continued his education at Virginia Tech completing his Masters in 1990 and his Ph.D in 1994. At this time, the author is adjusting to the concept of no longer being a resident Hokie.